Multi-mode optical resonators and wave chaos

PROEFSCHRIFT

ter verkrijging van
de graad van Doctor aan de Universiteit Leiden,
op gezag van de Rector Magnificus Dr. D. D. Breimer,
hoogleraar in de faculteit der Wiskunde en
Natuurwetenschappen en die der Geneeskunde,
volgens besluit van het College voor Promoties
te verdedigen op dinsdag 10 juni 2003
klokke 15.15 uur

door

Jos Dingjan

geboren te Amsterdam
op 8 september 1974

Promotiecommissie:

Promotor:	Prof. dr. J. P. Woerdman	
Copromotor:	Dr. M. P. van Exter	
Referent:	Prof. Dr. F. Haake	(Universität Duisburg-Essen)
Leden:	Prof. dr. ir. J. J. M. Braat	(Technische Universiteit Delft)
	Dr. T. Visser	(Vrije Universiteit Amsterdam)
	Dr. E. R. Eliel	
	Prof. dr. G. W. ’t Hooft	
	Prof. dr. G. Nienhuis	
	Prof. dr. P. H. Kes	

ISBN 90-9016973-3
© 2003 J. Dingjan

The work reported in this thesis was part of a research project supported by the “Stichting voor Fundamenteel Onderzoek der Materie” (FOM).

Aan mijn grootouders

Contents

1 Introduction 1

2 Geometric modes in a single-frequency Nd:YVO_4 laser 3

3 Optical resonators and the Gouy phase 13

3.1 Introduction . . . 14

3.2 Paraxial two-mirror resonators . . . 16

3.2.1 Wave-optical perspective . . . 16

3.2.2 Ray-optical perspective . . . 18

3.3 *Degenerate* paraxial two-mirror resonators . . . 20

3.4 Degenerate *nonparaxial* two-mirror resonators . . . 24

3.4.1 Presence of periodic orbits . . . 24

3.4.2 Stability of periodic orbits . . . 28

3.5 Folded three-mirror resonators . . . 30

3.6 Degenerate resonator as high-resolution interferometer . . . 33

3.7 Conclusions . . . 35

4 Attempts towards a cavity random laser 37

4.1 Introduction . . . 38

4.2 Experimental setup . . . 41

4.3 Spectral measurements . . . 44

4.3.1 Optical spectra . . . 44

4.3.2 Beat spectra . . . 46

4.4 Output power measurements . . . 50

4.4.1 Input-output curves . . . 50

4.4.2 Output power at fixed pump 52
4.5 Spatial measurements 55
4.6 Concluding discussion 57
4.7 Appendix: Calibrating the length of the resonator 58

5 Observation and manipulation of wave chaos in a folded optical resonator 61
5.1 Introduction 62
5.2 Folded optical resonator 64
5.2.1 Nonseparability 64
5.2.2 Setup 67
5.2.3 How we analyse the spectra 69
5.2.4 How we deal with losses 71
5.3 Results 72
5.3.1 Folding angle 2α 72
5.3.2 Opening angle ϕ 73
5.4 Concluding discussion 75

6 Diagnostics of wave chaos in a folded optical resonator 77
6.1 Introduction 78
6.2 Experiment 79
6.2.1 Setup 79
6.2.2 Method of analysis: general 80
6.2.3 Method of analysis: our case 81
6.3 Experimental validation 82
6.3.1 Transmission spectra 83
6.3.2 Averaging over realisations 84
6.3.3 Averaging over initial conditions 86
6.3.4 Line shape 86
6.3.5 Postselection of spectra 88
6.4 Concluding discussion 90

Bibliography 91

Samenvatting: Multimode optische trilholtes en golfchaos 95

Summary: Multi-mode optical resonators and wave chaos 105

Curriculum Vitae van de auteur 115

Curriculum Vitae of the author 116

Nawoord 117

Afterword 118

Chapter 1

Introduction

Every day in modern life we encounter, knowingly or unknowingly, an incredible number of lasers, used in a variety of devices and applications. Between getting out of bed in the morning and switching on the first laser in the laboratory, we use, look at or pass within sneezing distance of tens of lasers, incorporated into CD players and CD-ROM drives, in the levels and laser ranging equipment used by the builders at construction sites, in the laser speed guns used by the police at speed traps, and in the checkouts at the supermarket. Every single one of those lasers consists of the same basic elements: a gain medium for amplification of light, and a cavity to confine light and provide the feedback necessary for laser action.

This last component, the laser cavity, can be as simple as two flat reflective end facets of a semiconductor laser, or the intricate construction of mirrors found in high performance, pulsed lasers. It is the cavity that, through constructive and destructive interference, causes a laser to emit light in a narrow wavelength band and a confined beam. But it is not only in lasers that cavities play a large role, they are also indispensable in interferometry. They are used to analyse optical spectra, to set frequency standards, and to detect changes in length or optical properties.

This thesis deals with optical cavities, both as part of a laser system and as stand-alone systems. Its focus is on multi-mode cavities, where more, potentially many more, than one cavity mode is important. Optical cavities can be classified in many ways, but the most prevalent is that in *stable* and *unstable* resonators. This stability refers to the transverse behaviour of light in such a cavity. In a stable resonator, light remains transversely confined near the optical axis of the system, while in an unstable resonator there is no such confinement. Whether a cavity is stable or unstable is determined by the focusing properties of the elements that form the cavity. In this thesis, we deal (almost) exclusively with stable resonators.

The work reported in these chapters was performed as a Ph.D. project at the Quantum Optics Group at Leiden University. The initial goal of this project was to construct a *cavity random laser*, a random laser based not on a random scattering element, but on a standard laser cavity. While a cavity random laser has so far proven to be elusive, the genesis of all chapters in this thesis still lies in this concept. Two of the four experimental chapters, chapters 2 and 4, deal with laser systems, and were born directly out of the search for a cavity random laser. As such, the cavities considered in those chapters are not far out of the ordinary. It is the multi-mode nature, combined with the particular choice of cavity length in relation to the radii of curvature of the mirrors, that leads to surprising effects that had not previously been reported. These chapters extend the general understanding of multi-mode cavities and the implications of the established theoretical framework for resonator theory.

The other two experimental chapters, chapters 5 and 6, deal with a passive system: a nonstandard cavity, constructed from standard optical elements, that is *wave chaotic*. This wave-chaotic nature expresses itself in the eigenmodes of the cavity, and only becomes apparent when many modes are considered in the analysis. That such a relatively simple system could show wave chaos had hitherto not been suspected, and we expect that this system will, because of its simplicity, play an important role in studying many aspects of optical wave chaos.

In this thesis, several chapters have been written as, or are based on, separate articles intended for publication, while others were written specifically for this thesis. Nevertheless, in putting together this thesis I have tried to avoid unnecessary duplication and repetition, while still allowing chapters to be read individually. Specifically, chapters 2, 3 and 4 can be read separately, with only a few back references to important figures or equations. While it is possible to read chapters 5 and 6 on their own, they both rely heavily on each other.

In *Chapter 2* we report an experiment on an off-axis pumped Nd:YVO_4-laser that, instead of emitting in a conventional higher order transverse mode, at particular cavity lengths operates in a mode that strongly resembles a closed periodic orbit. Such modes, dubbed *geometric modes*, occur in a finite range around frequency-degenerate cavity configurations, and are the result of phase and frequency locking of a large number of transverse modes.

In *Chapter 3* we recall the expressions governing the spectral properties of optical cavities, and emphasise and extend the framework to describe both the ray-optical and wave-optical behaviour of cavities around the special configurations of chapter 2. Furthermore, we speculate, on ray-optical grounds, about the effects that violating the paraxial approximation has on this behaviour, and discuss a possible application of frequency degenerate optical cavities in interferometry.

In *Chapter 4* we report on a number of other experiments performed on essentially the same laser system as used in chapter 2 in our (unsuccessful) search for a cavity random laser. We present results that demonstrate some of the reasons for this lack of success, and a few surprising results around the edge of the stability region of our cavity.

In *Chapter 5* we experimentally show the presence of wave chaos in a novel and relatively simple optical cavity based on standard optical elements. In this cavity, a *folded* optical resonator, wave chaos is possible because of the relatively large degree of nonparaxiality that is induced by the curved folding mirror. By changing the angle of incidence of light on this folding mirror, or the opening angle of the intracavity modes, the amount of nonparaxiality, and thereby the strength of the wave chaos, can be controlled.

In *Chapter 6* we will validate the method of analysis used in chapter 5 to demonstrate the presence of chaos.

After chapter 6 follow a bibliography, popular summaries in Dutch and English, and the author's curriculum vitae.

Chapter 2

Geometric modes in a single-frequency Nd:YVO$_4$ laser[1]

We report single-frequency operation of a Nd^{3+}:YVO$_4$*-laser in geometric modes when its cavity is strongly frequency degenerate. These geometric modes closely resemble closed ray paths and are the result of gain-guiding induced phase and frequency locking of Hermite-Gaussian modes. The finite locking range observed around frequency degenerate cavity configurations is in good agreement with theory.*

---

[1] J. Dingjan, M.P. van Exter, and J.P. Woerdman, "Geometric modes in a single-frequency Nd:YVO$_4$ laser", Opt. Commun. **188**, 345–351 (2001).

In 1964, Herriott, Kogelnik and Kompfner [1] showed that off-axis rays in a spherical mirror optical resonator will have vertices on the mirrors that lie, in general, on ellipses. For specific resonator configurations the pattern of vertices closes on itself, leading to closed loop ray trajectories inside the resonator. Combining the ray analysis and frequency analysis of such passive resonators, Ramsay and Degnan [2] have shown that configurations corresponding to closed ray trajectories show a high degree of frequency degeneracy. The reverse statement, that configurations with a high degree of frequency degeneracy allow closed geometric trajectories, is equally true. More recently, these degeneracies have been studied from the perspective of periodic orbits and maps [3, 4, 5], and the influence of frequency degeneracies on laser threshold and output power has been discussed [6]. The novelty of our work is that it combines the closed trajectories of the ray optical picture with the frequency degeneracies of the wave optical picture, resulting in geometric laser modes.

The frequencies of Hermite-Gaussian modes native to a spherical mirror resonator are given by (see for example Siegman [7])

$$\nu_{q,mn} = \frac{c}{2L}\left\{q + (m+n+1)\frac{\theta}{2\pi}\right\}, \tag{2.1}$$

with θ the Gouy phase angle, q the longitudinal mode index, m and n the transverse mode indices, and L the length of the resonator. The Gouy phase angle is related to the resonator configuration according to

$$\cos^2\left(\frac{1}{2}\theta\right) = g_1 g_2, \tag{2.2}$$

where $g_{1,2} = 1 - L/R_{1,2}$, with $R_{1,2}$ the radii of curvature for the two mirrors. Cavity configurations such that the Gouy phase angle is a rational fraction of 2π, i.e., $\theta = 2\pi K/N$, will lead to a ratio of transverse frequency spacing to longitudinal frequency spacing $\Delta\nu_{\mathrm{T}}/\Delta\nu_{\mathrm{L}} = K/N$. This in turn leads to a high degree of frequency degeneracy, as lowering the longitudinal mode index q by K, while simultaneously raising the sum of the transverse mode indices $m+n$ by N, will leave the frequency unaltered. At the same time, in a ray-optical picture this cavity allows closed geometric paths in the cavity, as for example the trajectory in Fig. 2.3d on page 6. These trajectories close after N round trips, and will make K transverse excursions in the cavity before closure occurs, thereby illustrating the intimate connections between the wave-optical and the ray-optical picture.

In our experiments we have studied the effects of these frequency degeneracies in an active laser resonator. The cavity configuration is drawn schematically in Fig. 2.1. We use an optically pumped Nd^{3+}:YVO_4-crystal as gain medium. One of the planar facets of the 1 mm thick chip is coated for high reflectivity (reflectivity higher than 99.8%), forming one of the two mirrors of the resonator. The other facet of the chip has an antireflective coating for the laser wavelength. The output coupler is formed by a spherical, concave mirror with a reflectivity of 95% and a radius of curvature of 25 mm. The length of the cavity is varied between 8 and 21 mm, to select either highly frequency-degenerate or non-frequency-degenerate configurations. A key point is that the pump spot on the crystal is displaced from the axis of the system by a distance Δ, which is of the order of 1 mm or less. This off-axis pumping scheme can induce strong gain guiding effects which are easily manipulated, as the strength of the gain guide does not primarily depend on the size of the pump spot relative

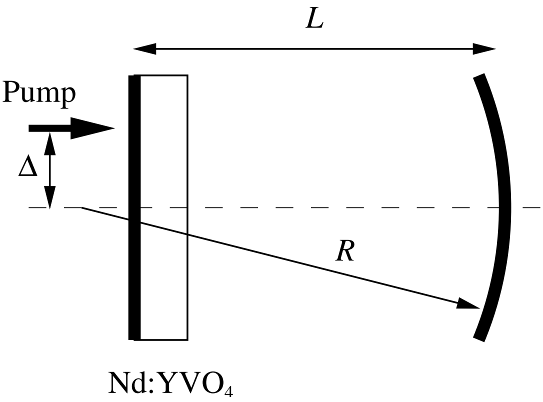

Figure 2.1: *Schematic resonator configuration, where L is the length of the resonator, R is the radius of curvature of the concave mirror and* Δ *is the displacement from the axis of the pump spot.*

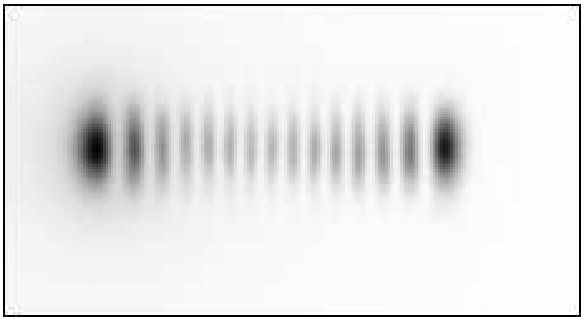

Figure 2.2: *Transverse beam profile for* $K/N \approx 0.256 > 1/4$.

to the size of the fundamental Gaussian mode waist, but rather depends on the position of the pump spot relative to the position of the outermost lobes of high-order Hermite-Gaussian modes. This allows for a broader range of guiding strengths as compared to on-axis pumping. The pump spot had a typical waist size of 0.11 mm, and the typical threshold pump power was of the order of 50 to 75 mW.

Without selecting a frequency-degenerate cavity configuration a laser with off-axis pumping will operate in a higher-order Hermite-Gaussian mode, a fact that was observed earlier by Chen *et al.* [8]. For such cavity configurations our experiment shows the same result, as can be seen in Fig. 2.2. For resonator configurations for which the Gouy phase $\theta = 2\pi K/N$, however, we find a drastically different behaviour of our laser. As an example, we change the resonator from an “arbitrary” configuration to a hemiconfocal geometry, for which the cavity length $L = R/2$, so that $\theta = 2\pi \cdot 1/4$, or $K/N = 1/4$. With this resonator geometry the behaviour of the laser changes drastically. Figures 2.3a–c are transverse intensity profiles taken at different axial positions. The laser is clearly operating in a mode that is completely unlike a

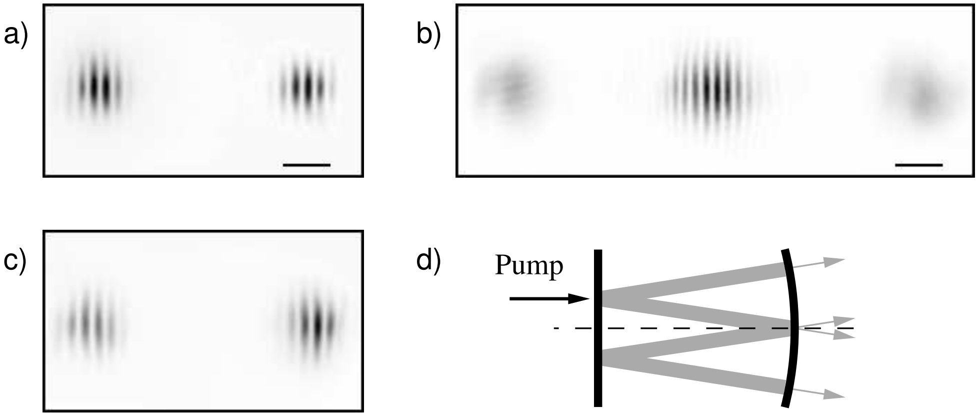

Figure 2.3: *Transverse beam profiles for* $K/N = 1/4$*: a) near field on the chip, b) near field on the concave output coupling mirror, c) far field, d) schematic depiction of the mode pattern inside the resonator. The black scale bars in a) and b) have a length of* 100 μm.

Hermite-Gaussian mode. Instead, the laser operates in a pattern that is schematically drawn in Fig. 2.3d: a W-shaped path that closely resembles a closed ray trajectory corresponding to the resonator geometry. One of the two vertices on the flat mirror coincides with the location of the pump spot, while the other vertex is its mirror image with respect to the optical axis of the system. For such a W-mode, two pairs of parallel beams emerge from the laser, as could be observed directly.

A striking feature in the transverse beam profiles are the deeply modulated fringes that occur both in the near fields and in the far field. In the near field on the flat mirror (Fig. 2.3a) we see that both spots show modulation, while in the near field on the curved mirror (Fig. 2.3b) only the central of the three spots has fringes. Comparing the intensity profiles with Fig. 2.3d, we see that these fringes occur at vertices where the ray path hits the mirror at non-normal incidence. We can think of these fringes as being the result of interference between two beams intersecting at an angle.The fringes in the far field are the result of interference between the two parallel but slightly offset beams that make up each spot.

The observed W-shaped path is in fact not the only closed ray path that fits inside a resonator for which $K/N = 1/4$. In the paraxial approximation, where we can find the propagation of rays inside the cavity using the ABCD-matrix formalism [7], we find that *any* ray inside the cavity will reproduce, and hence form a closed trajectory, after N round trips. This is the direct result from the fact that the ABCD-matrix for such a resonator satisfies

$$\begin{pmatrix} A & B \\ C & D \end{pmatrix}^N = \mathbb{1}\,, \tag{2.3}$$

where $\mathbb{1}$ is the identity matrix. Figure 2.4 shows typical examples of the closed ray paths that are possible in a cavity for which $K/N = 1/4$. Figure 2.4b is a generic trajectory, whereas the trajectories in Figs. 2.4a and c are limiting cases: a W-shaped trajectory and an M-shaped

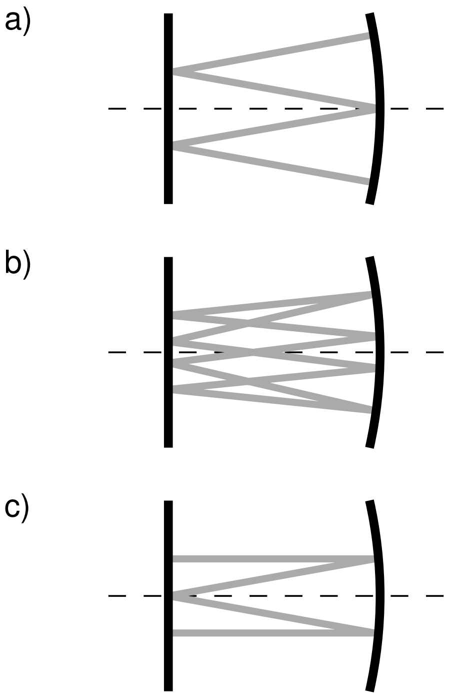

Figure 2.4: *Typical closed ray trajectories for* $K/N = 1/4$*: a) W-shaped path, b) generic path, c) M-shaped path.*

trajectory. In these limiting cases the trajectory hits one of the mirrors at normal incidence, so that the ray path reverses direction and starts retracing itself. A direct result of this is that the number of vertices on both mirrors is reduced. This reduction in the number of vertices explains the fact that we only observe the W-shaped path of Fig. 2.4a in our experiments, and none of the other possible trajectories. The W-shaped path has, of all possible ray paths, the lowest number of vertices on the flat mirror, i.e., two. One of these two vertices coincides with the location of the pump spot, while the other vertex lies on the planar mirror at a position that is not pumped. Trajectories different from the W-path will have more vertices on the flat mirror, and hence more vertices that do *not* coincide with the pumped region. Therefore, the overlap between modes that correspond to these trajectories and the pump region will be lower, leading to a higher threshold.

Because of the off-axis pumping of our system, axial symmetry is broken. The natural basis for this type of resonator with broken axial symmetry is the set of Hermite-Gaussian modes. The peculiar geometric beam patterns we observe are then formed by a phase-locked linear combination of the Hermite-Gaussian modes. Analysis of the optical spectrum with a Fabry-Pérot interferometer (see Fig. 2.5) shows that, for pump powers up to $P = 1.1\,P_{\mathrm{th}}$, where P_{th} is the threshold pump power, the laser emits at a single frequency, while still operating in a geometric mode. This implies that the transverse modes that combine to form the geometric mode all have the same frequency. As directly follows from the discussion above, Hermite-

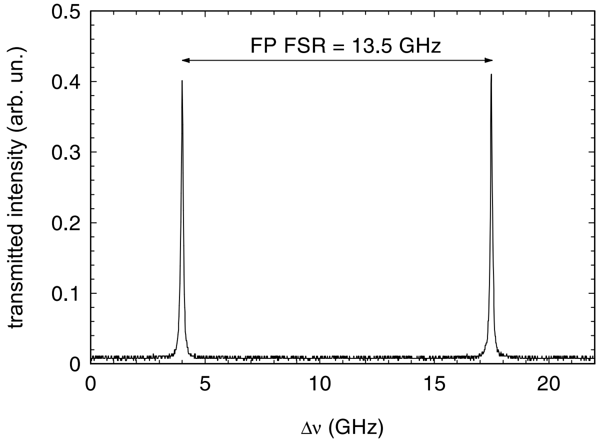

Figure 2.5: *Fabry-Pérot spectrum taken inside the locking range for which* $K/N = 1/4$*.*

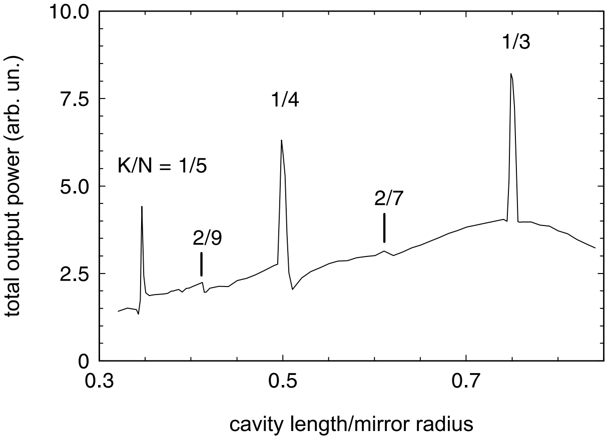

Figure 2.6: *Total laser output power versus normalised cavity length* L/R*, at fixed pump power.*

Gaussian modes of different total transverse order $m+n$, but with the same frequency, must necessarily be of different longitudinal order.

From Eq. (2.2) we see that the Gouy phase angle θ depends on the ratio L/R, rather than on the cavity length L. In Fig. 2.6 we have plotted the total power output of the laser at constant pump power against the scaled resonator length L/R. Several low-order frequency ratios K/N clearly show up as drastic increases in the output power of the laser. Furthermore, this power increase persists in a finite interval around these frequency-degenerate points. These intervals have a typical half width of the order of $\Delta L = 0.1$ mm.

If we lower the pump power to ensure single-mode lasing, we find that the shape of the mode is essentially unchanged over the entire length of each such interval, as illustrated by

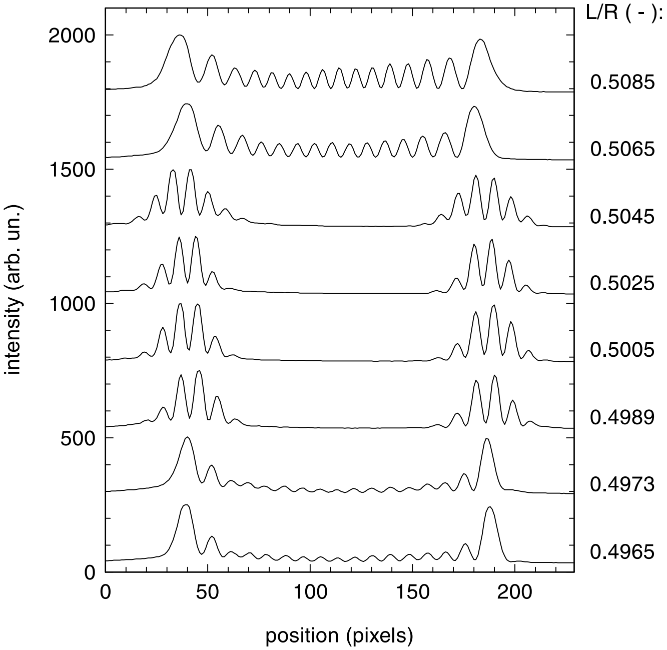

Figure 2.7: *Cross-sections through transverse beam profiles, taken in the near field on the flat mirror, for various resonator lengths around the point for which* $K/N = 1/4$.

the central four traces in Fig. 2.7. This shows that the transverse Hermite-Gaussian modes participating in the phase locking are frequency degenerate throughout these intervals. Since, for a cold cavity, this frequency degeneracy only occurs at specific cavity lengths, instead of over intervals centred at such lengths, we conclude that the modes lock their frequencies over the extent of such intervals.

Physically speaking, this frequency locking is the result of the competition between two mechanisms. These are the Maximum Emission Principle [9], which expresses that the laser strives to maximise its output power by pulling the resonance frequencies of the empty cavity together, and the modal dispersion, which is related to the Gouy phase angle of the resonator configuration and which can push the resonance frequencies apart. The physical process facilitating the Maximum Emission Principle is the strong gain guiding, caused by the off-axis pumping of the laser; pulling the frequencies of Hermite-Gaussian modes together to the same value allows phase locking of these modes to produce a time-constant mode profile that has a better overlap with the location of the pump spot than the Hermite-Gaussian modes individually would have.

A formal description runs as follows. We write the intracavity light field $|s\rangle$ on a Hermite-Gaussian basis $|u_i\rangle$ as $|s\rangle = \sum_i a_i |u_i\rangle$. The evolution of this light field through one round trip is given by the effective round trip evolution operator M:

$$|s\rangle_{\text{after}} = M|s\rangle_{\text{before}} . \tag{2.4}$$

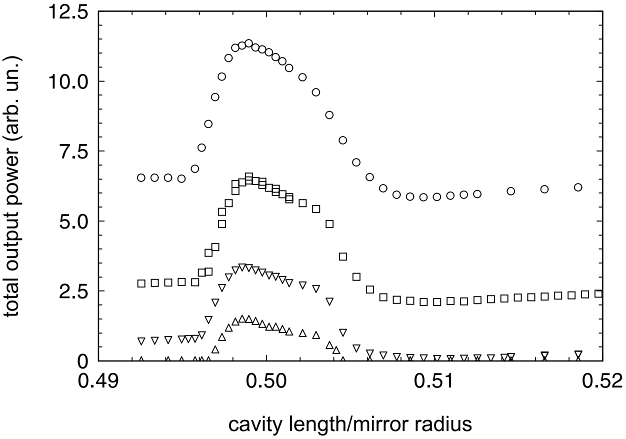

Figure 2.8: *Total laser output power around* $K/N = 1/4$, *for four different pump powers, in arbitrary units,* $P_{\text{pump}} = 0.60,\ 0.80,\ 1.10,\ 1.50$, *respectively.*

In the absence of gain guiding, the set of Hermite-Gaussian modes will be the set of eigenmodes of this evolution operator, and hence this operator will be diagonal, with the complex elements M_{ii} containing the modal gain, the Gouy phase and the transverse order of the mode. The combination of the Gouy phase and the transverse mode order will determine the optical frequency of the mode. In general this will lead to different frequencies for the various modes, except for very specific Gouy phases.

The introduction of gain guiding introduces off-axis elements M_{ij} in our effective round trip evolution operator, coupling modes i and j. Therefore, our initial set of Hermite-Gaussian modes will no longer be the set of eigenmodes for this operator. Instead, we find a new set of eigenmodes $|v_i\rangle$, a basis in which the evolution operator diagonalises. The elements of our diagonalised evolution operator $\tilde{M}_{ii}$ will be the eigenvalues for the modes $|v_i\rangle$, determining both modal gain and modal eigenfrequencies. These modal gains and eigenfrequencies will differ from those for the Hermite-Gaussian modes that were the eigenmodes in the absence of gain guiding. This allows values for the Gouy phase that again lead to degeneracies in the eigenfrequencies, whereas previously, for the cold cavity, there were none. The driving force for this is the maximalisation of the round trip amplification factor

$$\gamma = \frac{|\langle s|M|s\rangle|}{\langle s|s\rangle} = \frac{\left|\sum_{i,j} a_i^* a_j \langle u_i|M|u_j\rangle\right|}{\sum_i |a_i|^2} . \tag{2.5}$$

A more detailed look at the total laser output power around the point for which $K/N = 1/4$ is shown in Fig. 2.8. These data allow us to deduce the laser threshold for lasing in a single Hermite-Gaussian mode, just outside the locking interval, $P_{\text{th,HG}}$. We find $P_{\text{th,HG}} \approx 1.5 P_{\text{th,geo}}$, where $P_{\text{th,geo}}$ is the laser threshold for geometric lasing at the centre of the locking interval. Furthermore, we see that there is no significant dependence of the width of the locking interval on the pump power P, when the pump parameter $P/P_{\text{th,geo}}$ is varied from 1.2 to 3, or, equivalently, when the pump parameter $P/P_{\text{th,HG}}$ is varied from 0.8 to 2. The transition from Hermite-Gaussian to geometric mode lasing is abrupt on both sides of the locking interval, even though the total output power shows a smooth transition for higher cavity lengths. The half width of the locking interval is $\Delta L \approx 0.12$ mm. Note that the power output in the locking interval is asymmetric with respect to the centre of the locking range. Note also that we observe a weak minimum in the output power just outside the locking range, for cavities longer than hemiconfocal. These intriguing observations remain as yet unexplained.

If we increase the pump power too far above threshold, the laser operates in more than one mode, i.e., more than one frequency. It is important to realise that, for cavity configurations for which we have frequency locking, the frequency degeneracy allows geometric beam patterns not only at a single frequency, but rather at a whole range of frequencies, spaced at a distance of $\Delta\nu_{\mathrm{T}}$. Experimentally, as we increase the pump power we observe continued operation in closed ray paths, with a gradual disappearance of the fringes in the spots, as the position of the fringes for the individual geometric modes varies.

The pump parameter P/P_{th} at which multi-mode lasing sets in is found to be $P/P_{\mathrm{th}} \approx 1.1$; it is the same for emission in Hermite-Gaussian modes or geometric modes, as observed for cavity lengths just outside and inside the frequency locking interval, respectively. This is not surprising, as for the two cases, both the frequency difference with the next mode that starts lasing and the spatial hole burning effects are comparable. Naively, one might expect that for lasing in Hermite-Gaussian modes, the next mode to start lasing would be the nearly frequency degenerate one. However, this is not the case, because the difference in total transverse mode index between the lasing mode and this mode is generally quite large; as a result, the overlap with the pump spot is much worse.

We will now quantitatively estimate the strength of the frequency locking. From Eq. (2.1) we find that the frequency difference between Hermite-Gaussian modes for which the longitudinal mode index difference $\Delta l = q_2 - q_1 = -K$ and the transverse mode index difference $\Delta t = (n_2 + m_2) - (n_1 + m_1) = N$ equals

$$\Delta\nu_{K/N} = \nu_{q-K;(m+n)+N} - \nu_{q,mn} = \frac{c}{2L}\left\{-K + N\frac{\arccos\sqrt{g_1 g_2}}{\pi}\right\}. \tag{2.6}$$

Substituting g_1 and g_2 for a plano-concave cavity and taking the derivative $\mathrm{d}\Delta\nu_{K/N}/\mathrm{d}L$ we find that in our experiment, around the resonator configuration for which $K/N = 1/4$, that is, for $L = 1/2\,R = 12.5$ mm, the previously degenerate modes, upon changing the length of the resonator, move apart at a rate of

$$\frac{\mathrm{d}\Delta\nu_{1/4}}{\mathrm{d}L} \approx 6.1 \times 10^2\ \mathrm{GHz/m}. \tag{2.7}$$

Equation (2.7) implies that, in the absence of a mechanism that tries to maintain the frequency degeneracy, at the edge of the locking interval, which we found to have a half width of $\Delta L = 0.12$ mm, two nearest-neighbour, previously degenerate, modes would be $\Delta\nu = 73$ MHz apart. This is a measure for the strength of the dispersive effect of the Gouy phase angle, striving to lift the frequency degeneracy, which we shall denote with ν_{disp}.

At the edge of the locking interval this driving force will be balanced by the difference in gain between laser operation in a Hermite-Gaussian mode and in a geometric mode. This gain difference can be found from the difference in laser thresholds for the two types of operation. If, for a cavity configuration just outside the locking range, we are at the threshold of laser operation, we would, in the absence of the dispersive effect of the Gouy phase angle, be a factor of 1.5 above threshold for emission in a geometric mode (see Fig. 2.8). This means that the gain rate for such a geometric mode is a factor of 1.5 higher than the gain rate for a Hermite-Gaussian mode, which must be equal to the cavity loss rate. Neglecting losses other than mirror outcoupling losses we estimate a minimum value for the cavity decay rate of

$$\Gamma_{\mathrm{c}} = -\frac{c}{2L} \ln \mathscr{R}_1 \mathscr{R}_2 = 0.64\ \mathrm{ns}^{-1}, \tag{2.8}$$

where we have used that the reflectivities $\mathscr{R}_1 = 99.8\%$ and $\mathscr{R}_2 = 95\%$, and that $L = 12.5$ mm. From this we find that the excess gain rate for laser operation in a geometric mode relative to operation in a Hermite-Gaussian mode equals $\gamma_{\mathrm{ex}} = 0.5\Gamma_{\mathrm{c}} = 0.32\ \mathrm{ns}^{-1}$. This excess gain rate is a measure for the strength of the driving force trying to preserve the frequency degeneracy. It does indeed roughly equal the strength of the dispersive effect, which we calculated as $\nu_{\mathrm{disp}} = 73$ MHz, i.e., $\omega_{\mathrm{disp}} = 2\pi\nu_{\mathrm{disp}} = 0.46\ \mathrm{ns}^{-1}$.

Ramsay and Degnan [2] suggest that the width of the locking region is determined by the degree of nonparaxiality in the problem. However, their derivation is specific to cavity configurations that are at the edge of the traditional resonator stability diagram ($g_1 g_2 = 1$). Therefore, their expressions do not hold here.

We stress the fundamental difference between locking of modes of the type we observed and the so-called temporal or spatial mode locking in lasers. The latter two cases, dealing with phase locking of modes with different frequencies, can lead to, for example, pulsed laser operation [7], or a periodically scanning output beam [10]. However, in our experiments we observe both frequency and phase locking of the modes, i.e., we deal with a *single* frequency, leading to CW output in geometric mode profiles.

In conclusion, we have demonstrated that at certain, frequency-degenerate, cavity configurations, an off-axis pumped laser will phase and frequency lock transverse modes to maximise the overlap between the pump spot and the lasing mode. This maximises the output power, and leads to beam profiles that closely resemble closed ray paths that fit said cavity configuration. Furthermore, this phase and frequency locking persists over a finite interval around such degenerate points. Also, these experiments serve to illustrate the striking duality between wave and ray optics, combining frequency degeneracy with closed ray trajectories.

Chapter 3

Optical resonators and the Gouy phase

In this chapter we investigate some basic properties of optical resonators from a wave-optical and from a ray-optical point of view. Since it plays a pivotal role in determining both the spectral properties of optical resonators and the behaviour of rays inside such resonators, we shall use the Gouy phase as a unifying concept. We will recall the basic expressions for paraxial two-mirror resonators, and consider the special case where the Gouy phase θ *assumes a rational value,* $\theta = 2\pi K/N$*. In this case a paraxial two-mirror resonator has, at the same time, a highly degenerate eigenfrequency spectrum and supports closed periodic orbits that repeat after* N *round trips. Outside the paraxial limit, these periodic orbits are still useful: they allow us to make general statements about the behaviour of the Gouy phase for nonparaxial eigenmodes.*

We shall also extend the expressions for the paraxial two-mirror resonator so that they can be used to analyse paraxial resonators with astigmatic eigenmodes. In particular, we shall look at a folded three-mirror resonator, both from the viewpoint of the eigenfrequency spectrum and the possibility of periodic orbits, and we shall briefly speculate about nonparaxial three-mirror resonators.

Finally, we suggest a possible application of a degenerate two-mirror resonator as a high-resolution length-sensing interferometer. We discuss its principle of operation and point out some limitations.

3.1 Introduction

At the start of the last decade of the 19th century, Gouy [11, 12] showed that a beam of light that passes through a focus acquires an additional phase factor π. He demonstrated this using a variation on the Fresnel double-mirror experiment, where one of the two mirrors was replaced by a concave mirror, see Fig. 3.1. In this setup, the light transmitted through a small pinhole is reflected by both mirrors. Because the mirrors are placed at a slight angle to each other, the two reflected beams will overlap and interfere, leading to a bull's eye pattern of concentric rings. Gouy observed that the centre of this bull's eye pattern changed from bright to dark when going through the focus of the beam stemming from the concave mirror. He attributed this to a jump in the phase difference between the two beams of π, caused by the focused beam acquiring additional phase upon traversing the focus.

Further study showed that the magnitude of this so-called *Gouy phase* depends on the transverse structure of the focused beam. For well-behaved, smooth beams without additional structure, this additional phase equals π; for beams with more transverse structure it is larger. In the case of astigmatic beams, each of the two principal foci accounts for half of the Gouy phase. For example, a beam that is focused in one plane only, e.g., with a cylinder lens, will only acquire an extra phase of $\pi/2$. This phase anomaly, or Gouy effect, is not limited to electromagnetic waves in the optical regime, but it also applies to, for example, microwaves and acoustical waves.

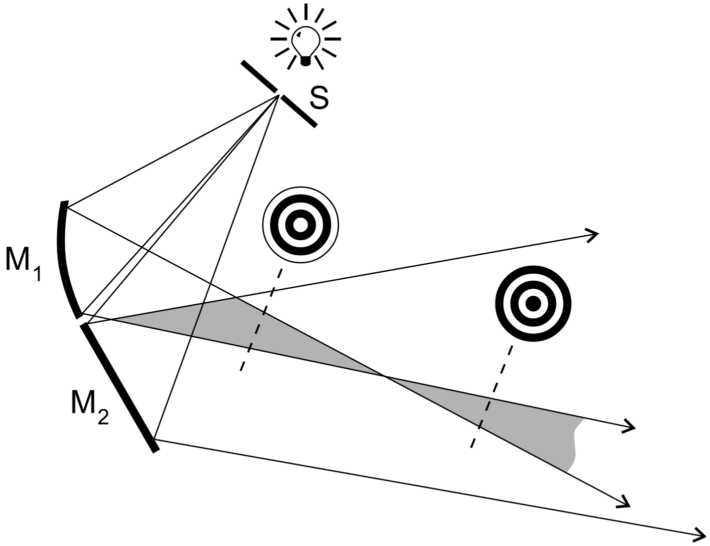

Figure 3.1: *Schematic setup for the Gouy experiment. Light from a lamp source is transmitted through a pinhole S, and subsequently reflected by mirrors* M_1 *and* M_2. *Because the two mirrors are placed at a slight angle, the reflected beams will overlap in the shaded area. If, in that overlap region, one places a card in the two beams, one will see a bull's eye pattern, where the brightness of the centre depends on whether the card is in front of or behind the focus of the second beam.*

Careful analysis has shown that this change in phase does not occur suddenly, but instead occurs gradually in a region around the focus. If one propagates an optical beam from one reference plane to the other, both being in the focal region, it will acquire a smaller additional phase than when the reference planes are situated in the front and back far field. This smaller phase, which can now be any fraction of the full Gouy phase, can be interpreted as the phase difference between a focused beam and a plane wave that is accumulated when proceeding from the one to the other reference plane. Customarily, this fraction is also called *the* Gouy phase, where the distinction with the full Gouy phase (referring to propagation from far field to far field) follows from context.

This (partial or full) Gouy phase has immediate relevance for the spectral properties of optical *resonators*, since it must be added to the propagation phase in the definition of round trip resonance. Its role in determining spectral properties is perhaps best known in the context of two-mirror resonators in the paraxial approximation (being the approximation that all angles are small, so that $\sin\alpha = \alpha$).

Since at first glance the Gouy phase appears to be a purely *wave*-optical property, it is surprising to find that it also plays a prominent role in determining the *ray* properties of resonators. This is a direct consequence of the fact that Gaussian beam propagation rules are the same as the rules that govern paraxial ray optics.

In this chapter we draw together equations and concepts concerning wave optics and ray optics in resonators of various types, using the Gouy phase as a unifying concept. Most of these results are not new, but are phrased in ways that are useful for the rest of this thesis. The combination of topics emphasises aspects of optics that rarely get much attention in textbooks or scientific journals. Our discussion naturally leads to speculation on cases that are not covered by standard theory, most notably nonparaxial resonators.

In the next section we shall recall the familiar expressions for paraxial two-mirror resonators that can be found in any textbook on laser physics and resonator optics [7, 13, 14], and highlight the parallels between wave and ray optics in such systems. Then, in section 3.3 we shall consider so called *degenerate* paraxial two-mirror resonators, where the Gouy phase is a rational fraction of 2π, $\theta = 2\pi K/N$. As we already saw in chapter 2, such systems can show behaviour that is very different from more generic resonator configurations, due to the occurrence of closed periodic orbits inside the resonator. Next, in section 3.4, we will consider what happens to those periodic orbits, and hence to that special behaviour, outside the paraxial limit, and we will speculate about the Gouy phase for nonparaxial modes.

In section 3.5 we shall consider the Gouy phase in the context of three-mirror resonators, where the resonator eigenmodes are astigmatic. We shall also give some attention to the possibility of closed periodic orbits in this type of resonator, and briefly speculate about three-mirror resonators outside the paraxial limit.

Finally, in section 3.6 we shall discuss the possibilities of using a degenerate resonator to create a high-resolution optical interferometer.

3.2 Paraxial two-mirror resonators

3.2.1 Wave-optical perspective

The simplest possible optical resonator is a stable paraxial two-mirror resonator. Its eigenmodes are the familiar Hermite-Gaussian or Laguerre-Gaussian modes. For a fundamental Gaussian *beam*, calculating the Gouy phase is straightforward. If we choose $z = 0$ at the location of the focus of the beam, and calculate the phase difference relative to this focus we find that

$$\phi(z) = \arctan\left(\frac{z}{z_\mathrm{R}}\right) , \tag{3.1}$$

where z_R is the Rayleigh range of the beam (see chapter 17 of ref. [7]). The Gouy phase upon going from a plane at z_0 to a plane at z_1 is then given by

$$\phi_{0,1} = \phi(z_1) - \phi(z_0) = \arctan\left(\frac{z_1}{z_\mathrm{R}}\right) - \arctan\left(\frac{z_0}{z_\mathrm{R}}\right) . \tag{3.2}$$

The *round trip* Gouy phase θ for the fundamental Gaussian mode of a resonator can be found by choosing an arbitrary reference plane z_r inside the resonator, and calculating the total Gouy phase going from this reference plane to the plane of one of the two end mirrors, located at z_2, then to the other end mirror at z_1 (taking into account the fact that we are now travelling in the opposite direction), and back again to z_r,

$$\theta = \left[\phi(z_2) - \phi(z_\mathrm{r})\right] + \left[-\phi(z_1) + \phi(z_2)\right] + \left[\phi(z_\mathrm{r}) - \phi(z_1)\right] = 2\left[\phi(z_2) - \phi(z_1)\right] , \tag{3.3}$$

where we have assumed that $z_1 < z_\mathrm{r} < z_2$. We see that this result is independent of the choice of reference plane.

One useful way to parametrise the geometry of a two-mirror resonator is through the so called “g parameters” $g_{1,2} \equiv 1 - L/R_{1,2}$, where L is the length of the resonator and R_1 and R_2 are the radii of curvature of the two mirrors. We then find, from elementary geometrical-optical considerations (see, for example, chapter 15 of ref. [7]), that the case $0 \leq g_1 g_2 \leq 1$ corresponds to a so called *stable* resonator. In a wave-optical context, a resonator is called stable when its eigenmodes have finite transverse dimensions on the mirrors. The $1/\mathrm{e}^2$ intensity radii of the spots on the mirrors w_1 and w_2, as well as the $1/\mathrm{e}^2$-radius of the focus of the beam w_0 (the “waist”), can be calculated using (see chapter 14 of ref. [13])

$$w_1^2 = \frac{\lambda L}{\pi}\sqrt{\frac{g_2}{g_1(1-g_1 g_2)}} , \tag{3.4}$$

$$w_2^2 = \frac{\lambda L}{\pi}\sqrt{\frac{g_1}{g_2(1-g_1 g_2)}} , \tag{3.5}$$

and

$$w_0^2 = \frac{\lambda L}{\pi}\sqrt{\frac{g_1 g_2(1-g_1 g_2)}{(g_1+g_2-2g_1 g_2)^2}} . \tag{3.6}$$

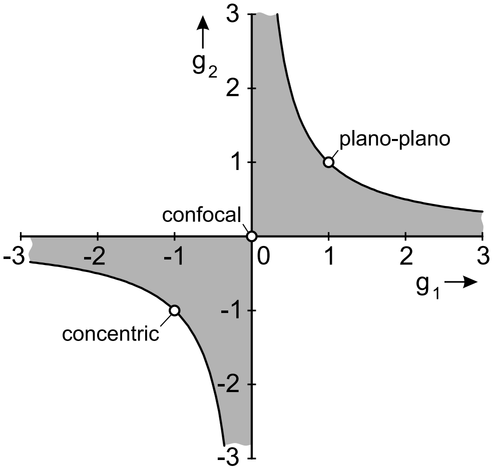

Figure 3.2: *Stability diagram or g_1-g_2-diagram for two-mirror optical resonators, where $g_{1,2} \equiv 1 - L/R_{1,2}$. The shaded region $0 \leq g_1 g_2 \leq 1$ contains all stable resonator configurations, where, in the paraxial limit, light remains confined inside a resonator. Indicated are the plano-plano, confocal and concentric resonator configurations.*

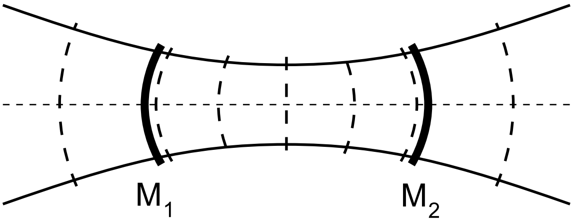

Figure 3.3: *Schematic indication of the wave fronts of the eigenmodes of a two-mirror resonator. At the two mirrors, the wave fronts must match the curvature of the mirrors.*

In Fig. 3.2 we plot the stability diagram for two-mirror resonators, where we have indicated three familiar configurations.

To find the eigenmodes of a resonator parametrised by g_1 and g_2, we require the curvature of the wave fronts at the mirrors to match the shape of those mirrors, as in Fig. 3.3. Then, the Rayleigh range z_R and the locations of the mirrors z_1 and z_2 are uniquely determined by the resonator length $L = z_2 - z_1$ and the radii of curvature of the mirrors R_1 and R_2. For the Gouy phase, only the ratios z_1/z_R and z_2/z_R are relevant. Expressed in terms of g_1 and g_2, these ratios are

$$\frac{z_{1,2}}{z_\mathrm{R}} = \frac{g_{2,1}(1-g_{1,2})}{\sqrt{g_1 g_2 (1 - g_1 g_2)}} \, . \tag{3.7}$$

Substituting Eq. (3.7) into Eq. (3.3) we find, after some algebra, that for the round trip Gouy phase

$$\theta = 2\arccos\left(\pm\sqrt{g_1 g_2}\right), \tag{3.8}$$

where the $+$ sign applies to $g_1, g_2 > 0$ and the $-$ sign to $g_1, g_2 < 0$. As we can see from Fig. 3.2, all resonators where g_1 and g_2 have different sign are unstable, and hence outside the scope of our discussion (see ref. [7], chapter 19).

Higher order Hermite-Gaussian or Laguerre-Gaussian modes acquire integer multiples of the fundamental round trip Gouy phase. For a Hermite-Gaussian mode with transverse mode indices m and n, or for a Laguerre-Gaussian mode with transverse mode indices p and l, the round trip Gouy phase is given by

$$\theta_{mn} = (m+n+1)\theta \text{ and } \theta_{pl} = (2p+l+1)\theta, \tag{3.9}$$

respectively. We may now relabel θ as θ_{00}; however, we will not do so but continue to use θ for the round trip Gouy phase of a fundamental Gaussian mode. The eigenfrequencies of a two-mirror paraxial resonator are then given by

$$\nu_{q,mn} = \frac{c}{2L}\left(q + \frac{\theta_{mn}}{2\pi}\right) = \frac{c}{2L}\left\{q + (m+n+1)\frac{\theta}{2\pi}\right\} \tag{3.10}$$

or the equivalent expression for Laguerre-Gaussian modes. The resulting spectrum consists, for every longitudinal mode index q, of combs of equidistant frequencies, where the distance between frequencies is the transverse mode spacing $\Delta\nu_{\mathrm{T}} = c/2L \cdot \theta/2\pi$. These combs are offset by the longitudinal mode spacing $\Delta\nu_{\mathrm{L}} = c/2L$, as illustrated in Fig. 3.4. In this figure, all transverse modes are indicated by bars of the same height. The sum of all combs is, in the absence of any mode selection mechanisms, an infinitely dense pattern of spikes. If one imposes an artificial limit on the maximum transverse order of modes, the resulting spectrum is very dense, but does not consist of equidistant resonances. In the presence of more realistic mode selection mechanisms, such as differences in gain or loss between the various transverse modes, eigenfrequency spectra will show amplitude structure (cf. Fig. 19.16 of ref. [7]).

We see that modes that have equal longitudinal mode indices q and equal sums of the transverse mode indices $m+n$ have the same frequency. Therefore, every eigenfrequency in the comb corresponding to a single value for q is a $(m+n+1)$-fold degenerate “family” of transverse modes. We label these families by their total transverse mode number $m+n$.

Because every frequency comb is offset by $\Delta\nu_{\mathrm{L}}$, a frequency interval with length $c/2L$ is the basic periodic block the eigenfrequency spectrum is built of. For historical reasons it is called the *free spectral range*. Because, in the range of large q, the spectrum is periodic, it is sufficient to consider a single free spectral range to get all spectral information.

3.2.2 Ray-optical perspective

To describe the ray behaviour of a paraxial two-mirror resonator, we consider a single plane containing the optical axis, and locally describe each ray by a vector $r = (x, x')$. This vector contains the distance of the ray to the axis x and its slope x' in a given reference plane perpendicular to the axis, as indicated in Fig. 3.5. Next, we calculate the round trip *ABCD*-matrix,

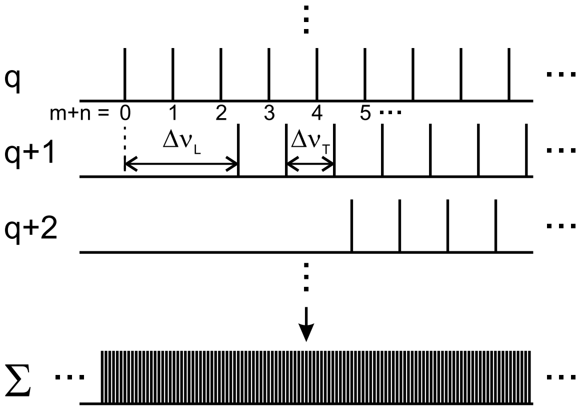

Figure 3.4: *Schematic representation of the structure of the eigenfrequency spectrum of a paraxial two-mirror resonator. Indicated are, for several values of q, the equidistant frequency combs, with a spacing between the peaks of $\Delta\nu_T$. The combs are offset by the longitudinal mode spacing $\Delta\nu_L$. Also indicated is the full spectrum resulting from summing over all possible values for q.*

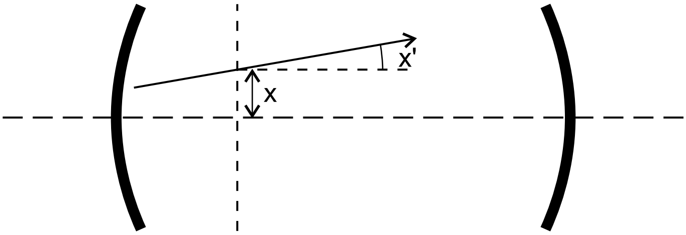

Figure 3.5: *Description of a light ray inside an optical resonator in terms of its distance to the optical axis and its slope, both taken in a given reference plane.*

where we choose mirror M_1 as reference plane. Propagation from mirror to mirror, over a distance L, is given by

$$\mathbf{M}_L = \begin{pmatrix} 1 & L \\ 0 & 1 \end{pmatrix}, \tag{3.11}$$

while the focusing effect of mirrors M_1 and M_2 is described by

$$\mathbf{M}_{1,2} = \begin{pmatrix} 1 & 0 \\ \dfrac{-2}{R_{1,2}} & 1 \end{pmatrix}. \tag{3.12}$$

The full round trip *ABCD*-matrix then equals

$$\mathbf{M}_{\mathrm{rt}} = \mathbf{M}_1 \mathbf{M}_L \mathbf{M}_2 \mathbf{M}_L = \begin{pmatrix} -1+2g_2 & 2Lg_2 \\ 2\dfrac{2g_1g_2 - g_1 - g_2}{L} & 4g_1g_2 - 2g_2 - 1 \end{pmatrix}, \tag{3.13}$$

where in the second step we have immediately rewritten everything in terms of g_1 and g_2. The eigenvalues for this round trip matrix are

$$\begin{aligned}\lambda_{1,2} &= 2g_1g_2 - 1 \pm 2\sqrt{g_1^2g_2^2 - g_1g_2} \\ &= 2g_1g_2 - 1 \pm 2i\sqrt{g_1g_2 - g_1^2g_2^2}\,,\end{aligned} \tag{3.14}$$

where, in the last step, we have used that the resonator is stable, so that $0 \leq g_1g_2 \leq 1$. In ray optics, a resonator is called stable when a paraxial ray that is injected into the resonator does not escape, but instead remains confined close to the axis of the resonator. Combining these expressions for the eigenvalues with Eq. (3.8) and standard trigonometric relations, we find

$$\lambda_{1,2} = \exp(\pm i\theta)\,, \tag{3.15}$$

with corresponding complex eigenvectors $r_{1,2}$. These complex eigenvectors do not themselves represent physical rays inside the resonator, but are introduced to ease the calculation, starting from an initial ray r_0, of the ray after n round trips in the resonator, described by the vector r_n. Any initial vector r_0 (where r_0 is, of course, real because it represents a physical ray inside the resonator) can be written as a linear combination of eigenvectors,

$$r_0 = c_1r_1 + c_2r_2\,, \tag{3.16}$$

with c_1 and c_2 suitable complex constants. Then, after n round trips inside the resonator we find

$$\begin{aligned} r_n = \mathbf{M}_{rt}^n r_0 &= \mathbf{M}_{rt}^n (c_1r_1 + c_2r_2) \\ &= c_1 \times \lambda_1^n r_1 + c_2 \times \lambda_2^n r_2 \\ &= c_1 \times \mathrm{e}^{in\theta} r_1 + c_2 \times \mathrm{e}^{-in\theta} r_2 \\ &= r_0 \cos n\theta + s_0 \sin n\theta \end{aligned} \tag{3.17}$$

where we have introduced the vector

$$s_0 \equiv i(c_1r_1 - c_2r_2)\,. \tag{3.18}$$

This last vector is a kind of “input slope vector”, and, because c_1 and c_2 are determined through Eq. (3.16), s_0 is real.

From Eqs. (3.10) and (3.17) we see that the Gouy phase θ plays a crucial role both in determining the spectral properties (in the case of a wave-optical treatment) and relating the positions and slopes of rays before and after a round trip through the resonator (in a ray-optical treatment). Since the ray behaviour of optical resonators rarely plays a prominent role in laser physics, this last aspect of the Gouy phase is often overlooked. However, as we will see in the next section, there are special resonator configurations where the dual nature of the Gouy phase leads to very surprising results.

3.3 *Degenerate* paraxial two-mirror resonators

The discussion in the previous section is valid for all possible values of the Gouy phase $0 \leq \theta \leq 2\pi$. However, when the Gouy phase is a rational number times 2π, that is $\theta = 2\pi K/N$

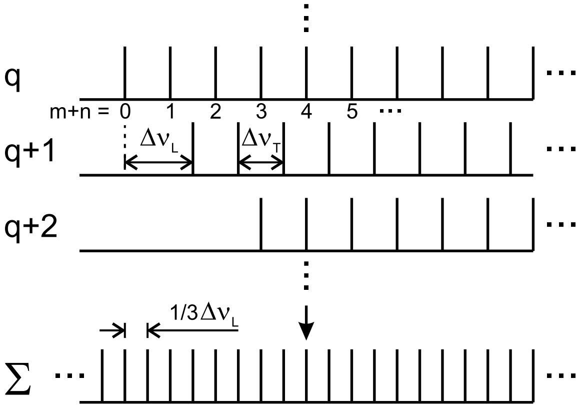

Figure 3.6: *Schematic representation of the structure of the eigenfrequency spectrum of a typical* degenerate *paraxial two-mirror resonator, with* $\theta = 2\pi \cdot 2/3$. *Indicated are, for three values of* q, *the equidistant frequency combs, with a spacing between the peaks of* $\Delta\nu_T = 2/3\Delta\nu_L$. *The combs are offset by the longitudinal mode spacing* $\Delta\nu_L$. *Also indicated is the full eigenfrequency spectrum, obtained from summing over all possible* q. *This full spectrum consists of equidistant resonances, spaced at* $1/3\Delta\nu_L$.

where K and N do not share common factors, these equations have unexpected consequences. Then, Eq. (3.10) can be rewritten to

$$\nu_{q,mn} = \frac{c}{2L}\left\{q + (m+n+1)\frac{K}{N}\right\} = \frac{c}{2LN}\{Nq + K(m+n+1)\}. \tag{3.19}$$

From this we see that raising the sum of the transverse mode indices $m+n$ by N, while at the same time lowering the longitudinal mode index q by K, will leave the resonance frequency unaltered, irrespective of the choice of q, m or n. Therefore, apart from the mode degeneracy within “families” of transverse modes mentioned in section 3.2.1, the resonator now also shows a degeneracy between different transverse mode families, separated by K in longitudinal mode index and N in total transverse mode index. The entire eigenfrequency spectrum collapses into these strongly degenerate clumps, spaced at $\Delta\nu = 1/N\,\Delta\nu_{\mathrm{L}} = c/2LN$, see Fig. 3.6. Thus, a single free spectral range will contain N of these degenerate clumps of modes, a fact that was first observed as early as 1964 [1]. We call such a resonator “fractionally degenerate”, or “degenerate” for short. A well known example of this kind of resonator is the confocal resonator with $K/N = 1/2$, a resonator configuration that is often used as optical spectrum analyser. In section 3.6 we shall consider the possibility of using this well-controlled distance between resonances to construct, for high N, a high-resolution interferometer.

The eigenfrequency spectrum of a degenerate resonator is quite different from that of a general resonator where $\theta = 2\pi p$, with p an irrational number. Then, no combination of lowering q and raising $m+n$ will lead to the same frequency, so that every transverse mode family, for every longitudinal mode index q, has its own unique frequency. As a result, a free spectral range will, in principle, be completely filled. In practice, however, there is a limit to how far m and n can be raised while remaining inside the paraxial approximation.

The eigenvalues of the round trip matrix of a resonator for which $\theta = 2\pi K/N$ follow from Eq. (3.15),

$$\lambda_{1,2} = \exp\left(\pm i 2\pi \frac{K}{N}\right), \tag{3.20}$$

so that the eigenvalues for n round trips equal

$$\lambda_{1,2}^{n} = \exp\left(\pm i n 2\pi \frac{K}{N}\right). \tag{3.21}$$

Then, from Eq. (3.17) we see that

$$\begin{aligned} r_N &= r_0 \cos\theta N + s_0 \sin\theta N \\ &= r_0 \cos N 2\pi \frac{K}{N} + s_0 \sin N 2\pi \frac{K}{N} \\ &= r_0 \end{aligned} \tag{3.22}$$

irrespective of the choice of initial ray r_0. Equivalently, for a system where $\theta = 2\pi K/N$, the *ABCD*-matrix for N round trips is the identity matrix

$$\mathbf{M}_{\mathrm{rt}}^{N} = \mathbb{1}. \tag{3.23}$$

Therefore, in such a resonator *any* paraxial ray will follow a trajectory that will close after N round trips. This is in contrast with a resonator with an “irrational” Gouy phase, where *no* ray (apart from the trivial ray along the optical axis) will ever follow a perfectly closed trajectory. Examples of periodic orbits for a resonator where $K/N = 1/4$ can be seen in Fig. 2.4 on page 7. In Fig. 3.7 we plot periodic orbits in a plano-concave resonator for which $\theta = 2\pi K/N$, with $K/N = 1/3$, $1/4$ and $2/5$, respectively. The choice for a plano-concave resonator was made to ease drawing of the orbits, and does not limit the generality of what follows.

We see that for degenerate resonators, we can distinguish two basic classes of periodic orbits. The first class consists of generic orbits, where the ray never strikes a mirror at normal incidence, such as in Figs. 3.7b and e. The second class consists of *reciprocating* orbits, where the orbit strikes a mirror at normal incidence, reverses direction and re-traces itself, as in Figs. 3.7a, c, d, and f. Obviously, the number of vertices where the orbit strikes the mirror at normal incidence is either 0 or 2. For resonators with even N, these vertices will always lie on the same mirror, allowing us to further subdivide the class of reciprocating orbits into those that have normal-incidence vertices on either mirror M_1 or M_2. For resonators with odd N, these vertices cannot lie on the same mirror, so that such a subdivision is not possible. We stress again that, in the paraxial case, *every* initial ray will form a closed orbit, as illustrated in Fig. 3.8. As such, there are infinitely many different periodic orbits for any of the mentioned five types.

As mentioned above, and clearly visible in Fig. 3.7, a periodic orbit for a resonator with $\theta = 2\pi K/N$ will make N round trips in the resonator, before closing on itself. In addition to that, K determines the number of *transverse* “round trips” an orbit will make before closing,as

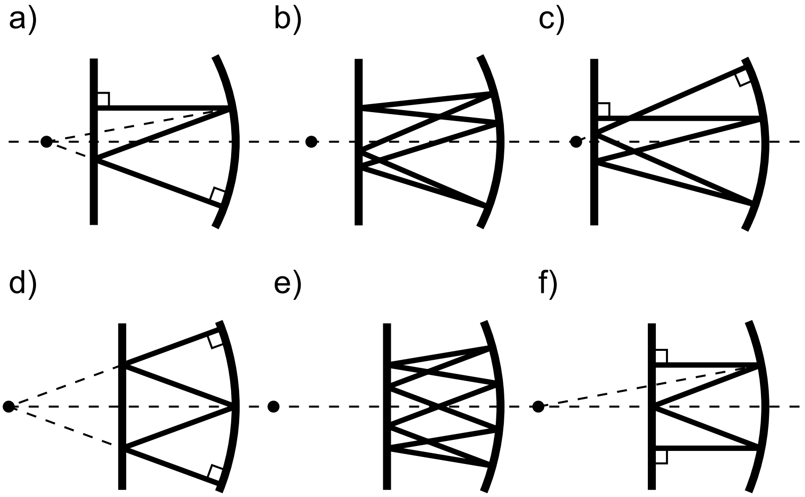

Figure 3.7: *Typical closed periodic orbits in degenerate resonators. (a) $K/N = 1/3$, reciprocating path ("Z-shaped"), (b) $K/N = 1/3$, generic path, (c) $K/N = 2/5$, reciprocating path, (d) $K/N = 1/4$, reciprocating path ("W-shaped"), (e) $K/N = 1/4$, generic path, (f) $K/N = 1/4$, reciprocating path ("M-shaped").*

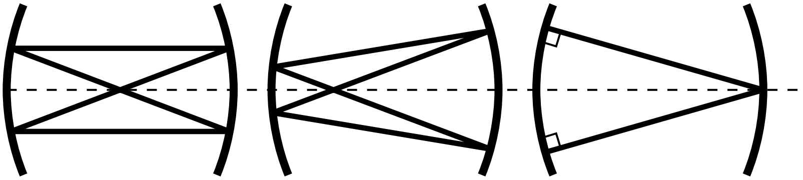

Figure 3.8: *Paraxial confocal resonator, for which $K/N = 1/2$. Several closed periodic orbits, with different initial conditions, are displayed. All these orbits have equal round trip length.*

can be seen, for example, in Fig. 3.7c, where $K/N = 2/5$. That this must be so follows from the eigenvalues of the round trip matrix for n round trips, $\lambda_{1,2}^{n} = \exp\left(\pm i n 2\pi K/N\right)$: if we represent these eigenvalues on the complex unit circle, we will make K full revolutions before coming to $\lambda_{1,2}^{N} = \exp\left(\pm i 2\pi K\right) = 1$.

As a result, a resonator with a "rational" Gouy phase will, at the same time, show a highly degenerate eigenfrequency spectrum (wave perspective) and support closed periodic orbits (ray perspective). As demonstrated in chapter 2, a strong mode selection mechanism in a laser can make both effects highly visible. There, we operate a laser with a plano-concave resonator at a length so that $\theta = 2\pi \cdot 1/4$. Pumping the laser off-axis selects a subset of modes, all belonging to the same family $m+n$. This linear combination of Hermite-Gaussian modes then results in the W-shaped geometric mode of Fig. 2.3. If we tune the laser to select a different transverse mode family, say $m+n+1$, we get the same overall W-shape.

3.4 Degenerate *nonparaxial* two-mirror resonators

3.4.1 Presence of periodic orbits

As we saw in the previous section, within the paraxial approximation every resonance will be part of a degenerate group of modes. This presupposes that one can increase the transverse mode indices m and n infinitely without violating the paraxial approximation. That this cannot be the case follows from the fact that the far field opening angle α of a higher order Hermite-Gaussian beam scales with $\sqrt{m}$ (where the transverse mode index m refers to the plane of the largest opening angle). For large enough m, this opening angle will be so large that we violate the paraxial approximation.

Similarly, in a ray-optical description of a resonator with $\theta = 2\pi K/N$, within the paraxial approximation *every* initial ray will repeat itself and follow a closed orbit after N orbits. However, this assumes the validity of the *ABCD*-matrix formalism; when the angles between rays and the optical axis become too large, this no longer holds. An alternative way of phrasing this is that, instead of being constants, the coefficients in a nonparaxial "*ABCD*-matrix" depend on the position and slope of the ray under consideration. Even in drawing the periodic orbits of, for example, Fig. 3.7, some artistic freedom was needed to get perfectly closed trajectories.

In this section we will consider what happens to the closed periodic orbits of degenerate resonators when we make those resonators nonparaxial, and from there try to draw conclusions concerning the behaviour of the Gouy phase for nonparaxial eigenmodes. We will show that, in nonparaxial resonators, the Gouy phase no longer is a global property, describing the behaviour of all eigenmodes and all rays. Instead, it becomes a *local* property: every ray has its own Gouy phase, just like every eigenmode has its "own" Gouy phase, which can no longer be written as $\theta_{mn} = (m+n+1)\theta$.

One may wonder whether periodic orbits exist at all outside the paraxial limit. Referring to the classification introduced in the previous section, it is easy to show that it is always possible to modify the length of a resonator so that it will still support a reciprocating periodic orbit. To start, choose one of the two vertices at normal incidence to one of the two mirrors, and trace $N/2$ round trips through the resonator, as in Fig. 3.9. Then, when we vary the length of the resonator, the position and angle of incidence of the last vertex will vary continuously. The angle with the optical axis can be both positive and negative, and as a result, it must be equal to zero for a particular resonator length. This, then, is the resonator length for which a reciprocating periodic orbit, with period N and a particular choice of location of one of the vertices, is possible.

It is not *a priori* clear whether *generic* (instead of reciprocating) periodic orbits are possible outside the paraxial limit, since then not only angles but also positions must be made to match. Numerical results that will be presented in Fig. 3.12 suggest that, at least for $K/N = 1/3$, such nonparaxial generic periodic orbits do indeed exist.

From the preceding discussion we see that, in order to support a nonparaxial reciprocating periodic orbit, the length of a resonator must be adjusted relative to the length of a degenerate paraxial resonator. The change in length will generally depend on the exact shape and size of the periodic orbit. As such, periodic orbits can become isolated, or "localised", in the sense that for every resonator length L, there is only one (or possibly two, due to symmetry)

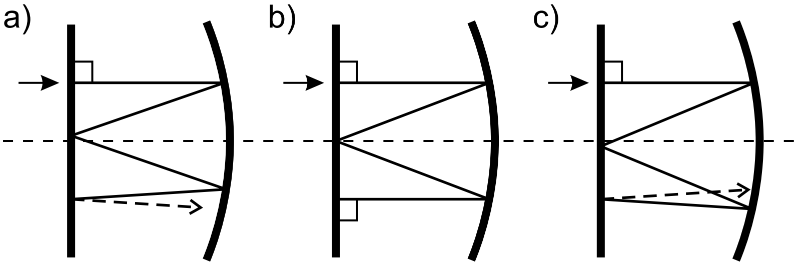

Figure 3.9: *Resonator configurations that are (a) too short, (b) precisely correct, and (c) too long to support a nonparaxial $K/N = 1/4$ periodic orbit. The arrow indicates the vertex that is kept fixed.*

specific periodic orbit with period N. This is in sharp contrast with paraxial periodic orbits, where every possible paraxial periodic K/N-orbit is supported at the same resonator length $L_{K,N,\mathrm{parax}}$.

The first orbit we shall consider is the W-shaped orbit of a plano-concave resonator as shown in Fig. 3.7d. In such a resonator, the topmost and bottommost segments of the orbit are radial to the concave mirror, while the middle two segments must meet at the apex, the intersection of the concave mirror and the optical axis. Reflection in the flat mirror shows that the middle two segments always intersect at the mirror image of the centre of curvature of the concave mirror. Therefore, for such a W-shaped path, the mirror image of the centre of the concave mirror and the apex of the concave mirror must coincide, irrespective of the opening angle of the periodic orbit. As a result, to support both paraxial and nonparaxial W-shaped orbits, the distance between flat and concave mirror must be $R/2$ (this is called a hemiconfocal resonator). In the light of the previous paragraphs this is a very surprising result: no matter how large the angles with the optical axis are, a resonator with a length $R/2$ will support a periodic orbit with period 4. We will see below that this is indeed a very special case.

The second orbit we shall consider is the M-shaped orbit of Fig. 3.7f. Here, no segments of the orbit are radial to the concave mirror. Instead, the top and bottom segments are perpendicular to the flat mirror, and the middle two segments meet at the flat mirror. As a parameter for the nonparaxiality of the M-shaped orbit we shall choose the angle between the middle segments and the optical axis, α (see Fig. 3.10a). Straightforward trigonometry then shows that such an M-shaped periodic orbit is supported by a plano-concave resonator with a length

$$L_{1/4,\mathrm{M}} = R\left\{1 - \frac{1}{2}\left(\cos\frac{\alpha}{2}\right)^{-1}\right\}. \tag{3.24}$$

For $\alpha \to 0$ we retrieve the result for paraxial orbits, $L_{1/4,\mathrm{M}} \to R/2$. In Fig. 3.10a we have drawn two such M-shaped orbits, for different angles α.

The last orbit we shall consider is the Z-shaped reciprocating orbit of Fig. 3.7a, for $K/N = 1/3$. This orbit has one segment, the bottommost, radial to the concave mirror, while the topmost segment is perpendicular to the flat mirror. As parameter we choose the angle α between the bottommost, radial, segment and the optical axis (see Fig. 3.10b). After slightly

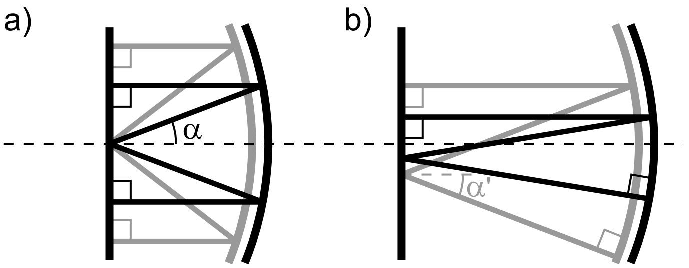

Figure 3.10: *Resonator configurations that support nonparaxial reciprocating orbits, for two different angles α each. (a) M-shaped periodic orbit for $K/N = 1/4$, (b) Z-shaped periodic orbit for $K/N = 1/3$. Black drawing: small α, grey drawing: large α. We see that for increasing α the resonator length becomes smaller.*

more complicated trigonometry than before we find that such orbits are possible in a plano-concave resonator with a length

$$L_{1/3,\mathrm{rec}} = R\left\{1 - \frac{1}{4}\left(\cos\frac{\alpha}{2}\right)^{-1}\right\}, \tag{3.25}$$

an expression that only differs from Eq. (3.24) in the factor $1/4$ instead of $1/2$ before the angle-dependent term. The similarity between these expressions suggests that, for a plano-concave resonator, the length L at which that resonator supports a particular nonparaxial reciprocating orbit, with at least one perpendicular hit on the flat mirror, is given by

$$L_{K/N,\mathrm{rec}} = R\left\{1 - \left(1 - \frac{L_{K/N,\mathrm{parax}}}{R}\right)\left(\cos\frac{\alpha}{2}\right)^{-1}\right\}, \tag{3.26}$$

where $L_{K/N,\mathrm{parax}}$ is the resonator length at which the *paraxial* K/N-orbit is closed. For a plano-concave resonator, $g_1 = 1$ and $g_2 = 1 - L/R$, so that, from rewriting Eq. (3.8), we find

$$g_1 g_2 = 1 - \frac{L}{R} = \left(\cos\frac{\theta}{2}\right)^2 \Rightarrow L_{K/N,\mathrm{parax}} = R\left(\sin\pi\frac{K}{N}\right)^2. \tag{3.27}$$

We will now explore the validity of our Ansatz Eq. (3.26). Generally, in the case of N even, it is not immediately clear where α should be chosen. A trial on a periodic orbit for $K/N = 1/6$ shows that *none* of the likely angles in the periodic orbit will result in the correct resonator length. In fact, it is rather trivial to show that for a $K/N = 1/6$ orbit that has its turning points on the flat mirror, the correct length is given by $1/2 \cdot L_{1/4,\mathrm{M}}$. Then, the vertex that, for $K/N = 1/4$, was at the intersection of the flat mirror and the axis will be reflected to the apex of the concave mirror, as sketched in Fig. 3.11. The vertices that strike the flat mirror at normal incidence are unaffected by the change in length. Because such an $1/6$-orbit can be derived from an M-shaped $1/4$-orbit, we shall refer to it as a *folded-M* orbit.

For N odd, the results from our Ansatz are equally disappointing. Choosing α as the angle between the segment that is radial to the concave mirror and the optical axis, Eq. (3.26) gives incorrect results for $K/N = 1/5$ and $K/N = 1/7$, as we have verified numerically.

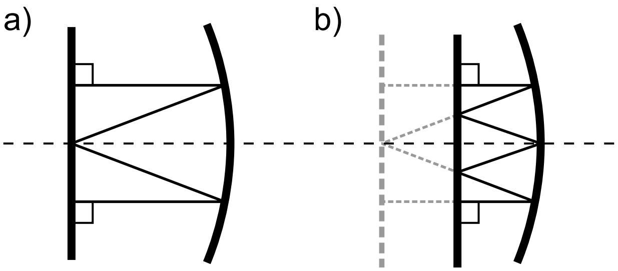

Figure 3.11: *(a) Nonparaxial M-shaped orbit for* $K/N = 1/4$*, (b) Nonparaxial orbit for* $K/N = 1/6$*. We see that the cavity length at which such an* $1/6$*-orbit is supported is* half *the cavity length at which an M-shaped* $1/4$*-orbit with the same slopes is supported.*

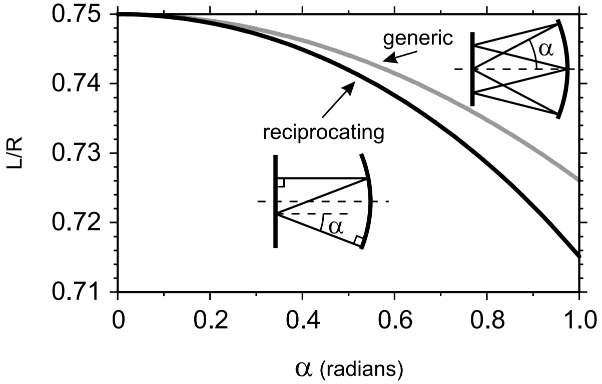

Figure 3.12: *Resonator lengths at which nonparaxial* $K/N = 1/3$*-periodic orbits are possible for (Z-shaped) reciprocating orbits (black) and symmetric generic orbits (grey). Indicated are the choices of angle* α *to parametrise the different orbits.*

Because the equations rapidly become intractable as soon as an orbit has an appreciable number of segments and vertices, it has not been possible to find expressions for the length of resonators that support reciprocating periodic orbits for $N > 4$ (with the exception of one variant for $N = 6$), or generic periodic orbits for any N. Numerically solving the propagation equations for generic $K/N = 1/3$ periodic orbits that are symmetric with respect to the optical axis suggest that these orbits are possible at suitable resonator lengths. In Fig. 3.12 we plot the resonator length at which such symmetric generic periodic orbits with $K/N = 1/3$ are possible, as well as the appropriate resonator length for reciprocating $K/N = 1/3$-orbits, as a function of angle α. Further study is needed to extend this to nonsymmetric generic orbits and different K/N.

All of the above considerations regarding the behaviour of nonparaxial periodic orbits suggest that determining the Gouy phase for nonparaxial eigenmodes is a far from trivial undertaking. We saw that, in general, to support nonparaxial periodic K/N-orbits, the length of a resonator must be *reduced* compared to the length at which it supports paraxial K/N-

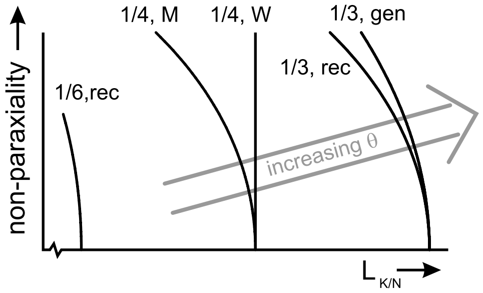

Figure 3.13: *Schematic representation of the behaviour of the Gouy phase as a function of the degree of nonparaxiality. The curves indicate resonator lengths at which certain periodic orbits are possible, and hence serve as lines of constant Gouy phase for those specific periodic orbits.*

orbits, as schematically indicated in Fig. 3.13. Since the Gouy phase increases with increasing length, another way of phrasing this effect is that the effective Gouy phase *increases* with increasing nonparaxiality; then, if we want to keep the Gouy phase constant when increasing the degree of nonparaxiality, we must reduce the length of the resonator.

The required change in length depends on the exact shape of a nonparaxial periodic orbit. We saw that the dependence of L on α is quite different for the $K/N = 1/4$ M- and W-shaped orbits, and also for the reciprocating and symmetric generic $K/N = 1/3$-orbit. Therefore, it is likely that the Gouy phase that will be acquired by a nonparaxial eigenmode of an optical resonator will strongly depend on the profile of that eigenmode. Nevertheless, from the above we can conclude that nonparaxial eigenmodes will have a Gouy phase that is *higher* than $\theta_{mn} = (m+n+1)\theta$, the result for paraxial eigenmodes. As a result, the simple structure of the degenerate eigenfrequency spectrum as described by Eq. (3.19), as well as the structure of the nondegenerate eigenfrequency spectrum described by Eq. (3.10), will be lost when we go beyond the paraxial approximation.

3.4.2 Stability of periodic orbits

To assess the stability of the nonparaxial periodic orbits discussed above, we must calculate the corresponding *monodromy matrices* $\mathbf{M}_\mathrm{m}$ (see, for example, section 7.2.5 of ref. [15]). In general the monodromy matrix describes the linearised evolution of a trajectory that deviates slightly from a given trajectory; such deviations can be either in ray angle or in ray position. As such, the monodromy matrix takes on the role of “round trip” *ABCD*-matrix for deviations, relative to a given orbit. For periodic orbits, we consider the evolution of small deviations after a *complete* circuit of such a periodic orbit, so that the concept “round trip” now refers to such a complete circuit, rather than to a *cavity* round trip. For paraxial trajectories and orbits, the monodromy matrix is identical to the *ABCD*-matrix; for nonparaxial trajectories and orbits it requires precise knowledge of the slope and length of every segment of the trajectory or orbit under consideration.

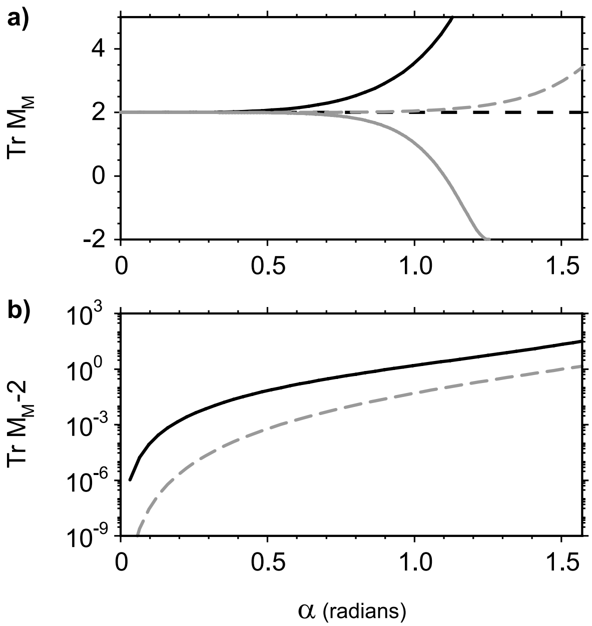

Figure 3.14: *(a) Trace of the monodromy matrix* $\mathrm{Tr}\,\mathbf{M}_m$ *for the M-shaped orbit for* $K/N = 1/4$ *of Fig. 3.7f (solid black curve), the folded-M orbit for* $K/N = 1/6$ *of Fig. 3.11b (solid grey curve), the W-shaped orbit for* $K/N = 1/4$ *of Fig. 3.7d (dashed black curve), and the Z-shaped orbit for* $K/N = 1/3$ *of Fig. 3.7a (dashed grey curve). (b) Difference* $\mathrm{Tr}\,\mathbf{M}_m - 2$ *for the M-shaped orbit for* $K/N = 1/4$ *(solid black curve) and the Z-shaped orbit for* $K/N = 1/3$ *(dashed grey curve), plotted on a logarithmic scale. Note that these are the same two orbits as plotted in (a), with corresponding line types. The angle* α *is the slope of the nonhorizontal segment of the orbit, as indicated in Figs. 3.10a and b.*

The stability of a periodic orbit can then be deduced from the trace of the monodromy matrix for that orbit, $\mathrm{Tr}\,\mathbf{M}_\mathrm{m}$:

$$|\mathrm{Tr}\,\mathbf{M}_\mathrm{m}| \leq 2 \text{ for stable orbits,} \tag{3.28a}$$

$$|\mathrm{Tr}\,\mathbf{M}_\mathrm{m}| > 2 \text{ for unstable orbits.} \tag{3.28b}$$

For paraxial periodic orbits of period N the monodromy matrix is equivalent to the *ABCD*-matrix for a complete circuit of N round trips through the cavity. From Eq. (3.23) we then find that

$$\mathbf{M}_\mathrm{m} = \mathbf{M}_\mathrm{rt}^N = \mathbb{1}\,, \tag{3.29}$$

so that $\mathrm{Tr}\,\mathbf{M}_\mathrm{m} = 2$, independent of any of the parameters of the orbit. Thus, paraxial periodic orbits are always stable, albeit marginally stable.

In the nonparaxial case we must calculate the trace of the monodromy matrix of every periodic orbit separately. In Fig. 3.14a we plot $\mathrm{Tr}\,\mathbf{M}_\mathrm{m}$ for four nonparaxial periodic orbits, namely the Z-shaped reciprocating orbit for $K/N = 1/3$ of Fig. 3.7a (dashed grey curve), the

W-shaped reciprocating orbit of Fig. 3.7d (dashed black curve), the folded-M reciprocating orbit for $K/N = 1/6$ of Fig. 3.11b (solid grey curve) and the M-shaped reciprocating orbit of Fig. 3.7f (solid black curve). The angle α is the slope of the nonhorizontal segments of the orbit (cf. the choice of α in Figs. 3.10a and b). We see that for finite angles α, i.e., for nonparaxial orbits, $\mathrm{Tr}\,\mathbf{M}_\mathrm{m} > 2$ for both the Z-shaped $1/3$ and the M-shaped $1/4$-orbits. We conclude that these nonparaxial orbits are *unstable*. In Fig. 3.14b we plot $\mathrm{Tr}\,\mathbf{M}_\mathrm{m} - 2$ for these two orbits, to better show the deviation from 2 for small α.

From the black dashed curve in Fig. 3.14a we see that for the W-shaped $1/4$-orbit, $\mathrm{Tr}\,\mathbf{M}_\mathrm{m} = 2$, independent of the angle α. The grey dashed curve shows that for the folded-M $1/6$-orbit, $|\mathrm{Tr}\,\mathbf{M}_\mathrm{m}| < 2$ (Note that for α larger than $4\pi/10 \approx 1.26$ radians, such an $1/6$-orbit is no longer possible). Therefore, these orbits are stable both within and outside the paraxial approximation, unlike the other two orbits under consideration. As we see from the results for these four orbits, we cannot make general statements about the stability of nonparaxial periodic orbits.

An interesting comment is as follows. For nonparaxial periodic orbits, the resonator length at which a particular periodic orbit is possible depends on both the ratio K/N *and* the exact geometry of that periodic orbit; therefore, it is possible that a resonator of a certain length supports periodic orbits of *different* period N at the same time. For paraxial resonators, a particular resonator length either supports only periodic orbits with the same K/N, or no periodic orbits at all.

3.5 Folded three-mirror resonators

A more complicated optical resonator than the two-mirror resonators considered so far is a folded three-mirror resonator. Our interest in this type of resonator stems from the fact that, as we will see in chapter 5, *nonparaxial* three-mirror resonators show wave-chaotic behaviour. Here, we will lay the groundwork for the understanding of *paraxial* three-mirror resonators.

In Fig. 3.15a we draw a simple folded three-mirror resonator. It is essential that the folding mirror M_F is a curved mirror. If not, the resonator can be trivially transformed back into a two-mirror resonator, as in Fig. 3.15b. Because of the non-normal incidence on the folding mirror, the effective radius of curvature of that mirror, and hence the focal power, will be different for different planes containing the axis. Here, it is sufficient to consider the behaviour in two perpendicular planes, both containing the optical axis, the so called principal planes.

The first of these is the plane defined by the two segments of the optical axis. This is customarily called the *tangential* plane, and the effective radius of curvature of the folding mirror in this plane is [7]

$$R_\mathrm{T} = R \cdot \cos\alpha\,. \tag{3.30}$$

When the folding angle 2α increases, R_T will decrease and hence the focusing effect of the folding mirror in the tangential plane will increase.

The second plane is the plane perpendicular to the tangential plane and containing the optical axis. Because the optical axis is folded, this plane is, in real space, folded as well. Customarily, it is called the *sagittal* plane. The effective radius of curvature of the folding

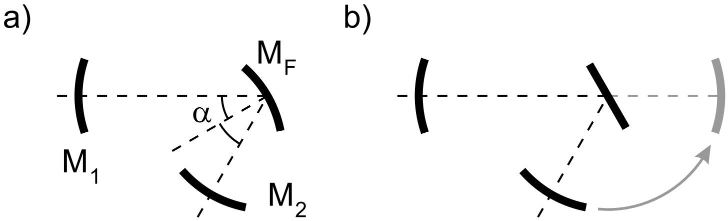

Figure 3.15: *(a) Schematic drawing of a three-mirror folded resonator. M_F is the curved folding mirror, M_1 and M_2 are the resonator end mirrors. The resonator is folded through 2α, so that the angle of incidence of the axis on the folding mirror M_F is α. (b) A three-mirror folded resonator with a flat folding mirror, which can be trivially transformed back into a two-mirror resonator.*

mirror in this plane is [7]

$$R_{\mathrm{S}} = R/\cos\alpha\,, \tag{3.31}$$

so that, for increasing folding angle 2α, R_{S} will increase and hence the focal power will decrease.

As a result, the total focal power in a single round trip through the resonator depends on whether one considers the tangential or the sagittal plane. A direct consequence of this is that the eigenmodes of a paraxial three-mirror resonator are astigmatic Hermite-Gaussian modes, with generally an elliptical cross-section. Also, instead of a single Gouy phase θ to describe the structure of, for example, the eigenfrequency spectrum (cf. Equation (3.10)), we now have *two* Gouy phases, one each for the tangential and the sagittal planes.

The eigenfrequencies of the astigmatic Hermite-Gaussian eigenmodes of a folded three-mirror resonator are given by [7, 16]

$$\nu_{q,mn} = \frac{c}{2L}\left\{q + \left(m+\tfrac{1}{2}\right)\frac{\theta_{\mathrm{T}}}{2\pi} + \left(n+\tfrac{1}{2}\right)\frac{\theta_{\mathrm{S}}}{2\pi}\right\}, \tag{3.32}$$

where θ_{T} and θ_{S} are the Gouy phases for the tangential and the sagittal plane, respectively. These Gouy phases depend on the folding angle 2α of the resonator; the easiest way of determining θ_{T} and θ_{S} is to compose the round trip matrices $\mathbf{M}_{\mathrm{rt,T}}$ and $\mathbf{M}_{\mathrm{rt,S}}$, using the appropriate effective radii of curvature of Eqs. (3.30) and (3.31) for the folding mirror. The eigenvalues of these round trip matrices will then be $\exp(\pm i\theta_{\mathrm{T}})$ and $\exp(\pm i\theta_{\mathrm{S}})$. In Fig. 3.16 we plot θ_{T} and θ_{S} versus half folding angle α, for a resonator with three mirrors with a radius of curvature $R = 1$ m. One arm of the resonator has a length $L_1 = 10$ cm, while the other arm has a length $L_2 = 20$ cm. These dimensions are taken from chapter 5, where we will demonstrate, for large enough α, the presence of wave chaos in such a resonator.

We can re-order the terms in Eq. (3.32) to get the more practical form

$$\begin{aligned}\nu_{q,mn} &= \frac{c}{2L}\left\{q + (m+n+1)\frac{\theta_{\mathrm{T}}+\theta_{\mathrm{S}}}{4\pi} + (m-n)\frac{\theta_{\mathrm{T}}-\theta_{\mathrm{S}}}{4\pi}\right\}\\ &= \frac{c}{2L}\left\{q + (m+n+1)\frac{\hat{\theta}}{2\pi} + \frac{(m-n)}{2}\frac{\delta}{2\pi}\right\},\end{aligned} \tag{3.33}$$

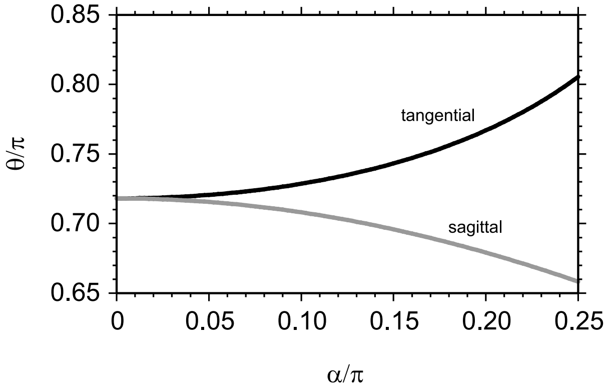

Figure 3.16: *Tangential and sagittal Gouy phases* θ_T *and* θ_S *versus half folding angle* α*, for a folded three-mirror resonator consisting of three mirrors with radius of curvature* $R = 1$ m. *The length of one arm of the resonator* $L_1 = 10$ cm*, while the length of the other arm* $L_2 = 20$ cm.

where we have introduced the average Gouy phase $\hat{\theta} = (\theta_{\mathrm{T}} + \theta_{\mathrm{S}})/2$ and the Gouy phase difference $\delta = \theta_{\mathrm{T}} - \theta_{\mathrm{S}}$. Using this equation we see that the eigenfrequency spectrum of a paraxial folded three-mirror optical resonator has a more interesting structure than that of a two-mirror resonator. For every longitudinal mode index q there is a “super-family”, an equidistant series of mode families with constant total transverse mode index $m+n$. The centres of each family are spaced at $\Delta\nu_{\mathrm{F}} = \hat{\theta}/2\pi \cdot c/2L$, similar to the transverse mode spacing $\Delta\nu_{\mathrm{T}}$ for a two-mirror resonator. However, for a three-mirror resonator the frequency degeneracy *within* a family of modes is lifted, so that every family consists of $m+n+1$ distinct peaks. From Eq. (3.33) we see, after noting that for a family of modes $m+n$ is a constant so that the difference $m-n$ can only change in steps of 2, that the distance between the different members of a single family is equal to $\Delta\nu_{\mathrm{M}} = \delta/2\pi \cdot c/2L$. Finally, to get the complete eigenfrequency spectrum we must combine all super-families of modes, each with their specific q, where neighbouring super-families are offset by $\Delta\nu_{\mathrm{L}} = c/2L$, the longitudinal mode spacing.

Similar to the two-mirror resonators described in section 3.3, it is possible to construct a folded three-mirror resonator that has one or both of the Gouy phases θ_{T} and θ_{S} equal to a rational fraction of 2π. However, to get degenerate eigenfrequency spectra, *both* Gouy phases must have this form, as what matters is the average and difference Gouy phases $\hat{\theta}$ and δ. This double degeneracy only occurs in a very small part of parameter space.

On the other hand, it *is* possible to have periodic orbits in a resonator with only one Gouy phase (θ_{T} or θ_{S}) of the form $2\pi K/N$, provided the analysis is limited to the plane (tangential or sagittal) for which the Gouy phase has this rational form. When both Gouy phases $\theta_{\mathrm{T,S}} = 2\pi K/N$, possibly with different K/N for the two planes, we again get a plethora of periodic orbits, now with a period that is the least common multiple of N_{T} and N_{S}.

When we operate a folded three-mirror optical resonator in the nonparaxial regime, we can expect, for the tangential and sagittal planes, effects that are similar to those described in section 3.4 for nonparaxial two-mirror resonators, both degenerate and nondegenerate. However, because we now deal with two separate Gouy phases, each with their own dependence on the degree of nonparaxiality, analysing this is beyond the scope of this chapter. It is likely that, because of nonparaxiality, it is no longer allowed to consider the tangential and sagittal planes independently, but that instead they become coupled. Also, as we will see in chapter 5, it appears that the effect of nonparaxiality is enhanced by the folding of the resonator.

3.6 Degenerate resonator as high-resolution interferometer

As we saw in section 3.3, a degenerate two-mirror optical resonator has an eigenfrequency spectrum consisting of evenly spaced resonances, with an inter-resonance distance of $\Delta\nu = 1/N \cdot c/2L$. The best known example of such a degenerate resonator is a *confocal* Fabry-Pérot resonator, with $N = 2$, as already mentioned on page 21. Here, we will consider resonators with much larger N.

We may consider using such a degenerate resonator as a high-resolution interferometer for sensing changes in length, as changing the length of the resonator will shift its resonance frequencies. If we inject monochromatic light at a fixed frequency ν_0 into a resonator, and monitor the amount of transmitted light as the length of the resonator changes, we will see maximum transmission when a resonator eigenfrequency coincides with the frequency of the injected light. To first approximation, the eigenfrequencies of a resonator change linearly with the length of the resonator, and changing the length of the resonator by $\lambda/2$, where λ is the wavelength of the injected light, will shift all frequencies by $\Delta\nu_\mathrm{L} = c/2L$, a single free spectral range.

In a traditional standing wave interferometer, the injected light is mode-matched to a single eigenmode of the resonator, the fundamental Gaussian mode. Then, changing the length of the resonator over a range $\lambda/2$ will bring you from one resonance to the next. There are two notable exceptions to this: the planar Fabry-Pérot interferometer, which only requires plane wave incidence, and the confocal interferometer, where no mode matching is required. However, these two types of interferometer are, in essence, degenerate resonators, with $K/N = 0$ and $K/N = 1/2$, respectively.

For a degenerate resonator where the distance between resonances is $1/N \cdot c/2L$, that is, a factor of $1/N$ smaller than for nondegenerate mode-matched interferometers, the change in length of the resonator required to get from one resonance to the next is *also* a factor $1/N$ smaller, $\delta L = 1/N \cdot \lambda/2$, and the value of N can be controlled, and calibrated, to high accuracy. Then, it is possible to detect changes in the length of such a resonator with an accuracy of at least $1/N \cdot \lambda/2$, over a large range of length changes ΔL.

In reality, conventional, nondegenerate resonators also offer a resolution that is higher than the fundamental mode spacing $\lambda/2$. Because the intensity reflectivity of the mirrors $\mathscr{R}_{1,2} < 1$, every resonance has a finite width $\delta\nu$ (FWHM). The ratio of the free spectral range to this line width is called the finesse $\mathscr{F}$, and is, for $\mathscr{R}_{1,2}$ close to 1, given by

$$\mathscr{F} \equiv \frac{c}{2L}\frac{1}{\delta\nu} = \frac{2\pi}{1-\mathscr{R}}\,, \tag{3.34}$$

with $\mathscr{R} = \mathscr{R}_1\mathscr{R}_2$. Through this finite line width, combined with knowledge about the exact shape of the resonance line, one can detect length changes that can, potentially, be much smaller than $\lambda/2$. However, a crucial difference with a degenerate resonator is that the *total* range of resonator lengths ΔL in which it is possible to detect small length changes is of the order of the width of an individual resonance. As soon as one is outside the wing of a modal resonance, one cannot determine the length of the resonator or changes therein. If, by reducing the line width of individual resonances, one wishes to improve the resolution of an interferometer, one reduces at the same time the useful range over which one can determine those minute length changes. One possible way to overcome this problem is to change the frequency of the injection laser. However, in that case it is no longer possible to lock the laser frequency to an atomic transition in order to achieve a very precise reference frequency, thus leading to loss of accuracy in the length measurement.

In contrast, a degenerate resonator allows one to apply the above procedure to all N resonances within a single free spectral range. One can detect large length changes, simply by counting the number of resonances that are brought into alignment with the injection laser frequency. Subsequently, small length changes can be determined by detecting the flank of individual resonances. Large length changes that are not equal to an integer times the spacing of individual resonances $1/N \cdot \lambda/2$, can be trivially broken up in a part that *is* equal to an integer times the fundamental line spacing, and a small length change. As both N and the laser wavelength λ can be precisely calibrated, any length change can be accurately determined. In effect, a degenerate resonator, in combination with an injection laser that is frequency-locked to an atomic transition, creates a well-calibrated “comb” of resonances.

An added advantage of a degenerate resonator is its insensitivity to mode matching. Since, for a degenerate resonator, *all* modes are condensed into degenerate groups, it is in fact essential to have nonperfect mode matching, as mode matching to a single resonance will destroy the increased mode density in the transmission spectrum. This effect is well known for confocal resonators, where neighbouring degenerate super-families consist of modes that are either even or odd with respect to the optical axis. Centreing a symmetric and even beam on such a resonator will cause the overlap with the odd super-families to be zero, so that the resulting transmission spectrum will have the basic $c/2L$ periodicity, instead of $c/4L$.

There are several limitations to using a degenerate optical resonator as a high-resolution interferometer. The first is that a resonator is only perfectly degenerate at a *single* resonator length $L_{K/N}$. Changing this length, even by tiny fractions of $\lambda/2$, will destroy this perfect degeneracy. In practice, this lack of degeneracy will only become significant when it is larger than the line width of individual resonances. As every degenerate group of resonances consists of modes with the same $(m+n) \mod N$, the distance between the extreme modes in a slightly nondegenerate group will be proportional to $(m+n)_{\text{max}} - (m+n)_{\text{min}} = kN$, where k is the number of resonances within a group. Therefore, it may be beneficial to limit the total number of resonances within a group.

A second limitation is that it is not possible to increase N at will. To get a nicely developed degenerate spectrum, with inter-resonance spacing $1/N \cdot c/2L$, one wishes to excite more than N families of modes, each with constant $(m+n)$. However, as we saw in section 3.4, it is not possible to increase $(m+n)$ indefinitely without violating the paraxial approximation. Outside the paraxial approximation, eigenmodes will have a round trip Gouy phase that is *larger* than $\theta_{mn} = (m+n+1)\theta$, so that, for a resonator with $\theta = 2\pi K/N$, the perfect degeneracy that exists for paraxial modes is absent for nonparaxial modes.

In practice, this limitation is not very strict. The opening angle of a fundamental Gaussian mode is given by

$$\alpha_0 = \frac{\lambda}{\pi w_0} \, , \tag{3.35}$$

where λ is the wavelength of the light and w_0 is the "waist", the $1/e$-radius of the optical field in the focus of the beam. The waist is related to the resonator geometry through Eq. (3.6). If we assume reasonable values for the various parameters ($\lambda = 532$ nm, $R = 1$ m and $L \approx 1$ cm), we find that $\alpha_0 \approx 1.5 \times 10^{-3}$. A requirement for paraxiality that is sometimes used (see, for example, p. 630 of ref. [7]) is $\alpha < 30^\circ = \pi/6$. As the opening angle of a Hermite-Gaussian beam scales with the square root of the transverse mode index, the highest-order transverse mode allowed within the paraxial approximation would have an index of the order 1.2×10^5.

A final limitation on a high-resolution interferometer, one that is shared between both conventional and degenerate resonator types, is the line width of individual resonances. At a certain point it is not feasible to reduce resonator losses further to reduce the line width of a resonator. Therefore, a resolution that is many orders of magnitude smaller than this minimum line width cannot be reached. However, using present day technology, a finesse $\mathscr{F}$ as high as 10^5 or 10^6 is possible [17], allowing, in principle, an inter-resonance spacing as small as $\lambda/10^6 = 0.5$ pm.

3.7 Conclusions

We have seen in this chapter that consideration of both wave and ray properties of optical resonators in combination can help improve the understanding of both. There exist close ties between the structure of the eigenfrequency spectrum of a resonator, and the behaviour of rays in that resonator. As a result, a convenient way of calculating, for example, the Gouy phase of a particular resonator geometry, is via the round trip *ABCD*-matrix of ray optics. Furthermore, when the Gouy phase of a resonator $\theta = 2\pi K/N$, that resonator has at the same time a highly degenerate eigenfrequency spectrum, and supports periodic orbits.

At least some of these periodic orbits survive outside the paraxial limit, but, where in the paraxial limits all periodic orbits for a given K/N occur at the same resonator length $L_{K/N,\text{parax}}$, nonparaxial periodic K/N-orbits are only possible at resonator lengths that depend strongly on the exact shape of the orbit. From the behaviour of these periodic orbits outside the paraxial limit, we may conclude that the round trip Gouy phase for nonparaxial eigenmodes will be larger than the paraxial Gouy phase. To get exact values, a full calculation of nonparaxial eigenmodes has to be performed.

A folded three-mirror optical resonator has properties that resemble those of a two-mirror resonator. A crucial difference is that eigenmodes are astigmatic, so that now two Gouy phases θ_T and θ_S are needed to fully describe both the structure of the eigenfrequency spectrum and general ray behaviour inside such a resonator. Degenerate eigenfrequency spectra and periodic orbits are still possible, but now with the stricter requirement that both θ_T and θ_S are rational fractions of 2π.

Finally, we saw that a degenerate two-mirror resonator may be used as a high-resolution interferometer for length-sensing purposes, where the benefit over a more conventional standing wave interferometer lies in the extended working range.

Chapter 4

Attempts towards a cavity random laser

This chapter contains a selection of experiments done on two-mirror (plano-concave) Nd:YVO$_4$*-lasers, similar to the setup used in chapter 2. These experiments were performed in our search for a* cavity random laser*, i.e., a random laser not based upon scattering by a disordered medium, but on the manifold of oscillating and (potentially) interacting modes of a highly multi-mode laser based upon a conventional cavity. The motivation for this search is that such a cavity random laser would allow a much larger degree of control over experimental parameters, as well as continuous instead of pulsed operation. This should greatly ease the comparison between theory and experiment.*

We will show that, unfortunately, our experiments did not reach the regime where random laser action could be expected. However, these efforts are not wasted: they draw attention to several key issues of multi-mode lasers. In this they may serve as a basis for future research.

4.1 Introduction

Ever since its invention in 1958 [18], the laser has captured the imagination of the general public as a source of monochromatic, confined beams of light, potentially with great brightness. This image is, of course, a simplification, ignoring as it does fundamental limitations such as quantum noise and diffraction, but nevertheless conventional lasers are fine examples of precision. As such, they are used in many high-accuracy measurement and control systems.

The directionality and monochromaticity of a laser's output is, to a very large extent, determined by the mirrors providing the feedback of light necessary for laser action. These mirrors form an optical resonator; it is this resonator that determines both the spatial and spectral properties of the resonator modes, leading to narrow-bandwidth directional emission.

However, as early as the 1960s, people started considering lasers that did away with conventional resonators, and instead relied on nonstandard ways of providing feedback of light, such as scattering of light in random media [19, 20]. Subsequently, the interest in these so called *random lasers* waned. However, the 1990s saw renewed interest in this type of laser systems, both from a theoretical [21, 22, 23, 24] and an experimental perspective [25, 26, 27, 28, 29, 30, 31, 32].

All experimentally realised random lasers so far consist of two important elements: a gain medium to provide amplification of light, and scattering particles to give feedback. These two elements may be separate, such as in a colloidal suspension of sub-wavelength TiO_2-particles in a laser dye solution [25, 26, 27], or combined in one, such as in finely ground ZnO- or GaN-powders [28, 29, 30]. From a theoretical point of view, a random laser is a laser based on chaotic modes [24]. These chaotic modes can be due to (microscopic) random scatterers, as in the above-mentioned implementations, or due to the (macroscopic) boundary conditions as in, for example, a stadium-shaped resonator [33].

Another possible classification of random lasers, largely orthogonal to the above-used distinction (microscopic versus macroscopic disorder), is based on the degree of *openness* of the random laser. Such a classification is well established [24, 34, 35], and is relevant because the degree of openness of a random laser leads to marked differences in behaviour. For "open" random lasers, the width of the resonances will be much larger than the average level spacing, so that many modes overlap. It is predicted that such random lasers have large Petermann K-factors [36]. On the other hand, in "closed" random lasers all resonances are well separated, with a width much smaller than the average spacing. These systems are expected to show effects of level repulsion [15, 37].

An important motivation for the revival of interest in these types of laser is that the properties of random lasers can be quite different from those of conventional laser systems. Theoretical calculations show that random lasers exhibit strikingly different spectral and temporal behaviour, such as, for example, increased laser line widths and laser intensity noise [36]. Experiments on scattering random lasers show that emission spectra can depend strongly on the emission direction, and that the output of such random lasers is not in a directed beam, but rather in all directions.

Interest in random lasers is not limited to the field of laser physics, but stretches from fundamental quantum physics to practical applications. From a fundamental point of view, random lasers may provide experimental access to quantum effects in combination with multiple scattering, quantum chaos, enhanced backscattering and Anderson localisation. Practical interest is driven by the fact that random lasers based on scattering media are, by definition, far more tolerant of imperfections in the feedback mechanism than conventional lasers, and can potentially be much cheaper than regular lasers. This has already led to, for example, the “paint-on laser” [31], that, according to its inventors, may be used for such varied applications as anti-counterfeit security systems, high visibility marking, emergency lighting and display technology.

As mentioned above, all current experimental realisations of random lasers contain a random, scattering medium. It is ironic that this “randomness”, while making the dependence of a laser on its surroundings far less critical and thereby making possible many practical applications, hampers a close comparison between theoretical predictions and experimental results. Control of the exact configuration of scatterers in random lasers based on ZnO- or GaN-powders or dye-TiO_2-suspensions is very limited, so that it is not always possible to make theory and experiment meet. Furthermore, dye-TiO_2-suspensions have to be constantly agitated to prevent sedimentation of the TiO_2 scatterers [32], so that reproduction of the configuration of scatterers is not possible. Another complication is that most theoretical treatments of random lasers deal with steady-state properties; in contrast, all experiments on scattering random lasers are pulsed to minimise the effect of heating and other complications.

For these reasons, it is desirable to have a random laser system that allows greater control over relevant experimental parameters, and that can be operated continuously. These requirements all but exclude random lasers based on scattering media. Furthermore, if this random laser can be built using off-the-shelf optical components this will greatly ease construction and exploration of diverse random laser systems.

At this point, it is useful to point out that the name “random laser” was, perhaps, an unfortunate choice, as it implies that some form of random element is *essential* to obtain a random laser. Rather, a random element is but one possible way of realising the truly essential element in a random laser, an ensemble of chaotic modes. Whether these modes are due to scattering particles or due to the shape of the boundary of the cavity is immaterial. It thus seems perfectly possible to create a random laser with no random element whatsoever.

For the reasons mentioned above, we undertook to construct a *cavity random laser*, a random laser based on a multi-mode optical resonator. This type of random laser was already considered in the 1960s, but the poor quality of the then-available gain media and other components led to inconclusive results. The central idea is to construct an optical resonator that will support many transverse modes that are not frequency-degenerate. These modes must experience comparable losses to prevent any loss-based mode selection mechanisms that would reduce the number of active laser modes, and they must somehow interact [20].

This mode interaction can take on many forms, depending on the type of random laser. For example, in an “open” random laser, losses due to outcoupling lead to spectral and spatial overlap of individual modes, and thus to mode mixing; in a “closed” random laser (i.e., negligible outcoupling), one employs the nonintegrability of the wave equation, including boundary conditions, to create a repulsive interaction of the modes (“level repulsion”). In essence, both these forms of interaction are due to the geometry of the system. In addition to these interactions, which apply equally to passive and active systems, in random lasers one may also have nonlinear mode-mode interaction mediated by the gain medium.

As explained in chapter 3, passive two-mirror resonators of certain geometries have

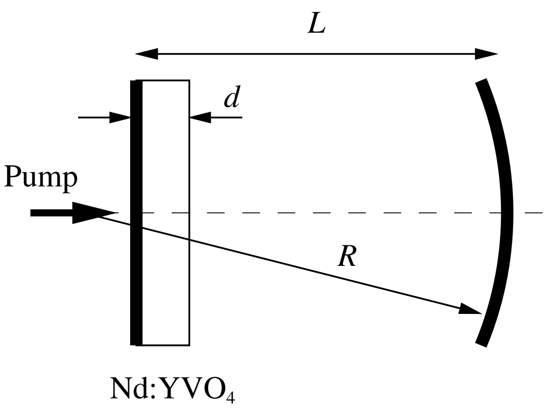

Figure 4.1: *Schematic resonator configuration, where L is the length of the resonator, d the thickness of the Nd:YVO$_4$-crystal, and R is the radius of curvature of the concave mirror. This setup is largely identical to that used in chapter 2 for the experiments on geometric modes.*

highly degenerate eigenfrequency spectra. If one then slightly changes, for example, the length of the resonator away from this degenerate configuration, the frequency degeneracy will be lifted. The frequency difference between neighbouring modes can be tuned by controlling the change in length away from a degenerate configuration. Hence, these near-frequency-degenerate resonator configurations were our prime choice for constructing a cavity random laser.

As a gain medium we chose Nd^{3+}:YVO$_4$, because it allows a high optical gain in a short crystal length, and because techniques, equipment and experience in working with Nd:YVO$_4$ were already present in our group. As Nd:YVO$_4$-crystals can be coated with highly reflective multilayer dielectric mirrors, we opted for a plano-concave resonator design, where one mirror is formed by the back facet of the Nd:YVO$_4$-crystal, and the other mirror is a separate concave mirror, see Fig. 4.1.

It is not *a priori* clear in which of the two classes mentioned above (“open” or “closed”) these lasers will fall. For instance, the cavity shown in Fig. 4.1 is generically open, but effectively closed for “low-loss” laser modes. Therefore it is not clear what form the (potential) interactions between modes will take (e.g., due to the geometry of the system or due to the gain). A further complication is that even high-quality mirror coatings are not completely uniform. These nonuniformities scatter light, and can therefore contribute to the interaction of modes.

As a consequence we employ an empirical approach and look for behaviour that is out of the ordinary, i.e., different from that of normal, nonrandom lasers. We primarily measured three basic properties: spectrum, laser output power and spatial profile. We analysed the optical spectrum using a Fabry-Pérot interferometer, and we also observed beat spectra using a fast optical detector and an FFT analyser. Laser output power was measured by either recording the output power as a function of pump power at fixed resonator geometry, or by recording the output power as a function of resonator length at fixed pump power. Spatial measurements consisted of near and far-field transverse beam profiles recorded using a CCD camera. As many of these measurements could be performed virtually simultaneously, it allowed powerful integrated diagnostics that can give deeper insight in the system.

In the next section we will describe our experimental setup in more detail. Then, in sections 4.3–4.5 we will report some surprising experimental results of spectral, output power and spatial measurements. Finally, we will wrap this chapter up with a concluding discussion. Even though, as we will see, a cavity random laser eluded us, in our experiments we encountered many unexpected phenomena. These effects, while not explored further in the context of this thesis, suggest rich physics and warrant further study. This, then, is the prime motivation for this chapter, to document and conserve the observation of these multi-mode laser phenomena and our associated thoughts.

4.2 Experimental setup

The setup used in these experiments is as sketched in Fig. 4.1. A plane-parallel Nd:YVO$_4$-chip, with a thickness d of either 0.21 mm or 1.0 mm, serves as a gain medium. This crystal is pumped optically by a titanium sapphire laser ($P_{\text{pump,max}} \approx 380$ mW) tuned to the absorption maximum of Nd:YVO$_4$ (pump wavelength $\lambda_{\text{pump}} = 809$ nm). The outward facing side of the crystal serves as a planar mirror; it has a multilayer dielectric coating with a reflectivity higher than 99.8% at the laser wavelength of $\lambda = 1064$ nm, while being antireflective at the pump wavelength. The inward facing side of the crystal has an antireflective coating at the laser wavelength.

The second resonator mirror serves as outcoupling mirror; it is a concave spherical mirror, either with a reflectivity of 95% and a radius of curvature $R = 25$ mm, or with a reflectivity of 98% and a radius of curvature $R = 2.1$ mm. This last mirror has only been used in combination with the 0.21 mm thick crystal. The outcoupling mirror is mounted on a movable stage for coarse control of the resonator length, and on a piezo crystal for fine length control.

In contrast with the experiments in chapter 2, pumping is mostly done on-axis to reduce the amount of pump-related mode selection. The $1/\mathrm{e}^2$ intensity radius of the pump spot in the crystal is in the range 50–350 μm. This size of the pump spot must be compared to the waist w_0 of the fundamental mode of the resonator; this waist is located at the planar mirror. The value of w_0 depends on the radius of curvature of the concave mirror, as well as on the cavity length. From Eq. (3.4) we see that, for a plano-concave cavity, the maximum mode waist as a function of cavity length occurs for hemiconfocal cavity configurations, where $L = R/2$. For the 25 mm radius-of-curvature outcoupling mirror we then find $w_0 \sim 65$ μm, while for the 2.1 mm radius-of-curvature outcoupling mirror $w_0 \sim 19$ μm. For cavity configurations other than hemiconfocal, the mode waist is smaller than these maximum values. For example, for a resonator with $L = 0.9\,R$, the mode waist w_0 is ~ 50 μm and ~ 14.6 μm for the two mirrors, respectively. According to Eq. (3.4), the mode waist tends to zero for a hemiconcentric resonator with $L = R$; note, however, that Eq. (3.4) is a *paraxial* result, while a hemiconcentric resonator violates the paraxial approximation. In practice, therefore, w_0 will remain finite. In our experiments the size of the pump spot is always comparable to or larger than the size of the mode waist w_0. This reduces (but does not eliminate) mode selection effects based on differences in spatial overlap between the pump spot and different transverse laser modes.

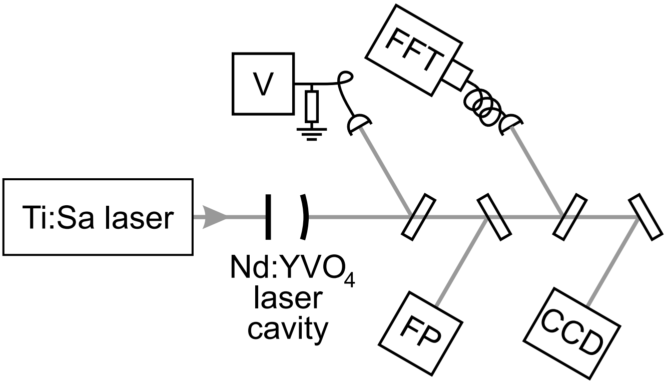

Figure 4.2: *Schematic picture of the various ways in which the laser output could be analysed.* V *indicates a volt meter attached to a semiconductor photodiode via a load resistor,* FFT *indicates an FFT analyser attached to a fibre-coupled fast photodiode,* FP *indicates a scanning plane-parallel Fabry-Pérot interferometer, and* CCD *indicates a CCD camera.*

Figure 4.2 gives a schematic picture of the diagnostics. Behind the laser, a dichroic mirror filters out any remaining pump light, after which the laser output can be directed onto either a semiconductor photodiode to measure the laser output power, onto a scanning plane-parallel Fabry-Pérot interferometer to determine the optical spectrum, onto a fast fibre-coupled photodiode to inspect beat spectra using an FFT analyser, or imaged onto a CCD camera.

Because the Nd:YVO$_4$-crystal has a refractive index $n_e \approx 2.17$, the optical length of the laser cavity will be different from the physical separation between the two mirrors. To relate frequency differences between modes to the length of the laser cavity we introduce the *optical* resonator length

$$L_{\text{opt}} = L + (n_e - 1)d, \tag{4.1}$$

where d is the thickness of the Nd:YVO$_4$-crystal. The longitudinal mode spacing or free spectral range of our resonator is then given by

$$\Delta\nu_{\text{L}} = \frac{c}{2L_{\text{opt}}}. \tag{4.2}$$

To get a sense of scale, for a hemiconcentric cavity configuration we find that $\Delta\nu_{\text{L}} \approx 5.6$ GHz when using a $R = 25$ mm-mirror and a 1 mm thick crystal, and $\Delta\nu_{\text{L}} \approx 61$ GHz when using a $R = 2.1$ mm-mirror and a 0.21 mm thick Nd:YVO$_4$-crystal.

From section 3.2.1 we see that the *ratio* between transverse mode spacing and longitudinal mode spacing is directly related to the Gouy phase θ,

$$2\pi\frac{\Delta\nu_{\text{T}}}{\Delta\nu_{\text{L}}} = \theta = 2\arccos\left(\pm\sqrt{g_1 g_2}\right), \tag{4.3}$$

with g_1 and g_2 the cavity g-parameters (also see chapter 3), taking into account the presence of the crystal. In this equation, the $+$ sign applies to $g_1, g_2 > 0$ and the $-$ sign to $g_1, g_2 < 0$.

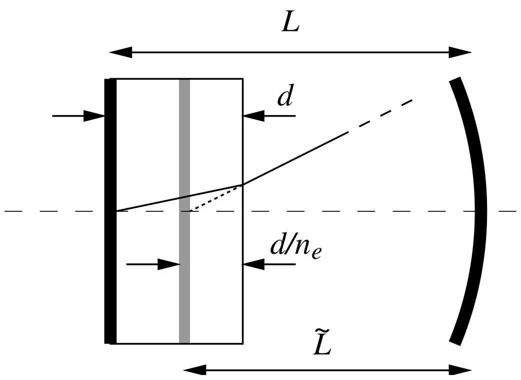

Figure 4.3: *Schematic indication of the relation between the nominal resonator length L and the corrected resonator length* $\tilde{L}$ *which takes into account refraction at the air-crystal interface.*

For a plano-concave resonator we find that [7]

$$g_1 = 1 \text{ and } g_2 = 1 - \frac{\tilde{L}}{R}, \tag{4.4}$$

where $\tilde{L}$ is the geometric length of the resonator corrected for refraction effects in the crystal,

$$\tilde{L} = L - (1 - 1/n_e)d\,. \tag{4.5}$$

In Fig. 4.3 we indicate, for a hemiconfocal resonator, the significance of this corrected length $\tilde{L}$. Because of refraction at the air-crystal interface, the apparent depth in the crystal at which the flat mirror lies equals d/n_e instead of d. In essence, $\tilde{L}$ is the length of the *empty* resonator that is equivalent to our laser cavity.

By combining Eqs. (4.1) and (4.5) and eliminating L, we can relate the corrected geometric resonator length to the optical resonator length through

$$\tilde{L} = L_{\text{opt}} - (n_e - 1/n_e)d\,. \tag{4.6}$$

Resonator configurations may now be compared by their reduced length

$$\ell = \frac{\tilde{L}}{R}, \tag{4.7}$$

where $\ell = 1/2$ and $\ell = 1$ correspond to a hemiconfocal and hemiconcentric cavity, respectively. Summarising, using Eqs. (4.2), (4.3) and (4.4) with Eq. (3.10) we find that the eigenfrequencies for our cavity are given by

$$\begin{aligned} \nu_{q,mn} &= \Delta\nu_{\text{L}} \left\{ q + (m+n+1)\frac{\theta}{2\pi} \right\} \\ &= \frac{c}{2L_{\text{opt}}} \left\{ q + (m+n+1)\frac{\arccos\sqrt{1-\tilde{L}/R}}{\pi} \right\}. \end{aligned} \tag{4.8}$$

4.3 Spectral measurements

As mentioned in the introduction, one possibility to construct a cavity random laser is to build a resonator that supports many transverse modes that are not frequency-degenerate, but are nevertheless spaced sufficiently close that they overlap spectrally. In order to search for such resonator configurations, we measure both the optical spectrum of our laser, using a Fabry-Pérot interferometer, and its beat spectrum, using a fast optical detector in conjunction with an FFT analyser.

4.3.1 Optical spectra

The length of the plane-parallel scanning Fabry-Pérot interferometer that we use for spectral diagnostics can be varied between 2.68 mm and 22.7 mm; over this range we found a finesse of $\mathscr{F} \sim 125$. From these interferometer lengths we deduce that the free spectral range of our interferometer can be varied between 6.60 GHz and 56.0 GHz, with a corresponding line width of 53 MHz and 0.45 GHz, respectively. Line widths below ~ 50 MHz were difficult to realise since we found that the finesse rapidly degrades for interferometer lengths beyond ~ 25 mm.

At low pump power, just above laser threshold, it is possible to obtain single frequency output at all resonator configurations except extremely close to hemiconcentric, and nothing remarkable is observed. If we change the length of the laser cavity on a sub-wavelength scale, using the piezo transducer, the frequency of this single lasing mode will change. As the spectral position of the gain profile is fixed, this will change the modal gain, until a second mode has the same gain as the original lasing mode. Then, we observe a changeover between these two modes, where the first mode stops lasing and the second mode becomes the new lasing mode. In general, we found that this changeover will be between modes of the same transverse order, but differing by 1 in the longitudinal mode index. In Fig. 4.4a we see the Fabry-Pérot (FP) spectrum of a single mode, while Fig. 4.4b shows such a changeover between two modes upon tuning the cavity length.

At higher pump powers, more and more transverse modes come above threshold, so that the FP spectrum shows more and more peaks. As explained in section 3.2.1, the distance between neighbouring transverse modes is directly related to the resonator geometry. Because FP spectra are periodic with a period equal to the free spectral range of the interferometer, all peaks are folded back into a single free spectral range, quickly making the interpretation of such spectra extremely complicated. At generic cavity lengths, these spectra show no further special features.

The situation is different around degenerate resonator configurations, where the ratio of transverse mode spacing and longitudinal mode spacing is rational,

$$\frac{\Delta\nu_{\mathrm{T}}}{\Delta\nu_{\mathrm{L}}} = \frac{K}{N} \tag{4.9}$$

as described in section 3.3. In Figs. 4.5a–e we show five FP spectra of a laser with an $R = 2.1$ mm radius-of-curvature outcoupling mirror, taken around the resonator configuration $\ell = 3/4$. For this configuration we calculate that $\Delta\nu_{\mathrm{L}} = 77.6$ GHz.

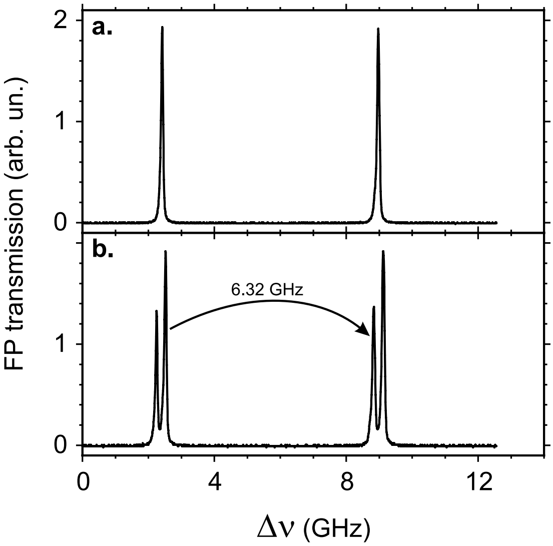

Figure 4.4: *Typical Fabry-Pérot spectra for a laser operated just above threshold. The location of the zero of the horizontal axis is arbitrary. Please note that we display more than a single free spectral range, highlighting the periodic nature inherent to Fabry-Pérot spectra. Therefore, the same frequency is, in this case, displayed twice. (a) For arbitrary microscopic resonator length only a single mode lases. (b) At specific microscopic resonator lengths two modes have the same modal gain, leading to a changeover between lasing modes. Indicated is the unfolded spectral distance between the two modes,* $\Delta\nu \approx 6.32$ GHz*. As both these modes are* TEM_{00} *modes, differing by 1 in longitudinal mode index, this spectral distance corresponds to the free spectral range* $\Delta\nu_L$ *of the laser. From this we can deduce that the optical cavity length* $L_{opt} \sim 23.7$ mm*. As these experiments were done with a crystal of* 1.0 mm *thickness and a mirror with a radius of curvature* $R = 25$ mm*, the geometric cavity length is* $\tilde{L} = 22$ mm*, and the reduced cavity length* $\ell = 0.88$.

In Figs. 4.5a, b, d and e we observe a generally broad structure in the FP spectrum, with a typical width between 15 and 25 GHz (compared to a free spectral range $\Delta\nu_\mathrm{L} = 86$–70 GHz for figures a–e). Superimposed on this broad structure are narrower lines. If we tune the length of the laser cavity by changing the voltage on the piezo, these narrower lines shift, indicating that they correspond directly to resonator modes. In contrast, the broad structure itself is immobile upon changing the length of the resonator on a sub-wavelength scale, suggesting that the spectral position of this broad structure is linked to the position of the maximum of the gain profile of the Nd:YVO$_4$-crystal. This is confirmed by changing the temperature of the Nd:YVO$_4$-crystal, causing a shift of the position of maximum gain. We then observe that the broad structure changes frequency, while the superimposed narrower lines remain fixed.

The FP spectrum displayed in Fig. 4.5c is quite different. The broad “bulge” that is present for different lengths collapses into a much narrower structure, with a width of around

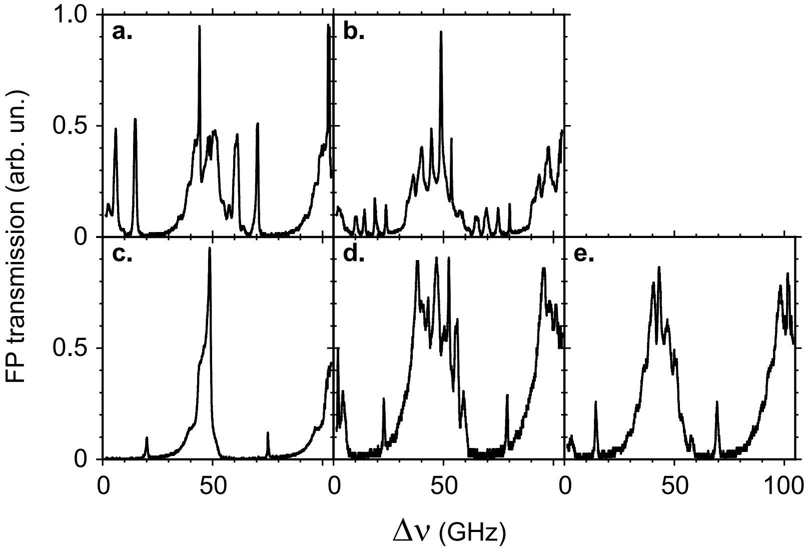

Figure 4.5: *Fabry-Pérot spectra for a resonator with a mirror with a radius of curvature* $R = 2.1$ mm, *and a reduced cavity length of (a)* $\ell = 0.66$, *(b)* $\ell = 0.71$, *(c)* $\ell = 0.75$, *(d)* $\ell = 0.80$, *and (e)* $\ell = 0.85$. *See Eq. (4.7) for the definition of* ℓ.

6 GHz. The position, and hence the frequency, of this structure changes when the length of the cavity is changed on a sub-wavelength scale, until at certain resonator lengths we observe a changeover between this structure and one of the smaller satellite peaks. This process is similar to the changeover between single modes that occurs at nondegenerate resonator lengths, as described above.

The collapse of the broad bulge into a much narrower spectral feature is not surprising once one realises that the present cavity configuration, $\ell = 0.75$, leads to a ratio of transverse and longitudinal mode spacings $\Delta\nu_T/\Delta\nu_L = 1/3$. Therefore, the entire eigenfrequency spectrum of the resonator is reduced to a “comb” of highly degenerate frequencies, as schematically depicted in Fig. 3.6. The distance between the large central structure and the smaller satellite peaks in Fig. 4.5c is equal to 26 GHz, which is indeed a third of the longitudinal mode spacing of the laser.

4.3.2 Beat spectra

Because of the modest finesse of our Fabry-Pérot resonator, it is not possible to resolve the finer structure in the broad spectra reported above. To gain more insight we measured the laser output in the time domain, and Fourier-transformed this signal back to the frequency domain. We directed the laser output onto a fibre-coupled fast photoreceiver, with a specified bandwidth of 6 GHz. The resulting signal was analysed using a FFT spectrum analyser.

In Fig. 4.6a we plot an FP spectrum for a laser at the edge of stability, $\ell = 0.999$. We see again a broad structure, with some narrower oscillations superimposed. The width of

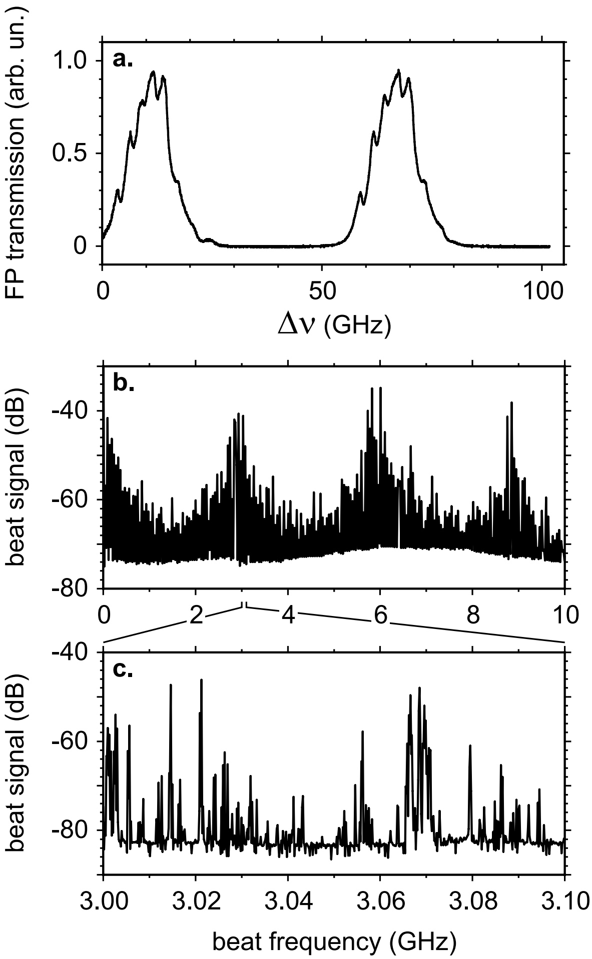

Figure 4.6: *(a) Fabry-Pérot spectrum of the output of a laser operated close to the edge of stability,* $\ell = 0.999$*. (b) Beat spectrum of the same output. Please note that the vertical scale is logarithmic. (c) Expanded section of the beat spectrum of (b). The concave cavity mirror had a radius of curvature* $R = 25$ mm*, while the crystal had a thickness of* $d = 0.21$ mm*. From this we calculate that* $\Delta\nu_{\rm L} \approx 5.9$ GHz*.*

the broad structure is of the order of 11 GHz, while the longitudinal mode spacing $\Delta\nu_{\rm L} \approx 5.9$ GHz. In Fig. 4.6b we plot the corresponding beat spectrum. A notable feature is the increased beat strength around multiples of about 2.9 GHz. This corresponds to the period of the oscillations superimposed on the broad structure in subfigure a. As we are very close to a hemiconcentric cavity configuration, where $\Delta\nu_{\rm T}/\Delta\nu_{\rm L} = 1/2$, we expect a transverse mode spacing of $\Delta\nu_{\rm L}/2 \approx 3.0$ GHz, in good agreement with the experimentally found value. In Fig. 4.6c we expand a 100 MHz-wide section of the full beat spectrum in Fig. b. We estimate that there are about 50–100 distinct beat frequencies in this interval, although most of these are very weak. Based on this, we estimate that there are about 10^4 beat frequencies in the beat spectrum between 0 and 10 GHz, i.e., in an interval comparable to the width of the broad structure (11 GHz).

To derive the number of lasing modes from the number of beat frequencies, we must make an assumption about the spectral distances between those lasing modes. One extreme assumption is that all lasing modes are equidistant, as is predicted by Eq. (3.10) for transverse modes belonging to the same longitudinal mode index q. In that case, a great number of mode-mode distances will be degenerate. A number of 10^4 *distinct* beat frequencies would then imply the presence of about 10^4 (transverse) lasing modes. However, as the distance between neighbouring transverse modes is ~ 3 GHz, the assumption that all transverse modes belong to the same longitudinal mode index q is very unrealistic (given the width of the broad structure and the transverse mode spacing, every longitudinal mode index q contributes, at most $11/3 \approx 4$ transverse modes). The other extreme assumption, also not very realistic, is that all mode-mode distances are effectively different. Then, the upper bound on the total number of lasing modes is reduced to about 10^2. So, our (very rough) guess is that $\sim 10^3$ modes are involved.

For comparison, a *passive* cavity consisting of two mirrors with the same reflectivity as our concave and our flat mirror (95% and 99.8%, respectively) would have a finesse of about 100. Therefore, it would not be possible to distinguish between more than about 100 modes per free spectral range, or about $11/5.9 \times 100 \approx 200$ modes in a frequency interval of 11 GHz. In the *active* system the line width is not a limiting factor, as all beat frequencies in Fig. 4.6c are well-resolved.

Spectral beat diagnostics also allows us to observe relatively low-frequency beats (up to 100 MHz) around frequency-degenerate laser cavity configurations. In Fig. 4.7 we plot the spectral position of three different beat peaks as a function of the length of the cavity around $\ell = 3/4$, where $\Delta\nu_{\mathrm{T}}/\Delta\nu_{\mathrm{L}} = 1/3$ (please note that the correspondence between the number of beat peaks and the degree of degeneracy is pure coincidence). In these experiments we used a cavity end mirror with a radius of curvature of 25 mm. We see that, at certain cavity lengths, the beat frequencies go to zero, indicating a frequency degeneracy between lasing modes. The nature of these frequency degeneracies is discussed in the following.

From chapter 3 we know that for a frequency-degenerate cavity, where $\Delta\nu_{\mathrm{T}}/\Delta\nu_{\mathrm{L}} = K/N$, lowering the longitudinal mode index q by K while at the same time raising the total transverse mode index t by N will leave the frequency unchanged (where $t = m+n$). Hence, as here $K/N = 1/3$, the beat peaks plotted in Fig. 4.7 must correspond to the frequency difference between modes $\{q,t\}$ and $\{q-k,\, t+3k\}$,

$$\Delta\nu_k = \nu_{q,\,t} - \nu_{q-k,\,t+3k} \tag{4.10}$$

with k an integer.

To calculate the rate at which the position of the beat peak changes as the resonator length is changed, we take the derivative of Eq. (4.10) with respect to the resonator length L, using Eqs. (3.8) and (3.10). If we then substitute the values of our cavity configuration, we find that for $k = 1$ the slope expected in Fig. 4.7 equals 3.16×10^2 MHz/mm, in good agreement with the value found experimentally, 3.14×10^2 MHz/mm.

It is surprising that the three beats as displayed in Fig. 4.7 do not reach zero frequency at the same laser cavity length. This effect cannot be explained within the context of the theor-

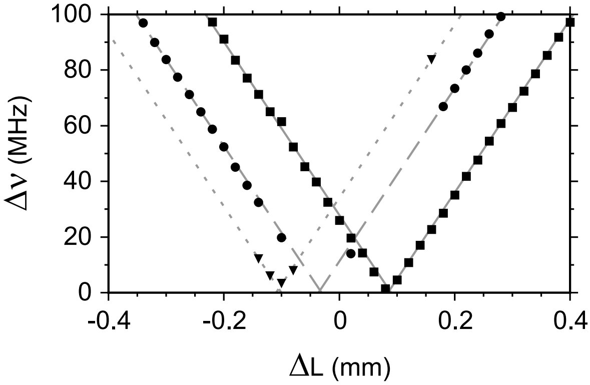

Figure 4.7: *Spectral position of three different beat peaks plotted versus the change in resonator length. We have chosen* $\Delta L = 0$ *at the resonator length for which we estimate that* $\ell = 3/4$. *For reference, the width of the graph corresponds to a change in* ℓ *of* 0.032. *The solid and dashed grey curves are straight line fits, with a slope of* 3.14×10^2 MHz/mm. *The dotted grey curve, with the same slope, is drawn as a guide to the eye.*

etical framework of chapter 3, as that would predict a unique degenerate cavity configuration where $K/N = 1/3$. A possible explanation for the differing degenerate resonator lengths may be dispersive effects due to gain guiding caused by the nonuniform transverse pump profile in the Nd:YVO$_4$-chip. As the gain profile is localised, it has a dispersive effect on modes that depends on the transverse profile of the latter. Neglecting dependencies on the longitudinal mode index q, we can, for $K/N = 1/3$, distinguish three groups of modes: one group will consist of all modes with total transverse mode index $t = 3k$, the second group will contain all modes $t = 3k + 1$, while the third group contains all modes with $t = 3k + 2$. As a result, the transverse profile of (linear combinations of) these modes differs. In combination with the above-mentioned dispersive effects of gain guiding this may lead to the observed shifts in degenerate resonator configurations.

In these experiments we had hoped to observe, as evidence that we were on the way to creating a random laser, avoided mode crossings around degenerate cavity configurations. These avoided crossings would demonstrate the presence of mode mixing, and would show up as beat frequencies that, as a function of cavity length, do *not* go down to zero, but only to a finite frequency, before increasing again. Such avoided crossings are, in general, the precursors of fully developed level repulsion as occurs in wave-chaotic systems [15]. As we see no trace of avoided mode crossings, we must conclude that, in this experiment, mode mixing can be neglected.

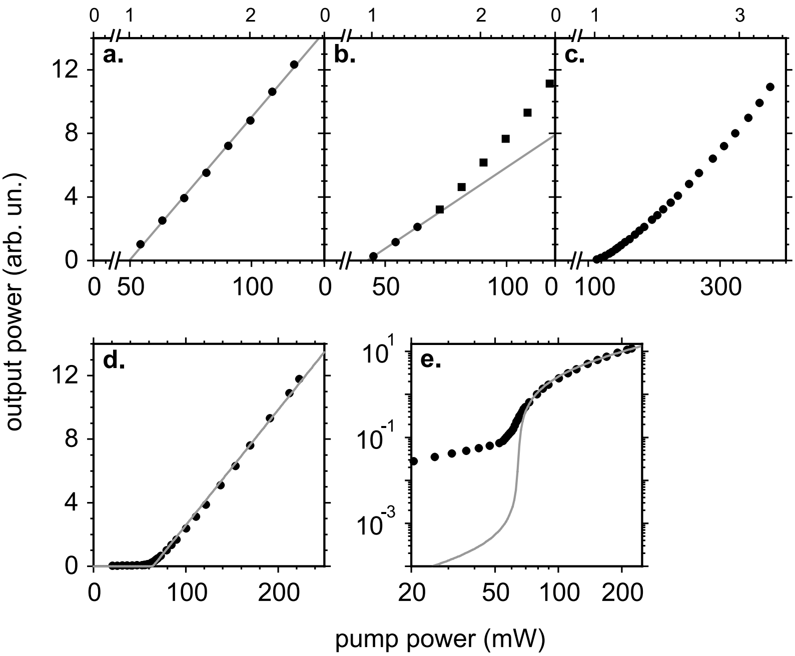

Figure 4.8: *Laser output power versus pump power for various cavity configurations. (a)–(c) Laser cavity with a concave mirror with* $R = 25$ mm *and (a)* $\ell = 0.88$, *single mode, (b)* $\ell = 0.98$, *single mode (circles) and dual mode (squares), (c)* $\ell = 0.99$ *and* $1.7\times$ *larger pump spot, multi-mode. The estimated pump spot radii are* ~ 53 μm *and* ~ 90 μm, *respectively. (d) and (e) Laser cavity with a concave mirror with* $R = 2.1$ mm *and (d)* $\ell = 0.99$, *multi mode, linear axes, (e) same as (d), but logarithmic axes. The grey curves in (a) and (b) are linear fits to the single mode regime. The grey curves in (d) and (e) are fits of Eq. (4.11), as explained in the text. The numbers above the top axis in (a)–(c) indicate the dimensionless pump parameter* $M = P_{pump}/P_{pump,th}$.

4.4 Output power measurements

4.4.1 Input-output curves

We have measured, for a given cavity geometry, the output power of our laser as a function of input power (or pump power). From this so called LI-curve we can then obtain information on, among other things, the position and sharpness of the laser threshold.

In Fig. 4.8 we plot LI-curves for four different cavity configurations. Figures 4.8a–c were taken for a cavity with a $R = 25$ mm end mirror, while Figs. 4.8d and e correspond to a cavity with a $R = 2.1$ mm end mirror.

Figure 4.8a is a typical example of an LI-curve for a generic cavity configuration ($\ell = 0.88$), with a relatively small pump spot (estimated pump spot radius $r \sim 53$ μm). Above laser threshold, at a pump power of ~ 50 mW, the laser output power rises linearly with the pump power. This is the expected behaviour for single mode lasers (in fact, this is the same cavity configuration that led to the FP spectrum of Fig. 4.4).

For a cavity that is closer to hemiconcentric, we observe LI-curves such as depicted in Fig. 4.8b ($\ell = 0.98$). Above threshold, the laser output power at first rises linearly with the pump power. Then, a second kink occurs, after which the output power again increases linearly. Inspection of the optical spectrum with a Fabry-Pérot interferometer shows that above threshold, but below the second kink, the laser operates in a single mode. Above the second kink, the laser operates in two modes.

The reason for the occurrence of this second kink in Fig. 4.8b, but not Fig. 4.8a, lies in the laser mode size for the two cases. From Eq. (3.4) we see that the size of the laser mode in the Nd:YVO$_4$-chip is smaller for $\ell = 0.98$ than for $\ell = 0.88$. This means that, for equal pump spot size, the gain difference between the fundamental laser mode and higher order transverse modes is reduced, so that, in Fig. 4.8b, we *do* bring the first higher order transverse mode above threshold. This leads to an increase in output power compared to the single-mode regime.

For a cavity that is even closer to hemiconcentric ($\ell = 0.99$), and for a pump spot that has a 1.7× larger radius ($r \sim 90\ \mu$m), we get LI-curves such as in Fig. 4.8c. Here, we observe a somewhat smoothened laser threshold: the thresholds of the higher order modes are so close together that, in this measurement, they can no longer be discerned individually, giving rise to a smooth superlinear dependence of output power on pump power.

Finally we consider a resonator with (almost) the same geometry ($\ell = 0.99$), but now with an outcoupling mirror with a radius of curvature of $R = 2.1$ mm. Then, the pump spot size is much larger than the fundamental mode size ($r \sim 0.27$ mm, while for a cavity with $\ell = 0.99$ and a mirror with a radius of curvature of $R = 2.1$ mm the waist of the fundamental laser mode $w_0 \sim 8\ \mu$m). For this laser we obtain an LI-curve as in Fig. 4.8d and e (where Fig. e is plotted on logarithmic axes). This curve looks like that of a single-mode laser; Fig. 4.8e resembles in fact the single-mode “S”-curve shape as can be found in any laser physics textbook (see, for example, Fig. 13.10 of Siegman [7]). From the optical spectrum, however, we see that the laser operates in many modes (not shown). This suggests that a large number of modes have their threshold close together.

For a single-mode laser such an “S”-curve is described by the equation

$$n = \frac{p}{2}\left\{(M-1) + \sqrt{(M-1)^2 + 4M/p}\right\}, \tag{4.11}$$

where n is the cavity photon number and $M = P_{\text{pump}}/P_{\text{pump,th}}$ is the dimensionless pump parameter. The parameter p is the number of (cavity) modes in which spontaneous emission can take place. The value of p determines the “sharpness” of the threshold: the width of the threshold region is $\sim p^{-1/2}$. Note that p is inversely related to the so-called spontaneous emission factor β [38],

$$p^{-1} = \beta = \frac{\Delta\Omega_{\text{cav}}}{8\pi}\left(\frac{4}{1-\mathscr{R}}\right)\frac{\Delta\nu_{\text{cav}}}{\Delta\nu_{\text{cav}} + \Delta\nu_{\text{gain}}} \tag{4.12}$$

where $\Delta\Omega_{\text{cav}} = \lambda^2/\pi w_0^2$ is the solid angle subtended by the (fundamental) cavity mode, $\mathscr{R} = \mathscr{R}_1\mathscr{R}_2$ is the product of the reflectivities $\mathscr{R}_1$ and $\mathscr{R}_2$ of the cavity mirrors, $\Delta\nu_{\text{cav}} = \Delta\nu_{\text{L}}/\mathscr{F}$ is the cold-cavity line width and $\Delta\nu_{\text{gain}}$ is the gain bandwidth. For this cavity configuration we find $\Delta\Omega_{\mathrm{cav}} = 5.36 \times 10^{-3}$ sr, while from the mirror reflectivities we calculate $\mathscr{R} = 0.978$. Using the free spectral range and the cavity finesse we find $\Delta\nu_{\mathrm{cav}} = 61.5/283 = 0.217$ GHz, while for Nd:YVO$_4$ $\Delta\nu_{\mathrm{gain}} = 257$ GHz. Substituting these numbers in Eq. (4.12) we calculate $p = \beta^{-1} \sim 3.0 \times 10^4$.

It may seem strange that we discuss Eqs. (4.11) and (4.12) in the context of Figs. 4.8d and e: the equations relate to a *single* laser mode, while the results in Figs. 4.8d and e are for a *multi*-mode laser. However, even though these expressions do not apply to the present case, they may still serve to guide our thoughts. The grey curves in Figs. 4.8d and e are fits of Eq. (4.11) to the experimental data, where we have used the value of $p = 3.0 \times 10^4$ calculated above. In these fits the only fitting parameters are the threshold pump power $P_{\mathrm{pump,th}}$ (relating absolute pump power to the dimensionless pump parameter M) and the relation between the output power (given in arbitrary units) and the cavity photon number. We see that, while above threshold the correspondence is quite reasonable, below threshold the fit is, unsurprisingly, very poor. In particular, the sharpness of the threshold in the experiment is far less than predicted for a single-mode laser.

Summarising, from the input-output curves in Figs. 4.8a–c we must conclude that, using a mirror with a radius of curvature of $R = 25$ mm, it was not possible to have a large number of lasing modes with approximately equal threshold. Only for when using a mirror with a radius of curvature of $R = 2.1$ mm, as in Figs. 4.8d and e, could this condition be reached experimentally.

4.4.2 Output power at fixed pump

Another way in which the output power of a laser may be measured is to keep the pump power fixed, and to vary the loss or gain of the different cavity modes. The gain directly depends on the spatial overlap between the pump spot and the cavity modes. It can be changed by, for example, displacing the pump spot away from the optical axis, or by altering the length of the cavity, thereby changing the size of the laser modes at the Nd:YVO$_4$-crystal. The losses can also be changed by altering the length of the cavity, through the ratio of mode spot size on the mirrors and the transverse extent of those mirrors. These changes in gain or loss will show up as variations in the output power of the laser.

In Figs. 2.6 and 2.8 we already saw examples of the influence of spatial overlap between pump and laser modes. There we plotted the total laser output power versus the length of the cavity, for fixed pump power. As the pump spot was located away from the optical axis, the laser output increased dramatically at degenerate cavity configurations, where a linear combination of cavity modes had a much higher spatial overlap with the pump spot than the individual cavity modes. Similar effects, but much weaker, can be seen with on-axis pumping, when the size of the pump spot differs from the size of the fundamental laser mode. There, too, linear combinations of modes can be much closer to the size and shape of the pump spot than the cavity modes individually. Such linear combinations are only possible between modes of the same frequency, and hence they will only occur at frequency-degenerate cavity configurations.

The influence of pumping off-axis is illustrated by Fig. 4.9. We measured the total output power at constant pump power and cavity length, versus the transverse displacement of the pump spot on the Nd:YVO$_4$-crystal. We clearly see two distinct shoulders on either side,

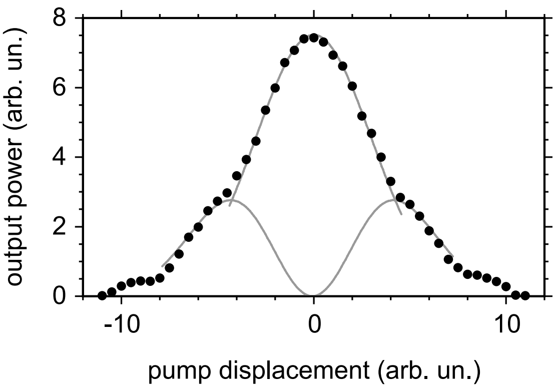

Figure 4.9: *Measured laser output power at constant pump power for a cavity with* $\ell = 0.90$*, versus the transverse displacement of the pump spot. Clearly visible are the two shoulders on either side of on-axis pumping. The grey curves are fits of the calculated overlap between a Gaussian pump spot, and a Hermite-Gaussian* TEM_{00} *and* TEM_{01} *cavity mode, respectively.*

caused by the changing overlap with the fundamental and first and second higher transverse modes. Also indicated are fits to the peak and to the first shoulders, respectively. The fit to the peak of the measured curve was done using the calculated overlap of two Gaussian modes, one for the laser mode and one for the pump profile. The fit to the first shoulders was done using the calculated overlap of a fundamental Gaussian mode (the pump profile) and a Hermite-Gauss TEM_{01} mode (the first higher transverse laser mode). The fundamental cavity mode waist size w_0 was taken equal in the two fits.

Interesting effects are also visible when we measure, with an on-axis pump, the laser output power at constant pump power versus cavity length, right at the very edge of stability of the cavity, as plotted in Fig. 4.10. These curves were obtained using a $R = 25$ mm end mirror. On the horizontal axes we plot, as a percentage, the change in reduced cavity length ℓ relative to the estimated hemiconcentric configuration (see the appendix in section 4.7). In Fig. 4.10a we see that the output power of the laser decreases rapidly when, upon increasing the cavity length, we get to within 0.1% of hemiconcentric. Upon further increase, surprisingly, the output power appears to level off, and decreases more slowly. Clearly visible are two local minima in the output power (indicated by arrows A and B). These points coincide with sudden changes in the shape of the mode inside the laser cavity; in the next section we will show near-field images of the mode on the outcoupling mirror around these local minima (albeit for a different outcoupling mirror).

In Fig. 4.10b we plot a similar measurement, but now with an intracavity pinhole placed right next to the Nd:$\mathrm{YVO_4}$-crystal; this pinhole was chosen such that it only allows, for a cavity shorter than hemiconcentric, the fundamental Gaussian mode to lase. We see that for $\Delta\ell < 0$, the laser output is reduced considerably compared to the case where no intracavity pinhole is present (Fig. 4.10a). However, to our surprise we found that for $\Delta\ell > 0.2\%$, the total laser output is *enhanced*, and laser action is possible up to much larger cavity lengths. Both measurements were found to be reproducible.

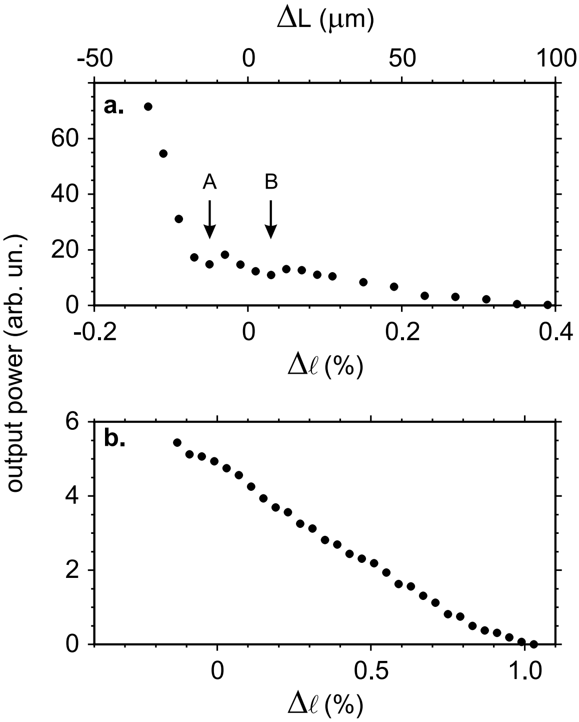

Figure 4.10: *(a) Measured laser output power at constant pump power versus cavity length, for a cavity with an* $R = 25$ mm *radius of curvature end mirror and a crystal with a thickness of* $d = 0.21$ mm. $\Delta\ell = 0$ *corresponds to the best estimate for hemiconcentric. The arrows indicate two local minima in the total output power. Indicated at the top of the graph is the absolute change in cavity length compared to hemiconcentric. (b) The same, but now with an intracavity pinhole that, below hemiconcentric, only allows the fundamental Gaussian mode to lase. The vertical scale for the two plots is different. The uncertainty in the position of* $\Delta L = 0$ *is about* $3\ \mu$m, *as explained in the appendix in section 4.7.*

We thus observe that both without and with intracavity pinhole, the laser operates even beyond the edge of resonator stability. Of course, lasing in unstable resonators is well known, but the transition between a stable and an unstable resonator has never been studied carefully. We observe here that in fact the transition is *not* very abrupt. Our results suggest that the geometrically abrupt transition between a stable and an unstable resonator is smoothed by diffraction. As, at the edge of stability, the size of the laser mode on the outcoupling mirror can become comparable to the transverse mirror size (see Eq. (3.5)), diffraction from the mirror boundary is expected to play a role; this interpretation is supported by experiments on microwave resonators [39]. Inserting the intracavity pinhole apparently enhances the diffraction effects even further.

4.5 Spatial measurements

As we already saw in chapter 2, the transverse output profile of our laser can strongly depend on the length of the laser cavity. There we saw that, for an off-axis pumped laser, the output is either in the form of a higher order transverse mode, or in the form of a so-called geometric mode when the cavity is highly frequency degenerate. When pumping the laser purely on-axis, these effects are less pronounced. Nevertheless, we found that when the size of the pump spot differs from the size of the fundamental laser mode, the mode profile in both the near and far field shows subtle changes when the length of the laser is scanned through such a degenerate configuration.

More pronounced is the behaviour of the output profile at the edge of the stability region of the cavity. In Fig. 4.11 we plot transverse emission profiles, taken on the concave cavity mirror, for different cavity lengths. If the cavity is well below our best estimate of hemiconfocal, we see that the near field on the mirror is a complex 2D pattern (Fig. 4.11a). If we increase the cavity length slightly, the near field on the mirror suddenly collapses into a single stripe, as in Fig. 4.11b. At the same time, the total laser output power has a local minimum, similar to the local minimum indicated as “A” in Fig. 4.10a. Then, going towards a hemiconcentric cavity, this stripe evolves smoothly into the two spots of Fig. 4.11c. This pattern on the concave mirror suggests emission in a “V”-shaped mode, with the cusp of the “V” on the flat mirror coinciding with the pump spot. What we see in Fig. 4.11c are the two vertices of the “V”.

If the length of the resonator is increased even more, a spot appears in the middle of the image, between the two spots of the “V”. Inspection of this central spot shows that it has a different polarisation than the “normal” laser output, i.e., horizontal instead of vertical. Also, the wavelength of this output light is slightly longer than “normal”, $\lambda \sim 1066$ nm instead of 1064 nm (where “normal” refers to stable cavity configurations). In Fig. 4.11d this central spot has become very prominent, and the “V”-mode has almost disappeared. This changeover from “V”-shaped lasing to a single central spot occurs at the same cavity length where the total output power has a local minimum, similar to the local minimum indicated as “B” in Fig. 4.10a.

If we compare the range of absolute cavity lengths ΔL at which these effects occur for Figs. 4.10a and 4.11, we notice that it is almost the same, even though there is a factor of 12 difference in radius of curvature of the end mirrors ($R = 25$ mm and $R = 2.1$ mm, respectively), i.e., a factor of 12 difference in absolute cavity length L. As the only dimension that is unchanged between these two experiments is the thickness of the Nd:YVO$_4$-crystal, this suggests that the absolute length scale at which these effects occur is set by this crystal thickness. Here we may think of gain-guiding or thermal lensing in the Nd:YVO$_4$-crystal, or aberrations caused by the non-normal incidence of light on the plan-parallel crystal.

At the moment, we do not have an explanation for the occurrence of the “V”-shaped mode of Fig. 4.11c. One possibility is that the above-mentioned effects (gain-guiding, thermal lensing and aberrations in the crystal) cause the “V”-shaped mode to be (more) stable, while conventional axial modes are (more) unstable. Another possibility is that diffractive effects play a role in stabilising this mode. Highly suggestive in this context are the “V”-shaped modes found both numerically and experimentally in plano-concave microwave resonators [39]; these modes rely crucially on diffractive effects at the edge of the concave mirror.

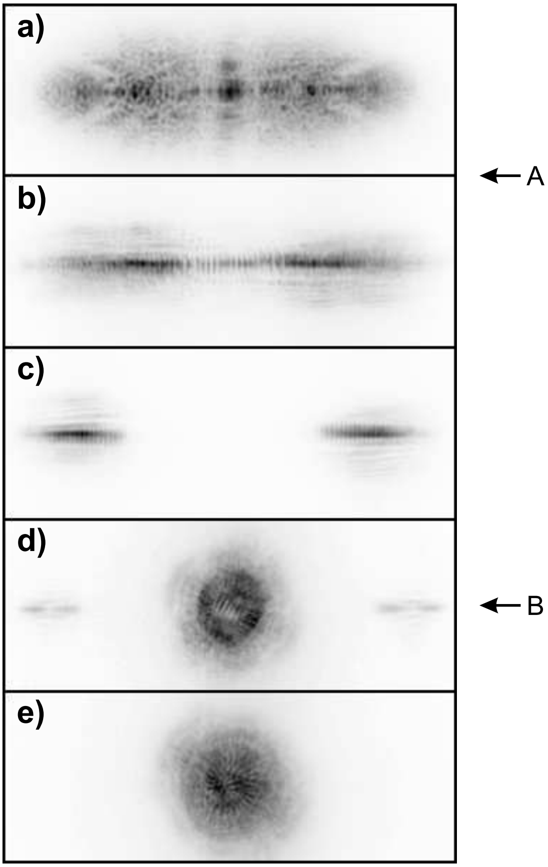

Figure 4.11: *Transverse near field beam profiles, taken at the concave cavity mirror. The concave mirror had a radius of curvature of* $R = 2.1$ mm. *(a)* $\Delta\ell = -0.7\%$ *(*$\Delta L = -15\ \mu$m*), (b)* $\Delta\ell = -0.2\%$ *(*$\Delta L = -5\ \mu$m*), (c)* $\Delta\ell = 0\%$*, (d)* $\Delta\ell = 0.2\%$ *(*$\Delta L = 5\ \mu$m*), (e)* $\Delta\ell = 0.5\%$ *(*$\Delta L = 10\ \mu$m*). Greyscales have been adjusted to increase contrast. The arrows indicate the location of minima in the total output power, similar to those in Fig. 4.10a.*

Equally unexplained is the central spot of Figs. 4.11d and e, where emission is both at a different wavelength and with a different polarisation compared to normal lasing. For stable cavities, this “nonstandard” laser operation is prevented by the difference in gain between the two situations. For slightly unstable cavities, this gain difference can apparently be compensated for by increased losses for lasing at the standard wavelength and polarisation, although it is mysterious what the exact mechanism is. This nonstandard lasing is even more surprising if one realises that normal Nd:YVO_4-based laser output is polarised along the *extraordinary* crystal axis. As $n_e > n_o$, the geometric cavity length for light polarised along the ordinary axis is larger (see Eq. (4.5)), so that the cavity should be more unstable, contrary to our observations.

4.6 Concluding discussion

Despite all our attempts, of which the above is only a choice selection, a cavity random laser has eluded us. The requirements as outlined by Ambartsumyan *et al.* [20], to have a large number of modes oscillating which are nondegenerate, have equal losses, and overlap, could never be fulfilled in the same experiment.

For resonators with (nearly) frequency degenerate cavity configurations, careful control of the cavity length did allow us, in principle, to create an overlapping, nondegenerate mode manifold. However, with the pump laser available to us, except for cavities close to hemiconcentric, it was not possible to make the pump spot sufficiently large so that many modes had roughly the same laser threshold. Close to hemiconcentric, we managed to get around $\sim 10^3$ modes to lase. However, as we can resolve individual beat peaks in Fig. 4.6c, there the condition of mode overlap was not fulfilled. Bringing the cavity even closer to hemiconcentric, to reduce the mode-mode distance, increased the laser threshold prohibitively.

Furthermore, for lasers with a pump profile as uniform as our pump laser ($P_{\text{pump,max}} \approx$ 380 mW) allowed, we have not observed avoided mode crossings as evidence of mode mixing. A possible way to induce mode mixing is to enhance the influence of the gain medium, either by increasing the pump power, thereby making use of the nonlinearity of the gain medium, or by disturbing the uniformity of the pump, making use of the overlap between pump profile and laser modes. As we could not increase the pump power sufficiently (because of the limited power of our pump laser), we opted for the second approach, by pumping the laser off-axis. However, as demonstrated in chapter 2, instead of avoided crossings, around degenerate cavity configurations we observed mode pulling and frequency locking effects (“geometric modes”). These effects are very interesting in their own right, but quite the opposite of what we had hoped for.

Even though a cavity random laser stayed out of reach, our experiments turned up surprising results at the edge of resonator stability. As we saw in section 4.4.2, the transition between a stable and an unstable resonator is far less abrupt than expected from geometric considerations. Another surprising observation is that this transition is not monotonous: the output power shows local minima, coinciding with sudden changes in the shape of the lasing mode, as shown in section 4.5. Experimental evidence suggests that, in blurring this transition between stable and unstable cavities, gain guiding, thermal lensing, aberrations and diffraction play a role, although a full explanation is lacking. It would be useful to study this transition from a stable to an unstable cavity in a *passive* system (i.e., omitting the gain medium), since in that case diffraction is the only conceivable blurring mechanism.

In conclusion, creating a cavity random laser based on a two-mirror cavity design is not as simple as we had hoped at the outset. A more fruitful line of investigation may be a cavity random laser based on a three-mirror folded cavity. As we will show in the next chapter, such a cavity can be built using standard optical components, and shows *wave chaos*. This may, then, pave the way towards a cavity random laser, a random laser without randomness.

4.7 Appendix: Calibrating the length of the resonator

The length of the resonator is controlled by shifting the position of the concave mirror using a micrometer screw. The question of calibrating the length of the resonator is then that of finding the relation between the setting of this micrometer screw L_{set}, and the geometric cavity length $\tilde{L}$. If we express L_{set} and $\tilde{L}$ in the same units, we find

$$\tilde{L} = L_{\text{offset}} + L_{\text{set}}\,, \tag{4.13}$$

with L_{offset}, the offset between geometric cavity length and micrometer setting, our calibration parameter. Alternatively, we may specifically be looking for the micrometer setting at which the cavity is hemiconcentric, $L_{\text{set,conc}}$. We then find that

$$\tilde{L} = R - L_{\text{set,conc}} + L_{\text{set}}\,, \tag{4.14}$$

with R the radius of curvature of the mirror.

To find L_{offset} or $L_{\text{set,conc}}$, we first make an *a priori* estimate for L_{offset} by directly measuring, for a given L_{set}, the nominal resonator length L, and calculating $\tilde{L}$ using Eq. (4.1). Then, we record L_{set} for a large number of frequency-degenerate cavity configurations. These configurations can be observed in the total laser output power, as in Fig. 2.6, or as changes in the transverse emission profile (compare, for example, Figs. 2.2 and 2.3). Based on the *a priori* estimate for L_{offset} we can assign Gouy phases $2\pi K/N$ to these configurations. In this process the experimental observation that the qualitative "strength" of the effect in either total output power or transverse emission profile is larger for smaller K may be helpful; for example, the degeneracy $K/N = 1/3$ is more prominent than the degeneracy $K/N = 7/20$. In Fig. 4.12 we plot the micrometer screw setting L_{set} against the Gouy phase $\theta/2\pi$ for 34 degenerate cavity configurations.

Combining Eq. (4.13) with Eqs. (4.3) and (4.4), we find that

$$L_{\text{set}} = \tilde{L} - L_{\text{offset}} = R\left(1 - \left(\cos\frac{\theta}{2}\right)^2\right) - L_{\text{offset}} = R\left(\sin\frac{\theta}{2}\right)^2 - L_{\text{offset}}\,. \tag{4.15}$$

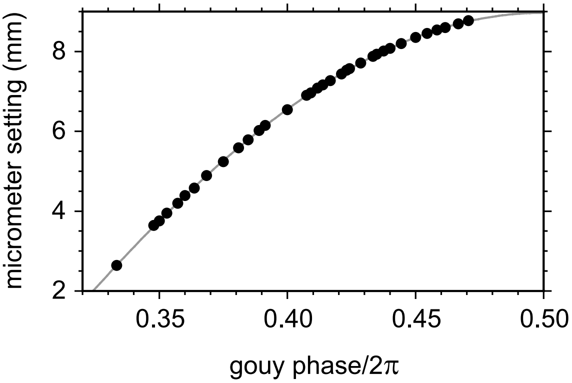

Figure 4.12: *Micrometer setting L_{set} versus (assigned) Gouy phase $2\pi K/N$ for 34 degenerate cavity configurations. The grey curve is a fit using Eq. (4.15) or Eq. (4.16).*

Alternatively, combining Eq. (4.14) with Eqs. (4.3) and (4.4), we find that

$$L_{\mathrm{set}} = \tilde{L} - R + L_{\mathrm{set,conc}} = L_{\mathrm{set,conc}} - R\left(\cos\frac{\theta}{2}\right)^2. \tag{4.16}$$

These two equations are, of course, equivalent, as can be verified using Eqs. (4.13) and (4.14).

We may now fit either equation to the data in Fig. 4.12, using as fitting parameters R and either L_{offset} or $L_{\mathrm{set,conc}}$ (we fit the mirror radius of curvature R to verify the specifications of the mirror). From the grey curve in Fig. 4.12 we see that the fit is very good. We find that $R = 25.30(3)$ mm, $L_{\mathrm{offset}} = 16.33(2)$ mm and $L_{\mathrm{set,conc}} = 8.970(3)$ mm. As such, the uncertainty in the position of $\Delta L = 0$ in Fig. 4.10 is about 3 μm.

Chapter 5

Observation and manipulation of wave chaos in a folded optical resonator[1]

We present an experimental study of the multi-mode spectrum of a folded, three-mirror optical resonator. In comparison with a two-mirror resonator the use of a concave folding mirror enhances the effective nonparaxiality, which, combined with the lowered symmetry of the system, may lead to wave chaos*. Based on the dependence of the Gouy phase on the folding angle, we estimate theoretically that wave chaotic behaviour may occur for folding angles* $2\alpha > 4^\circ$*. As transmission spectra for this system are largely filled, it is not possible to extract nearest-neighbour or other spectral statistics. Instead, we look at the wave packet survival probability, averaged twice, over both input conditions and realisations of the system. This survival probability exhibits, for chaotic spectra, a so called* correlation hole*, contrary to regular spectra. Our experimental results show that nonparaxial perturbations, as introduced by the concave folding mirror, cause wave chaotic behaviour for folding angles* $2\alpha = 20^\circ$ *and larger. The strength of these perturbations, and thereby the amount of chaos, can be increased through increasing the folding angle, or through increasing the effective opening angle of the system.*

---

[1] J. Dingjan, E. Altewischer, M.P. van Exter, and J.P. Woerdman, “Experimental observation of wave chaos in a conventional optical resonator”, Phys. Rev. Lett. **88**, 064101 (2002); J. Dingjan, M.P. van Exter, and J.P. Woerdman, “Manipulating optical wave chaos in an open cavity”, in preparation.

5.1 Introduction

Classical chaos is the phenomenon where the dynamics of a deterministic system, while limited to a finite part of phase space, is critically sensitive to initial conditions. The combination of these two features leads to intensive mixing in phase space. Well-known examples of such systems are the weather system and the behaviour of billiard balls inside a stadium-shaped billiard. Wave chaos is usually defined as the wave-mechanical behaviour of systems that are classically chaotic. Note that this is a somewhat loose description; currently there is no explicit criterion for chaos in a wave theory.

One may deal with classical waves, as occur in acoustic, hydrodynamic and microwave systems, or with quantum waves, as occur in atoms, molecules, nuclei, quantum dots and other quantal systems [37, 15]. For two-dimensional systems, wave chaos is equivalent to quantum chaos, since the Helmholtz equation can be mapped onto the Schrödinger equation [15]; for three-dimensional systems this is not the case. In this chapter we will focus on a novel experimental demonstration of *optical* wave chaos.

In a broad context, optical wave chaos has appeared in experiments on chaotic microresonators [40, 33, 41], localisation of light [42, 43, 44] and random laser action [45, 46, 47]. However, the microscopic nature of the material systems used in these experiments (microresonators [40, 33, 41], suspensions [42, 45] or powders [43, 46]), and the associated difficulty in fabrication and reproducibility, has not allowed the same spectacular progress as, for example, microwave experiments [15,48,49]. There, the use of closed, stadium-type resonators allows excellent control over the relevant experimental parameters. Extending this degree of control into the optical domain would be a tremendous boost for optical wave chaos experiments. It would allow study of quantum-mechanical effects (such as spontaneous emission and lasing) that are absent for microwaves. Also, contrary to the microwave domain, spatially chaotic patterns can easily be imaged in the optical domain. From a general perspective, the optical domain is preferable since it allows one to explore much further into the asymptotic domain where wave and ray chaos meet [50], since the ratio of system size and wavelength can be made very much larger than in the microwave domain[1]. Finally, such an optical implementation may open up new opportunities for research into enhanced backscattering (weak localisation), and even Anderson localisation of light, phenomena that require chaotic scattering [44, 51].

In this chapter we report the observation of wave chaos in the optical regime in a surprisingly simple system, namely a folded optical resonator operating in the multi-transverse-mode regime (see Fig. 5.1) [52]. This resonator, formed by standard optical components, is a truly macroscopic system, and it allows excellent control as well as easy fabrication. Apart from enabling the above-mentioned experiments that require optical wave chaos, this system is of great interest in its own right, since it allows what seems to be the first demonstration of wave chaos in an extremely open resonator.

---

[1] For comparison: a folded three mirror *microwave* resonator that would support the same number of transverse modes as our optical resonator would need to have the same Fresnel number $N_\mathrm{F} = a^2/(\lambda L)$, with $2a$ the mirror diameter, L the resonator length and λ the wavelength. If we keep the ratio a/L constant, we see that, for a comparable microwave resonator, both the mirror diameter and resonator length have to be scaled up by a factor $\lambda_\mathrm{micro}/\lambda_\mathrm{opt}$, which is typically around 10^4. Therefore, our $\sim$ 30 cm long resonator with convenient 25 mm diameter mirrors would become as big as a university campus.

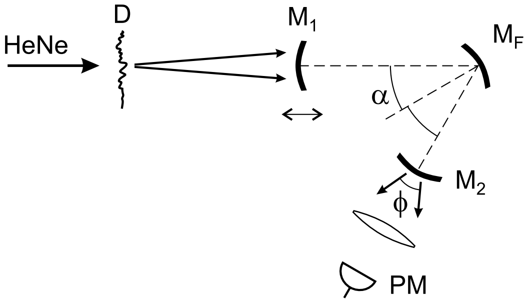

Figure 5.1: *Experimental setup. HeNe: helium-neon laser beam, D: diffusor,* M_1,M_2*: resonator end mirrors,* M_F*: folding mirror, and PM: photomultiplier. The figure shows the aberrated resonator, which has a concave folding mirror* M_F*. The use of a flat folding mirror leads to a nonaberrated resonator. Indicated is the modal opening angle* ϕ*.*

Furthermore, we study how the wave chaos in such a folded optical resonator depends on the geometry of the setup (see Fig. 5.1). To achieve the nonseparability of the wave equation (including boundary conditions) that is required for chaos, the resonator operates in the nonparaxial regime, where the nonparaxial perturbations are strongly enhanced by the curved folding mirror M_F. This enhancement is a direct consequence of the non-normal incidence of light on the curved folding mirror, as will be explained in section 5.2.1. Varying either the folding angle of our resonator, 2α, or the opening angle of the highest-order excited transverse modes, ϕ, allows us to manipulate the nonparaxial perturbations of the system. As it is the nonparaxiality that causes nonseparability, we expect (and confirm experimentally) that these variations strongly affect the chaotic properties of our system.

Conceptually, our system is related to billiard type chaotic resonators (such as the stadium billiard), in the sense that the chaotic behaviour of the system depends on the shape of the boundary of the resonator [15]. The key difference, of course, is that the majority of such billiard systems are closed, whereas our resonator is very open. Open resonators have received attention in the context of wave chaos, but only in very small systems that could not be easily manipulated [40, 33, 41].

Because of the intimate relation between ray (or classical) chaos and wave chaos, analysing the ray behaviour of wave-chaotic systems can offer a lot of insight in the properties of such systems. Therefore, throughout this chapter we will draw on both ray mechanics and wave mechanics when we discuss our folded optical resonator, which, by its nature, is of course purely wave-mechanical.

For “traditional” billiard systems, the combination of suitably chosen shaped boundary conditions and symmetries makes it possible, through analytical or numerical approaches, to get information on the ray behaviour, or classically chaotic dynamics [53, 54]. For classically chaotic systems, plots of trajectories in phase space, or Poincaré-sections, can give a lot of insight in the dynamics. In general, one finds that these systems have a *mixed* phase space, containing both fully regular and fully chaotic regions.

Obtaining Poincaré-sections for a folded, very open resonator is not trivial. As a first complication, the resonator must, due to lack of cylindrical symmetry, be treated as a fully three-dimensional system. Furthermore, we must distinguish between rays that stay confined inside the resonator, and rays that will, at a certain point, miss one of the mirrors and escape. Because of these complications, the phase space of our folded resonator has not yet been mapped, although work on this has started [55]. Therefore, the theoretical discussion in this chapter will be mainly restricted to the *diagnostics* of the wave chaotic behaviour of our system.

In section 5.2.1 we will discuss the role of nonparaxial perturbations in achieving wave chaos in a folded optical resonator. We shall use the notion of lens (or mirror) aberrations to estimate when chaos might occur. Then, in section 5.2.2 we will describe the experimental setup, and identify the key parameters. Since the resonator finesse, $\mathscr{F}$, is considerably smaller than the number of excited modes, N, the spectral resonances in the resonator transmission spectrum will overlap, so that standard spectral statistical approaches that, for chaotic systems, show effects such as level repulsion and spectral rigidity, will fail. Therefore, in section 5.2.3 we describe an alternative method, devised by Wilkie and Brumer [56] (see also [57, 58, 59, 60]) for diagnostics of chaotic molecular spectra with overlapping lines. This is followed by a report of the experimental results when varying the folding angle 2α (section 5.3.1) and the maximum modal opening angle ϕ (section 5.3.2). Finally, we will finish with a concluding discussion in section 5.4.

5.2 Folded optical resonator

5.2.1 Nonseparability

In the paraxial approximation, the scalar wave equation, or Helmholtz equation,

$$\nabla^2\psi + k^2\psi = 0\,, \tag{5.1}$$

reduces to the simpler paraxial wave equation,

$$\nabla_t^2 U - 2ik\frac{\partial U}{\partial z} = 0\,, \tag{5.2}$$

where ∇_t refers to the transverse coordinates x and y only. This reduced equation, in combination with a quadratic approximation of spherical optical elements (e.g., lenses and mirrors), leads to a fully separable problem. This applies, for instance, to a regular two mirror resonator, and the resulting eigenmodes are the well known Hermite-Gaussian or Laguerre-Gaussian functions, with eigenfrequencies

$$\nu_{q,mn} = \nu_q + \nu_m + \nu_n \tag{5.3}$$

depending on the longitudinal and transverse mode indices q, m and n.

However, for chaos to be possible, the wave equation (including the boundary conditions) describing the system must become sufficiently nonseparable, which implies a strong enough violation of the paraxial approximation. Then, the longitudinal and transverse mode indices labelling the Hermite- or Laguerre-Gaussian modes, native to a paraxial optical resonator, lose their meaning. This will occur first for the highest order transverse modes supported by the resonator. This is analogous to the occurrence of quantum chaos due to the disappearance of normal eigenmodes in highly vibrationally excited molecules [61], where the vibrational quantum numbers may be compared with the transverse mode indices.

In a two mirror cavity with spherical mirrors, the strength of nonparaxial perturbations will remain limited, unless the opening angle of the system becomes inconveniently large, typically $\phi > 60^\circ$, where ϕ is the full opening angle (see p. 630 of ref. [7]). Instead, we study a three mirror folded linear cavity, formed by two high-reflectivity end mirrors, which can be either flat or curved, and a high-reflectivity *curved* folding mirror (see Fig. 5.1). In this resonator, the perturbations due to nonparaxiality are strongly enhanced by the non-normal incidence of light on the curved folding mirror $\mathrm{M_F}$; furthermore, the folding breaks the cylindrical symmetry of the system. As we will see, relatively small values of the opening angle ϕ are then sufficient to produce wave chaos.

To illustrate the beneficial role of the concave folding mirror, it is instructive to consider the nonparaxial perturbations as introduced by a curved mirror in the context of the theory of lens aberrations. This will serve as a guide on how to change the resonator geometry in order to affect the wave chaos in our system. We may consider the axis of the folded three mirror resonator as a (known) base ray, and study rays that make a small angle with this base ray, the parabasal approximation [62]. Even for zero opening angle ϕ, the non-normal incidence on the curved folding mirror introduces an appreciable astigmatism for nonzero folding angles 2α (see section 5.3 of ref. [63]). For finite opening angle ϕ, and in lowest order, the five Seidel aberrations (astigmatism, coma, spherical aberration, distortion, and curvature of field) will become important, their effect boosted relative to a paraxial system because of the folding angle α [63]. To understand this boosting effect, we can look at, for example, the general expression for the contribution of astigmatism to the total wave aberration,

$$\Phi = -C y_0^2 \rho^2 \cos^2\theta \,, \tag{5.4}$$

where y_0 is the off-axis distance in the object plane, ρ and θ are polar coordinates in the plane of the optical element and C is a system-dependent constant. For a conventional paraxial optical system, both y_0 and ρ are generally small parameters, so that, loosely speaking, the strength of the astigmatism scales as the *fourth* power of a small parameter. However, using a curved mirror under non-normal incidence can also be interpreted as giving y_0 a large offset, with small variations around it, so that the aberration now scales as the *third* power of a small parameter, dramatically enhancing its strength[1]. Similar considerations hold for the other Seidel aberrations. Therefore, we expect the strongest nonparaxiality, and hence the strongest chaos, for large folding angles 2α. Also, for a given α, the effective nonparaxiality will increase when increasing the opening angle ϕ (this corresponds to increasing ρ in Eq. (5.4)).

It is also useful to discuss the effective nonparaxiality of a resonator from the perspective of the Gouy phase. The Gouy phase θ is a well known concept for a paraxial resonator (see p. 682 of ref. [7]); it is defined as the excess phase of the fundamental Hermite-Gaussian mode relative to a reference plane wave after one round trip. For a paraxial two-mirror resonator, it only depends on the ratios of the mirror radii R_1 and R_2, and the resonator length L, via the resonator parameters $g_{1,2} = 1 - L/R_{1,2}$,

---

[1] The quadratic term ($\propto \rho^2$) plays the role of an additional cylindrical lens, and gives rise to Coddington's equations for the effective radius of curvature of the folding mirror [62]: $R_\mathrm{T} = R\cos\alpha$ for the tangential plane and $R_\mathrm{S} = R/\cos\alpha$ for the sagittal plane.

$$\cos\theta = 2g_1 g_2 - 1 \ . \tag{5.5}$$

Higher order modes acquire a (round trip) phase difference that is an integer multiple of the fundamental Gouy phase,

$$\theta_{mn} = (m+n+1)\,\theta \ . \tag{5.6}$$

The frequency of a Hermite-Gaussian mode with longitudinal mode index q and transverse mode indices m,n is then given by

$$\nu_{q,mn} = \frac{c}{2L}\left(q + \frac{\theta_{mn}}{2\pi}\right) = \frac{c}{2L}\left[q + (m+n+1)\frac{\theta}{2\pi}\right] , \tag{5.7}$$

which has the separable structure as emphasised in Eq. (5.3).

The Gouy phase thus determines the spectral distance between neighbouring transverse modes sharing the same longitudinal mode index q. At the same time, as the eigenvalues of the round trip *ABCD*-matrix of the resonator are $\mathrm{e}^{\pm i\theta}$ (see p. 600 and 836 of ref. [7]), the Gouy phase describes the paraxial ray behaviour in the system, illustrating the dual nature of wave and ray optics in resonators (see chapters 2 and 3).

In a parabasal folded resonator consisting of three mirrors, there is not one but two Gouy phases, θ_T and θ_S, one each for the tangential and sagittal planes of the resonator; these phases depend on the folding angle 2α. They can be calculated in a straightforward manner, combining, for each of the two planes, Coddington's equation for the effective radius of curvature of the folding mirror [62] with the standard *ABCD*-matrix method [7]. The resulting spectrum is given by

$$\nu_{q,mn} = \frac{c}{2L}\left(q + \left(m+\tfrac{1}{2}\right)\frac{\theta_\mathrm{T}}{2\pi} + \left(n+\tfrac{1}{2}\right)\frac{\theta_\mathrm{S}}{2\pi}\right) , \tag{5.8}$$

where a straightforward rearrangement of terms shows that it consists of "families" of transverse modes with equal $n+m$. The distance between neighbouring families, for given q, is given by the average Gouy phase $(\theta_\mathrm{T}+\theta_\mathrm{S})/2$, whereas the spacing of modes within a family is given by the difference Gouy phase $\theta_\mathrm{T}-\theta_\mathrm{S}$. Even though the thus described spectrum is more complicated than that of a paraxial resonator *without* astigmatism, the fact that, instead of just one Gouy phase, we now need two Gouy phases to describe the paraxial spectrum is in itself not sufficient to generate chaos; the problem is again separable (cf. Eq. (5.3)).

We can, however, use the folding angle dependence of these two Gouy phases to get a rough estimate at what parameters wave chaos could become relevant. Due to the folding angle dependency of both Gouy phases, light travelling at an angle to the axis of the folded resonator will experience a different Gouy phase than light travelling parallel to the axis. Since the Gouy phase is intimately related to the eigenfrequencies of a system, this Gouy phase difference immediately translates to a spectral shift of the resonances involved. Based on this notion we can now estimate the maximum variation in Gouy phase, and hence the maximum spectral shift, by multiplying the derivative of the Gouy phase with respect to the folding angle by the opening angle ϕ,

$$\Delta\theta_\mathrm{T,S} = \frac{\mathrm{d}\theta_\mathrm{T,S}}{\mathrm{d}\alpha}\phi \ . \tag{5.9}$$

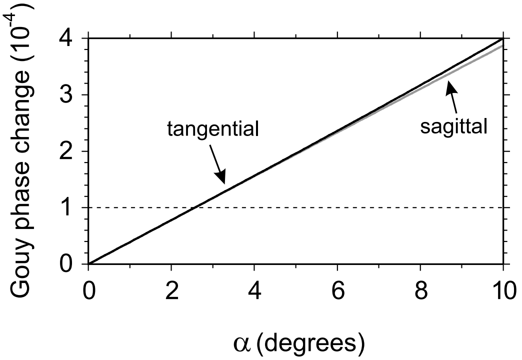

Figure 5.2: *Gouy phase variations* $\left|\dot{\theta}_T\right| \cdot \phi/2\pi$ *and* $\left|\dot{\theta}_S\right| \cdot \phi/2\pi$ *(where* $\dot{\theta} = \mathrm{d}\theta/\mathrm{d}\alpha$*) versus resonator folding angle* α*, for the resonator geometry used in our experiments (see section 5.2.2). These quantities represent the spectral shift as a fraction of the free spectral range. The curves correspond to the tangential and the sagittal plane, respectively. The horizontal line corresponds to the mean level spacing in the case of* $N = 10^4$ *excited transverse modes.*

To translate this to a frequency shift, we use that a free spectral range

$$\nu_{\mathrm{FSR}} \equiv t_{\mathrm{round}}^{-1} = c/2L \tag{5.10}$$

(where t_{round} is the cavity round trip time), which corresponds to a round trip Gouy phase of 2π. Therefore, the spectral shift as a fraction of the free spectral range is given by

$$\frac{\Delta\nu_{\mathrm{shift}}}{\nu_{\mathrm{FSR}}} = \frac{\Delta\theta_{\mathrm{T,S}}}{2\pi} = \frac{\mathrm{d}\theta_{\mathrm{T,S}}}{\mathrm{d}\alpha}\frac{\phi}{2\pi}\,. \tag{5.11}$$

For small spectral shifts $\Delta\nu_{\mathrm{shift}}$, the spectrum will be only weakly perturbed, and one can still recognise the unperturbed, “parabasal” spectrum, in the sense that one can still label the perturbed resonances with their original mode indices. However, if $\Delta\nu_{\mathrm{shift}}$ is comparable to or larger than the average inter-mode spacing $\Delta\nu$, the deviation from the “regular” spectrum will be too large to handle perturbatively, and hence, chaos will be a possibility.

In Fig. 5.2 we plot, for the resonator used in our experiments (see section 5.2.2), $\left|\dot{\theta}_{\mathrm{T}}\right| \cdot \phi/2\pi$ and $\left|\dot{\theta}_{\mathrm{S}}\right| \cdot \phi/2\pi$ (where $\dot{\theta} = \mathrm{d}\theta/\mathrm{d}\alpha$) as a function of folding angle α (for an experimental opening angle $\phi \sim 1.25°$). Also indicated is the average level spacing as a fraction of the free spectral range, for the case $N = 10^4$ modes (this is a representative case, see below). We see that already for α as low as 2°, the effects of nonparaxiality have the potential of causing wave chaos.

5.2.2 Setup

Our resonator consists of three high-reflectivity concave mirrors with a diameter of 25 mm and a radius of curvature of 1 m (see Fig. 5.1). They have been manufactured by Research

Electro Optics on superpolished fused-silica substrates with highly reflective dielectric multilayer coatings for $\lambda = 633$ nm, optimised at either 0° or 45° angle of incidence. The 0° mirrors have a specified reflectivity of 99.99%, whereas the 45° mirrors have a specified reflectivity for s-polarised light of 99.995%. For p-polarised light the reflectivity is unspecified, but substantially lower.

The length L_1 of one arm of the resonator was varied between ~ 14 and ~ 25 cm, while the length L_2 of the other arm, between mirrors $\mathrm{M_F}$ and $\mathrm{M_2}$, was kept fixed at ~ 10 cm. These values correspond to the paraxially stable regime of the folded resonator (as can be verified using the standard *ABCD*-matrix formalism [7] in combination with Coddington's equations [62]). A total length $L \sim 24$–35 cm leads to a free spectral range $\nu_{\mathrm{FSR}} \equiv t_{\mathrm{round}}^{-1} = c/2L \sim 0.63$–0.43 GHz, where t_{round} is the cavity round trip time.

The half folding angle α can be varied from 10°–45°, the lower limit being set by the requirement that the end mirrors (and their mounts) do not obscure each other. The upper limit results from the available mirror coatings: for angles of incidence other than the design angle, the reflectivity of the coatings will be less. For $0° \leq \alpha \leq 45°$ the reflectivity of either the 0° or the 45° coating is high enough that experiments can be done at sufficient finesse $\mathscr{F}$, defined as $\mathscr{F} = \nu_{\mathrm{FSR}}/\delta\nu$, where $\delta\nu$ is the width of an individual mode; typically, $\mathscr{F} \sim 2 \times 10^3$ or better. For $\alpha > 45°$, the reflectivity of the 45° coating rapidly degrades, so that experiments cannot be done for angles significantly larger than 45°. To obtain results for $\alpha = 0°$ we use a two mirror resonator that is equivalent to a three mirror resonator with $\alpha \downarrow 0°$.

To assess the nature of the wave dynamics in our system, we measure transmission spectra of the cavity by injecting light from a frequency-stabilised single-frequency HeNe laser ($\lambda = 633$ nm) and measuring the transmitted intensity while scanning mirror $\mathrm{M_1}$ over a few wavelengths. Because of the polarisation-dependent reflectivity of the folding mirror, the polarisation of the injected light is chosen to be normal to the folding plane to maximise the resonator finesse. In addition, this prevents the occurrence of peak splitting due to birefringence of the reflective coatings which we observed for "arbitrary" input polarisations, and found to be of the order of $2 \times 10^{-3}\nu_{\mathrm{FSR}}$.

In our experiments the value of the finesse $\mathscr{F}$ of the resonator plays a crucial role. If we paraxially inject a narrow laser beam directly into the cavity, i.e., without the diffusor, we excite only a few, low-order, transverse modes. From these modes we obtain, depending on the value of α, $\mathscr{F} = 2 \times 10^3$–$5 \times 10^3$ (this corresponds to $Q \equiv \nu/\delta\nu = 1.5 \times 10^9$–$5.5 \times 10^9$). The spread in these values is the result of the change in effective reflectivity of the folding mirror at different incident angles.

Before entering the cavity, the HeNe beam is first expanded by a telescope to a diameter of $2w \approx 3.4$ mm and then passes through a weak diffusor, with a scattering half cone angle of 0.5°, which is placed ~ 20–25 cm in front of the first mirror; the resulting speckled input field allows an appreciable spatial overlap with a large number of modes of the resonator. From the typical radius a of the light spot on the mirrors, $a \sim 0.5$–1 cm, we may estimate the number of transverse modes that are excited upon scanning the length of the resonator[1], $N \sim a^4/\lambda^2 L^2 \sim 10^4$–$10^5$.

The light that is transmitted through the cavity is collected with a lens and focused onto a photomultiplier. Figure 5.3 is a typical transmission spectrum for a resonator with $\alpha = 45°$.

---

[1] Equation (37) in chapter 19 of ref. [7] is the result for a single transverse dimension. As we consider both transverse dimensions, our expression is the square of this.

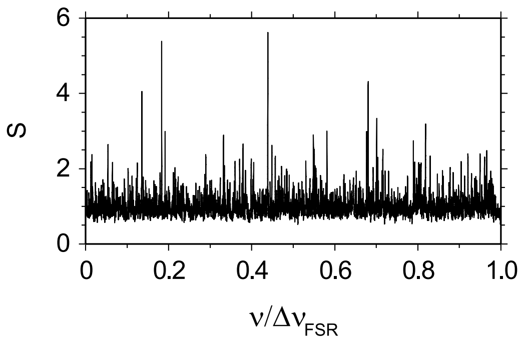

Figure 5.3: *Transmission spectrum, normalised to the transmission averaged over one free spectral range, for a resonator with* $\alpha = 45°$. *The baseline of this spectrum is* $I = 0$, *i.e., the zero-offset is due to overlap of spectral resonances.*

We shall now outline the procedure to extract information from these experimental spectra.

5.2.3 How we analyse the spectra

From the estimate of the number of excited modes and the measured finesse, we see that $N \sim 10^4$–$10^5 > \mathscr{F} = 2 \times 10^3$–$5 \times 10^3$. As a result, transmission spectra will be largely "filled" due to the overlap of peaks, so that it is impossible to resolve all individual resonances, or even a considerable fraction thereof (see Fig. 5.3). Therefore, all attempts at extracting level spacing distributions from these transmission spectra, the most commonly used analysis technique for potentially wave-chaotic systems [15], are doomed to fail, and we must look at other methods to determine whether or not wave chaos is present in our system, e.g., in a spectrum as shown in Fig. 5.3.

A technique that is eminently suited to analyse filled spectra such as ours is the one devised by Wilkie and Brumer [56]. The technique is an extention of earlier attempts at analysing highly complex molecular spectra [57, 58], and is centred around the wave packet *survival probability* $P(t)$. This quantity describes the survival probability after a time t of an initial wave packet $\psi(0)$, and can, for a lossless system, either be found from the normalised wave function $\psi(t)$, or determined from the Fourier transform of the normalised spectrum $S(\omega)$ corresponding to that initial wave packet,

$$P(t) \equiv |\langle\psi(0)|\psi(t)\rangle|^2 = \left|\int S(\omega) \mathrm{e}^{-i\omega t} \mathrm{d}\omega\right|^2, P(0) = 1. \tag{5.12}$$

We observe that $P(t)$ is, in effect, the Fourier transform of the spectral autocorrelation function. Note that for a lossless system the spectrum consists of δ-spikes.

This wave packet survival probability $P(t)$ is averaged twice, over different realisations of the system and over initial conditions, to obtain $\langle\langle P(t)\rangle\rangle$. Starting from work by Pechukas [64, 65], Wilkie and Brumer [56] show that for the lossless system $\langle\langle P(t)\rangle\rangle$ has the special property that, in the case of a chaotic system, $\langle\langle P(t)\rangle\rangle$ *must* fall below its long time asymptote

$\langle\langle P(\infty)\rangle\rangle$ for some times t, whereas in the case of a regular system, $\langle\langle P(t)\rangle\rangle$ can *never* fall below $\langle\langle P(\infty)\rangle\rangle$:

$$\forall t: \langle\langle P(t)\rangle\rangle \geq \langle\langle P(\infty)\rangle\rangle \text{ for regular dynamics,} \tag{5.13a}$$

$$\exists t: \langle\langle P(t)\rangle\rangle < \langle\langle P(\infty)\rangle\rangle \text{ for chaotic dynamics.} \tag{5.13b}$$

As a result, this method unambiguously identifies the dynamics as being regular or chaotic. Furthermore, the asymptotic behaviour of $\langle\langle P(t)\rangle\rangle$ is directly related to the number of spectral lines (or modal resonances) N in the interval under consideration,

$$\langle\langle P(\infty)\rangle\rangle = \frac{2}{N+1}. \tag{5.14}$$

The region where $\langle\langle P(t)\rangle\rangle < \langle\langle P(\infty)\rangle\rangle$, in general found for small t [59, 66, 60], is called the *correlation hole*. This correlation hole also occurs when the classical dynamics of a system are not fully chaotic, but are in an intermediate or mixed regime [59, 60]. The size and shape of the correlation hole are related to the spectral statistics. The depth of the hole measures the long-range correlation between levels ("spectral rigidity"), whereas the area of the correlation hole is related to the degree of level repulsion [60].

Because $P(t)$, being the Fourier transform of the spectral autocorrelation function, can be obtained directly from experimental spectra, and does not require peak finding or similar preprocessing, methods employing $P(t)$ are very robust. In the case of complicated spectra, with many overlapping peaks, these methods are superior to direct frequency-domain methods, such as those examining level repulsion or spectral rigidity [57, 58]. Using the doubly-averaged spectral *autocorrelation* function to distinguish between regular and chaotic dynamics is, in principle, equivalent to the Wilkie-Brumer method. However, for badly resolved spectra the *survival probability* $\langle\langle P(t)\rangle\rangle$ again outperforms the alternative [57, 58].

As will be explained in more detail in chapter 6, in our experiments averaging over initial wave function conditions is achieved by recording transmission spectra for a number of different transverse positions (typically 10) of the diffusor placed before the resonator. Varying the position of the diffusor will change the exact configuration of the speckled input field impinging on the resonator, and will thereby give rise to different couplings to the individual intracavity modes. If we cross-correlate results for different transverse positions of the diffusor, we find that in our experiments shifting the diffusor by 1 mm leads to completely uncorrelated transmission spectra (see section 6.3.3).

To implement different realisations of the system, we change the length of the resonator in steps δL much larger than λ (typically $\delta L = 1$ mm), and average over the resulting spectra. These length changes lead to differently structured eigenfrequency spectra, as will be demonstrated in section 6.3.2. However, since the character and strength of the aberrations caused by the concave folding mirror do not change, these spectra can be seen as different realisations of the *same* system.

We found that some realisations, i.e., some choices of L_1, L_2 and α, show quasiperiodic transmission spectra, giving rise to strong Fourier components in $P(t)$. In the paraxial limit, such quasiperiodic transmission spectra occur for resonators that support closed periodic orbits (chapters 2 and 3 of this thesis, refs. [1, 67]). Apparently, some of these closed periodic orbits survive upon going to a nonparaxial resonator. As the corresponding strong spikes in the Fourier transform are very sharp, only a single data point wide, and isolated, they do not affect the general trend of the $\langle\langle P(t)\rangle\rangle$-curves. For reasons of clarity of the graphs of $\langle\langle P(t)\rangle\rangle$ we have therefore chosen to perform a postselection on our data. Similar procedures have been used by other authors [48, 68, 69].

This postselection procedure is as follows. Typically, we record transmission spectra for 50 distinct lengths of the resonator. For each resonator length we use 10 different transverse positions for the incoupling diffusor, resulting in a total of 500 transmission spectra. After normalising we apply Eq. (5.12) to these spectra $S_{\mathrm{exp}}(\omega)$ to obtain 500 curves $P_{\mathrm{exp}}(t)$. Subsequently, we average $P_{\mathrm{exp}}(t)$ over diffusor positions, resulting in 50 $\langle P_{\mathrm{exp}}(t)\rangle$-curves, one for every resonator length. Of these, we reject the 10 curves with the strongest principal Fourier components. The remaining 40 are averaged to $\langle\langle P_{\mathrm{exp}}(t)\rangle\rangle$. This selection removes the sharp, isolated peaks apparently resulting from periodic orbits, as explained above, without affecting the overall shape of $\langle\langle P(t)\rangle\rangle$. A detailed discussion of the correlation properties of the spectra as a function of diffusor position and resonator length, as well as the "remnant" periodic orbits will be reported in chapter 6.

5.2.4 How we deal with losses

In our experiments, dissipation is impossible to avoid; it is dominantly due to the finite reflectivity of the mirrors ($< 100\%$). As a result, experimental spectra will not consist of ideal δ-spikes, but instead all resonances have a finite width, and $\langle\langle P_{\mathrm{exp}}(t)\rangle\rangle$ contains a decaying term. To be able to apply the conditions in Eq. (5.13), we must transform $\langle\langle P_{\mathrm{exp}}(t)\rangle\rangle$ to the "decay-free" $\langle\langle P(t)\rangle\rangle$. Wilkie and Brumer have shown that one can transform the wave packet survival probability for a lossy system, directly obtained from the experimental spectrum using Eq. (5.12), to the $P(t)$ of the underlying lossless system [56], provided each individual transmission spectrum can be viewed as a convolution of an ideal spectrum consisting of δ-spikes (or "sticks"), and a known basic line shape $\ell(\omega)$. In the Fourier domain, this convolution then reduces to a simple multiplication of the Fourier transform of the delta spectrum, $P(t)$, and that of the fundamental line shape, $\mathscr{L}(t)$. The decay-free $\langle\langle P(t)\rangle\rangle$ is then related to the experimentally obtained $\langle\langle P_{\mathrm{exp}}(t)\rangle\rangle$ through

$$\langle\langle P(t)\rangle\rangle = \frac{\langle\langle P_{\mathrm{exp}}(t)\rangle\rangle}{|\mathscr{L}(t)|^2} . \tag{5.15}$$

For optical resonators, the shape of the resonances is a Lorentzian,

$$\ell(\omega) = \frac{2}{\pi}\frac{1}{\Delta\omega}\left\{1 + 4\left(\frac{\omega}{\Delta\omega}\right)^2\right\}^{-1} , \tag{5.16}$$

where $\Delta\omega$ is the full line width at half maximum. The Fourier transform of this fundamental line shape is given by

$$\mathscr{L}(t) = \exp\left(-\frac{\Delta\omega}{2}|t|\right) = \exp\left(-\frac{\pi}{\mathscr{F}}\left|\frac{t}{t_{\mathrm{round}}}\right|\right) , \tag{5.17}$$

where we have used that the finesse $\mathscr{F} = \nu_{\mathrm{FSR}}/\delta\nu = 2\pi/\Delta\omega\, t_{\mathrm{round}}$. Indeed, the Fourier transform of experimentally obtained low-order resonances corresponds closely to a decaying

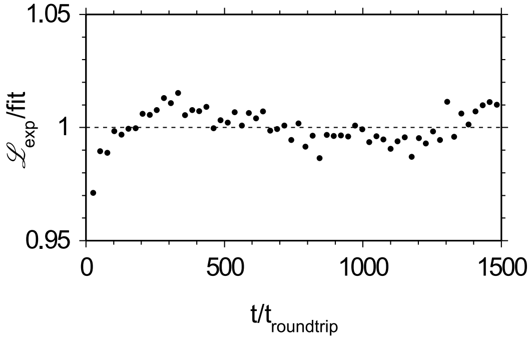

Figure 5.4: *Fourier transform of low-order resonances, divided by a fitted exponential. In fact, 20 individual resonances were recorded, Fourier transformed, and averaged. A single exponential was fitted to these data, and subsequently divided out, to highlight the deviations from exponential decay. We see that deviations stay well below* 5%.

exponential as given by Eq. (5.17), as can be seen in Fig. 5.4. As a result, we can obtain the desired "decay-free" $\langle\langle P(t)\rangle\rangle$ from the experimentally determined $\langle\langle P_{\mathrm{exp}}(t)\rangle\rangle$ through

$$\langle\langle P(t)\rangle\rangle = \langle\langle P_{\mathrm{exp}}(t)\rangle\rangle / \exp\left(-\frac{2\pi}{\mathscr{F}}\left|\frac{t}{t_{\mathrm{round}}}\right|\right), \tag{5.18}$$

where $\mathscr{F}$ can either be measured independently (by exciting only one, or at most a few, nonoverlapping paraxial resonances and directly measuring the line width), or be estimated from $\langle\langle P_{\mathrm{exp}}(t)\rangle\rangle$. This last method requires that the asymptotic behaviour of $\langle\langle P_{\mathrm{exp}}(t)\rangle\rangle$ can be recognised reliably; in our experiments this is always the case. In section 6.3.4 we take a closer look at both the line shape of our resonator and $\langle\langle P_{\mathrm{exp}}(t)\rangle\rangle$. There we will see that the asymptote of $\langle\langle P_{\mathrm{exp}}(t)\rangle\rangle$ is indeed very prominent.

5.3 Results

Having thus explained the experimental setup and the analysis procedure, we will now present the experimental results. We have studied the dependence of the wave packet survival probability on the degree of the nonparaxiality as induced by the concave folding mirror. The degree of nonparaxiality may be manipulated through the folding angle of the resonator 2α and opening angle ϕ.

5.3.1 Folding angle 2α

Adjustment of the folding angle 2α is experimentally straightforward. In Fig. 5.5 we plot $\langle\langle P(t)\rangle\rangle$, measured for five different folding angles. All curves are for identical opening angle $\phi \sim 1.25^\circ$. The smallest folding angle, $2\alpha = 0^\circ$, corresponds to a paraxial two-mirror resonator, and we see that in this case $\langle\langle P(t)\rangle\rangle$ never falls below its long time asymptote.

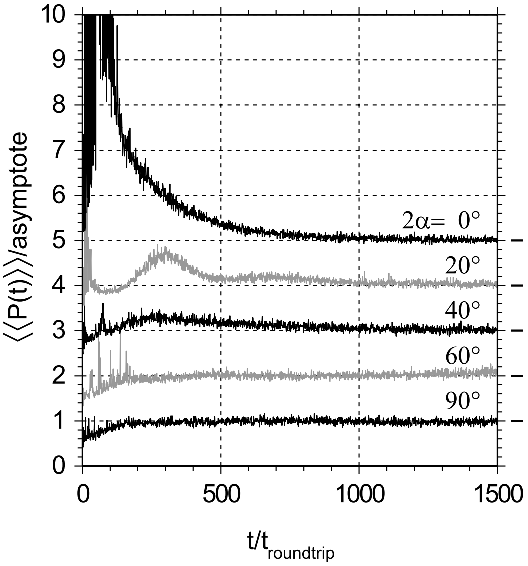

Figure 5.5: *Doubly averaged wave packet survival probability* $\langle\langle P(t)\rangle\rangle$ *for five different cavity folding angles* 2α*. The curves have been normalised to their respective asymptotes, and shifted vertically for clarity. Bars next to the right side axis indicate the location of the asymptotes for the curves.*

This confirms that, in a “normal” resonator, no chaos is present and the dynamics are purely regular.

For $2\alpha = 90^\circ$, corresponding to a resonator that has been folded through a right angle, we see that $\langle\langle P(t)\rangle\rangle$ is almost featureless, only showing a “correlation hole” below $t/t_{\text{round}} = 150$. We conclude that for such a resonator the dynamics are chaotic, as reported earlier [52].

For intermediate folding angles we see a gradual transition from the $2\alpha = 0^\circ$ to the $2\alpha = 90^\circ$ result. There does not seem to be a sharp dividing line between regular and chaotic resonators, but instead a smooth transition regime. Even for $2\alpha = 20^\circ$ a small correlation hole can be observed, which seems to indicate that even for such small folding angles chaos plays a role. If we compare the curves for $2\alpha = 60^\circ$ and $2\alpha = 90^\circ$ we see that the size and depth of the correlation hole do not change significantly; however, the “spikes” (that managed to sneak through the postselection procedure) that are present for $\alpha = 30^\circ$ for $t/t_{\text{round}} < 200$ diminish in height and number.

5.3.2 Opening angle ϕ

A second way of manipulating the strength of the nonparaxial aberrations in our resonator is by varying the opening angle ϕ. The value of ϕ depends on the size of the illuminated regions on the mirrors as well as the geometry of the resonator; it directly determines which modes will be excited in our resonator. A low value of ϕ means that only modes that do not extend too far from the optical axis are excited, whereas a higher value means that also modes with

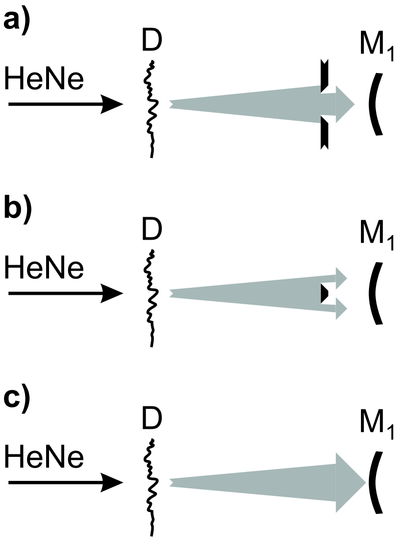

Figure 5.6: *Resonator incoupling methods to manipulate the amount of nonparaxiality through varying ϕ. (a) Injection around the optical axis only, (b) Injection away from the axis, (c) Injection both on-axis and away from the axis.*

appreciable amplitude far from the axis will contribute; for the latter modes, the nonparaxial aberrations due to the curved folding mirror will be stronger. If we select, through the way we couple light into the resonator, a subset of modes that does not extend far from the axis, we expect to see more regular behaviour. On the other hand, selecting a subset of modes that extends much further from the axis is expected to lead to more chaotic behaviour.

We select subsets of modes by modifying the light field injected into the resonator. First we use a diaphragm, with a diameter of ~ 1.4 mm, to block the outer ring of the full field after the diffusor, and we primarily excite a small region around the optical axis, as in Fig. 5.6a. Next, we *block* this region and only allow the outer ring to pass, see Fig. 5.6b; in that way, we only excite modes that extend far from the axis. Finally, we do not block any part of the input beam, allowing the entire ~ 1 cm diameter light spot to impinge on the input mirror (Fig. 5.6c); this results in a mix of the previous two cases, and we expect to see an intermediate result.

In Fig. 5.7 we plot the results of these three types of incoupling, for two different folding angles 2α of the resonator. We see that, as expected, only coupling light into the resonator in a limited region around the optical axis leads to a less pronounced correlation hole, indicating less chaos, whereas injecting light far away from the axis leads to a stronger correlation hole, indicating more chaos. For $2\alpha = 90^\circ$, the dynamics stay chaotic for all three cases; for $2\alpha = 40^\circ$, when coupling light into the resonator close to the axis only, the chaotic signature almost disappears.

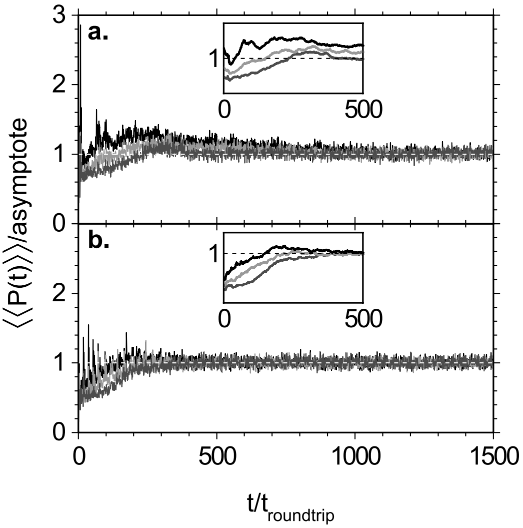

Figure 5.7: *$\langle\langle P(t)\rangle\rangle$-curves for three different types of incoupling for a resonator with: (a) $\alpha = 20°$, (b) $\alpha = 45°$. Insets show a detail of the same curves, smoothed with a 21-point moving average filter, to expose the general trend around the location of the correlation hole. For all graphs, the topmost curve (black) is for on-axis injection (cf. Fig. 5.6a), the bottom curve (dark grey) is for injection away from the axis (cf. Fig. 5.6b), and the middle curve (light grey) is for injection both on and away from the axis (cf. Fig. 5.6c).*

5.4 Concluding discussion

In conclusion, in this chapter we have demonstrated the presence of wave chaos in an effectively nonparaxial, folded three-mirror resonator consisting of standard, high-reflectivity mirrors. The experimental results in section 5.3 show that the degree of nonparaxiality, as caused by the concave folding mirror, crucially determines the nature of the wave dynamics in the system. As can be seen from the behaviour of the correlation hole in $\langle\langle P(t)\rangle\rangle$, increasing the folding angle 2α from $0°$ to $90°$ shows a smooth transition from a nonchaotic to a chaotic system; it takes the shape of a restructuring of the low t/t_{round}-parts of the curves, corresponding to relatively larger spectral distances.

To gain more insight into the dynamics of folded optical resonators it will be necessary to increase the resonator finesse $\mathscr{F}$, so that the regime $\mathscr{F} > N$ can be reached. Then, it will be possible to resolve the resonances of our cavity, allowing us to simultaneously obtain nearest neighbour spacing distributions and perform the above-mentioned analysis procedure based on $\langle\langle P(t)\rangle\rangle$. This will allow a direct comparison between the two methods of identifying chaos, and is expected to shed more light on the behaviour of $\langle\langle P(t)\rangle\rangle$ in intermediate regimes. Also, it may give more insight as to the physical interpretation of the correlation hole in $\langle\langle P(t)\rangle\rangle$, and the relation with direct spectral statistics.

Due to the lack of predictive theory for our system, we now discuss some speculative issues. For example, the sharp spikes that appear for specific resonator configurations, and the quasiperiodic transmission spectra they correspond to, call to mind similar effects in nonchaotic open resonators. For such systems, highly periodic spectra are known to occur for resonators that support closed periodic orbits [1]. This suggests that our *chaotic* open resonator may also support periodic orbits, and might point to the presence of *scars* [70].

A natural question is whether the value of the resonator finesse $\mathscr{F}$ only determines the most suitable diagnostic technique, or whether it plays a deciding role in generating chaos. A somewhat reverse question is whether the presence of chaos will degrade the resonator finesse; if a chaotic system would show an increased leakage rate compared to a regular system, its finesse will be lower. As of now, answers cannot be given because of the lack of a predictive theory of our system.

Obviously, a very interesting experiment is to study the *spatial* rather than *spectral* properties of transmission of our resonator. We may expect that the statistics of speckles in the transmitted light field depend on the nature of the dynamics inside the resonator and could be non-Gaussian, that is, quite different from the transmission statistics of a conventional paraxial multi-mode resonator.

In conclusion, our experiments have shown that a folded optical resonator is an exciting and promising wave chaotic system. On the theory side, a lot of work still has to be done to better understand this system. Experimentally, the convenience of control, combined with all the techniques and tools available in the optical regime, form a powerful combination that will enable extensive quantitative studies on the emergence and properties of chaos in very open systems.

Chapter 6

Diagnostics of wave chaos in a folded optical resonator[1]

We discuss in detail how a Fourier transform method proposed by Wilkie and Brumer (Phys. Rev. Lett. 67, 1185 (1991)) can be used to analyse wave chaos in a folded optical resonator. Because the line width of the resonances of this system is usually larger than the average distance between lines, many lines overlap, leading to spectra that are complex and largely filled. As a result, conventional analysis techniques, based on spectral statistics, cannot be used. First, we show that, for such a chaotic resonator, transmission spectra obtained through scanning the length of the resonator accurately reflect the resonance frequencies for fixed *length. Next, we show that the two types of averaging, needed in the method of Wilkie and Brumer, can be achieved by acquiring spectra for different resonator lengths and for different incoupling diffusor conditions, respectively. As a last issue, we show the validity of two assumptions that greatly simplify the application of the Wilkie-Brumer method.*

---

[1] J. Dingjan, E. Altewischer, M.P. van Exter, and J.P. Woerdman, “Diagnostics of wave chaos in a folded optical resonator”, in preparation.

6.1 Introduction

In the previous chapter we demonstrated the presence of wave chaos in the optical regime in a novel system, a folded optical resonator [52]. In our experiments, we obtained transmission spectra for which the number of participating transverse modes exceeds the resonator finesse. As a result, spectra of this system are complex and largely filled, and it is not possible to extract the location of every resonance, or even a large fraction of all resonances. Therefore, customary techniques for analysing spectra from potentially chaotic systems, such as studying nearest neighbour distributions, spectral rigidity and other spectral statistics [15], cannot be performed.

Instead, to determine whether the wave dynamics of this system are regular or chaotic we use a method specifically developed to deal with such complex, filled spectra in the context of quantum chaos in highly excited molecules [56, 58]. Although this method has several roots [64,65,57] we will refer to it as the Wilkie-Brumer method [56]. It is centred around the *wave packet survival probability* $P(t)$, which can, through a Fourier transform, be obtained directly from experimental spectra, without the need for peak detection or reduction to a spectrum of δ-spikes. The beauty of this method is that it gives a clear-cut distinction between chaotic and nonchaotic systems. Not much work has been done on the application of the Wilkie-Brumer method in practical systems, and this is the gap that we will try to (partially) fill with this chapter.

Our system, a folded conventional optical resonator, is essentially macroscopic and very open. It consists of three conventional high-reflectivity mirrors (see Fig. 6.1) that allow a great freedom in selecting and changing the geometry of the resonator, as well as insertion of additional elements into the resonator. It easily allows one to reach the asymptotic limit, i.e., the system size much larger than the wavelength. To show that this system is indeed chaotic, we measured transmission spectra by injecting light into the resonator and measuring the transmission as a function of the resonator length (see chapter 5). As mentioned above, the fact that the number of modes is larger than the finesse means that these spectra are largely filled due to mode overlap.

In section 6.2 we shall introduce the experimental setup in more detail, and describe how the diagnostic method, as described by Wilkie and Brumer [56], can be applied to our system. In section 6.3 we start by showing that transmission spectra can be obtained through scanning the resonator length. Furthermore, we determine the optimal way to achieve the averaging needed for the Wilkie-Brumer method, and show that two assumptions that greatly simplify the experimental application of that method are indeed valid. We also show that scanning the length of the resonator at a rate (somewhat) higher than the cavity decay rate does not adversely affect the results, and confirm the validity of postselection of spectra to minimise spikes that obscure the overall results. Finally, in section 6.4 we shall discuss these results, and identify possible future avenues towards a better understanding of the Wilkie-Brumer method.

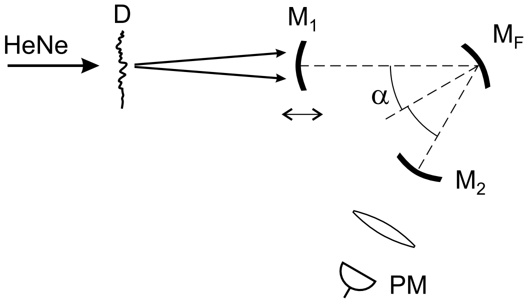

Figure 6.1: *Experimental setup. HeNe: helium-neon laser beam, D: diffusor,* M_1,M_2*: resonator end mirrors,* M_F*: folding mirror, and PM: photomultiplier. The figure shows the resonator with a concave folding mirror* M_F*; this introduces aberrations. The use of a flat folding mirror leads to a nonaberrated resonator.*

6.2 Experiment

6.2.1 Setup

In Fig. 6.1 we sketch the experimental setup. At its heart is a folded optical resonator, formed by three high-reflectivity mirrors. The two mirrors M_1 and M_2 (with a reflectivity $\mathscr{R} \sim 0.9999$) serve as cavity end mirrors, while the third mirror M_F (with reflectivity $\mathscr{R} \sim 0.99995$) folds the cavity through a total angle of 2α. If this folding mirror is *curved*, it will, because of the non-normal incidence of light, introduce significant nonparaxial effects. For $\alpha \geq 20^\circ$ these aberrations (relative to the paraxial case) are sufficient to generate wave-chaotic behaviour, as demonstrated in chapter 5. The two end mirrors can be either flat or curved, provided the overall resonator is stable in the sense that paraxial rays remain confined close to the optical axis of the system. The length of the resonator can be changed on a sub-wavelength scale, using a piezo element, as well as on a larger scale. The entire resonator is enclosed in a simple box to exclude airflows. No acoustic shielding is used.

To obtain transmission spectra of this system we inject light from a HeNe laser ($\lambda = 633$ nm), while scanning the resonator length. In front of the cavity, the HeNe beam is expanded by a telescope, to a diameter of typically 3.4 mm, and sent through a weak diffusor (typical FWHM scattering angle $\sim 0.5^\circ$); the resulting speckled input field excites about $N \sim 10^4$–10^5 transverse modes of the cavity[1] (also see section 5.2.2). Translating the diffusor transversely to the beam causes the speckle pattern to change drastically, thereby radically altering the excitation of the transverse mode manifold.

The finesse of the resonator was found to be[2] $\mathscr{F} \equiv \nu_\mathrm{FSR}/\delta\nu = 2\times10^3$–$5\times10^3$, where the free spectral range $\nu_\mathrm{FSR} \equiv t_\mathrm{round}^{-1} = c/2L$ (where t_round is the cavity round trip time), and

---

[1] This number of transverse modes may be estimated from the typical radius a of the light spot on the mirrors, $a \sim 0.5$–1 cm, the length of the resonator $L \sim 25$–35 cm, and the wavelength of the injected light λ through $N \sim a^4/\lambda^2 L^2 \sim 10^4$–$10^5$.

[2] This spread in the finesse is the result of the change in reflectivity of the folding mirror upon varying the folding angle of the resonator. In our experiments we used folding mirrors with coatings optimised for use at 0° and 45°, respectively. At angles of incidence other than the design angle, their reflectivity is lower.

$\delta\nu$ is the width of individual resonances. We see that $N > \mathscr{F}$, or that the width of individual modes is larger than the average mode spacing. As a result, transmission spectra for this system are largely filled, with many modes overlapping.

6.2.2 Method of analysis: general

With such largely filled transmission spectra, it is only possible to accurately detect the position of relatively few isolated resonances; the large majority cannot be analysed individually. Therefore, techniques that rely on analysis of isolated resonances, such as direct spectral statistics in the form of nearest neighbour distributions and related quantities, cannot be used to determine the nature of the dynamics in the system.

Instead, we turn to an analysis technique that was developed around 1985 [65, 57, 58] and got its final form a few years later [56]. It was specifically developed to deal with complex, dense spectra, such as occur in atomic and molecular systems. Its key ingredient is the *wave packet survival probability* $P(t)$, a measure for the temporal evolution of an arbitrary initial wave packet or state. For a lossless system, where all resonances are infinitely narrow and the spectrum consists of δ-spikes, $P(t)$ is directly related to both the normalised wave function $\psi(t)$ and to the Fourier transform of the normalised spectrum $S(\omega)$ corresponding to the initial wave packet $\psi(0)$, through

$$P(t) \equiv |\langle\psi(0)|\psi(t)\rangle|^2 = \left|\int S(\omega)\mathrm{e}^{-i\omega t}\mathrm{d}\omega\right|^2, P(0) = 1. \tag{6.1}$$

In essence, $P(t)$ is equivalent to the Fourier transform of the spectral autocorrelation function

$$\mathscr{A}(\Delta\omega) = \int S(\omega)S(\omega+\Delta\omega)\mathrm{d}\omega\,. \tag{6.2}$$

As a next step, $P(t)$ is averaged twice, over both initial wave functions and different realisations of the system, yielding $\langle\langle P(t)\rangle\rangle$. On mathematical grounds Wilkie and Brumer [56] have shown that this quantity has very different behaviour for regular or chaotic systems. For a chaotic system, $\langle\langle P(t)\rangle\rangle$ *must* fall below its long time asymptotic value $\langle\langle P(\infty)\rangle\rangle$ for some times t, while, for a regular system, $\langle\langle P(t)\rangle\rangle$ *cannot* fall below $\langle\langle P(\infty)\rangle\rangle$:

$$\forall t: \ \langle\langle P(t)\rangle\rangle \geq \langle\langle P(\infty)\rangle\rangle \text{ for regular dynamics,} \tag{6.3a}$$

$$\exists t: \ \langle\langle P(t)\rangle\rangle < \langle\langle P(\infty)\rangle\rangle \text{ for chaotic dynamics.} \tag{6.3b}$$

Therefore, the behaviour of $\langle\langle P(t)\rangle\rangle$ allows us to unambiguously distinguish between regular and chaotic dynamics. The asymptotic behaviour of $\langle\langle P(t)\rangle\rangle$ is directly related to the number of resonances N in the interval under consideration,

$$\langle\langle P(\infty)\rangle\rangle = \frac{2}{N+1}\,. \tag{6.4}$$

The region where, for chaotic dynamics, $\langle\langle P(t)\rangle\rangle$ falls below its asymptotic value $\langle\langle P(\infty)\rangle\rangle$ is commonly identified as the *correlation hole*. It is present not only for systems with fully developed chaos, but also for systems that have mixed chaotic and regular dynamics [59], and is generally located at small times t. Numerical studies indicate that the depth of the correlation hole is directly related to long-range spectral correlations (spectral rigidity), whereas its area depends on short-range correlations [59, 60]. Wilkie and Brumer [56] have shown that there is a direct relation between, on the one hand, $\langle\langle P(t)\rangle\rangle$, and hence the size and shape of the correlation hole, and, on the other hand, the cosine transforms of all n-th nearest neighbour spacing distributions $P_n(s)$. However, a direct physical interpretation of this correlation hole is as yet unavailable.

When applying this method to actual experiments, matters are complicated somewhat by the fact that in practice one rarely deals with lossless systems and ideal δ-spectra. Instead, one has to account for the finite line width of experimentally obtained spectra. Wilkie and Brumer [56] have shown that, with some reasonable assumptions, one can transform the wave packet survival probability for a lossy system $P_{\text{exp}}(t)$, as obtained directly from applying Eq. (6.1) to an experimental spectrum,

$$P_{\text{exp}}(t) = \left| \int S_{\text{exp}}(\omega) \mathrm{e}^{-i\omega t} \mathrm{d}\omega \right|^2 , \tag{6.5}$$

to the $P(t)$ of the underlying lossless system.

The argument is as follows: one assumes that each individual transmission spectrum can be viewed as the convolution of an ideal spectrum consisting of δ-shaped peaks, and a basic and known line shape $\ell(\omega)$. In the Fourier domain, this convolution reduces to a simple multiplication of the Fourier transform of the δ-spectrum, $P(t)$, and that of the fundamental line shape, $\mathscr{L}(t)$. Provided that $\ell(\omega)$ is the same for all realisations, the decay-free $\langle\langle P(t)\rangle\rangle$ is then related to the experimentally obtained $\langle\langle P_{\text{exp}}(t)\rangle\rangle$ through

$$\langle\langle P(t)\rangle\rangle = \frac{\langle\langle P_{\text{exp}}(t)\rangle\rangle}{|\mathscr{L}(t)|^2} . \tag{6.6}$$

This assumption on the structure of eigenspectra is valid for systems with a global loss mechanism that affects all eigenmodes equally.

Because this assumption allows one to obtain $P(t)$ directly from experimental spectra, without the need for peak finding or similar preprocessing techniques, methods relying on $P(t)$ are very robust. For badly resolved and complicated spectra, with many overlapping peaks, it has been found that these methods outperform direct frequency-domain methods, such as those centred around spectral rigidity or level repulsion [57, 58]. As $P(t)$ is the Fourier transform of the spectral autocorrelation function, one could, in principle, also use the doubly-averaged autocorrelation function to distinguish between regular and chaotic dynamics. However, for badly resolved spectra $\langle\langle P(t)\rangle\rangle$ is again superior to the alternative [57, 58].

6.2.3 Method of analysis: our case

We address now the two types of averaging introduced by Wilkie and Brumer in the context of our experimental setup. The first averaging refers to different realisations of the same system. In our system, this can be achieved most easily by changing the length of the resonator in steps δL much larger than the wavelength λ. These length changes lead to differently structured eigenfrequency spectra, but, since the angle of incidence of light on the folding mirror $\mathrm{M_F}$ is unchanged, these spectra correspond to different realisations of essentially the *same* system. In section 6.3.2 we will show that the use of on the order of 50 different resonator lengths leads to sufficient averaging.

The second averaging is done over initial wave functions. In our case, this role is played by the speckled injection field and the way it excites transverse modes of the cavity; therefore, averaging over initial conditions can be performed by changing the incident field and obtaining transmission spectra for different situations. The easiest way to implement this is to vary the transverse position of the diffusor. This will change the exact configuration of speckles in the input field impinging on the resonator, and will therefore give rise to different couplings to the individual intracavity modes. In section 6.3.3 we show that, in our setup, the use of 10 different transverse positions of the diffusor gives enough averaging.

As dissipation, dominantly due to the finite reflectivity of our mirrors, is impossible to avoid, all resonances have a finite width. To enable the diagnostic use of Eq. (6.3) we have to transform the experimentally obtained $\langle\langle P_{\text{exp}}(t)\rangle\rangle$ to the lossless $\langle\langle P(t)\rangle\rangle$ using Eq. (6.5). We assume that the resonances of our folded, chaotic resonator retain the Lorentzian line shape generally found for Fabry-Pérot interferometers,

$$\ell(\omega) = \frac{2}{\pi}\frac{1}{\delta\omega}\left\{1+4\left(\frac{\omega}{\delta\omega}\right)^2\right\}^{-1}, \tag{6.7}$$

where $\delta\omega$ is the full line width at half maximum. The Fourier transform of this fundamental line shape is given by

$$\mathscr{L}(t) = \exp\left(-\frac{\delta\omega}{2}|t|\right) = \exp\left(-\frac{\pi}{\mathscr{F}}\left|\frac{t}{t_{\text{round}}}\right|\right), \tag{6.8}$$

where we have used that the finesse $\mathscr{F} = \nu_{\text{FSR}}/\delta\nu = 2\pi/\delta\omega\, t_{\text{round}}$. Combining this with Eq. (6.5), we obtain the desired "decay-free" $\langle\langle P(t)\rangle\rangle$ from the experimentally determined $\langle\langle P_{\text{exp}}(t)\rangle\rangle$ through

$$\langle\langle P(t)\rangle\rangle = \langle\langle P_{\text{exp}}(t)\rangle\rangle/\exp\left(-\frac{2\pi}{\mathscr{F}}\left|\frac{t}{t_{\text{round}}}\right|\right), \tag{6.9}$$

where $\mathscr{F}$ can either be measured independently (by exciting only one, or at most a few, paraxial resonances and directly measuring the line width), or be estimated from $\langle\langle P_{\text{exp}}(t)\rangle\rangle$. This last method is only feasible if the asymptotic behaviour of $\langle\langle P_{\text{exp}}(t)\rangle\rangle$ can be recognised reliably (which is usually the case). Experimental results on the actual line shape, as well as a comparison between the two methods, will be reported in section 6.3.4.

6.3 Experimental validation

In this section we experimentally validate a number of techniques and procedures that we use to implement the Wilkie-Brumer method.

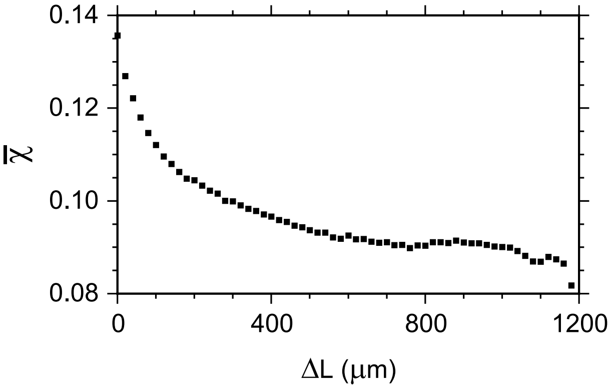

Figure 6.2: *Average of the maximum value of the cross-correlation for pairs of transmission spectra obtained for different cavity lengths, versus the difference in cavity length ($2\alpha = 90°$).*

6.3.1 Transmission spectra

For optical resonators, the most obvious, and intuitively cleanest, approach to obtain eigenfrequency spectra is to keep the length L of a resonator fixed, and scan the wavelength λ of the injection laser, while measuring the transmission through the resonator ("λ-scan"). However, since all eigenfrequencies depend on L, it is also possible to get information on these resonances by keeping λ fixed, and instead scan L over a limited range ("L-scan"). This will change the eigenfrequencies of the cavity, bringing them, one by one, into resonance with the laser frequency.

For paraxial, nonchaotic resonators the L-scan "spectrum" is, in general, identical to the proper eigenfrequency spectrum, as long as the scan range (of order $\lambda/2$) is much smaller than the resonator length[1]. The L-scan spectrum of a resonator is then quasiperiodic, with a period of $\lambda/2$, equivalent to a periodicity of $\Delta\nu = \nu_{\mathrm{FSR}}$ in the frequency domain. It is not, however, *a priori* clear whether the same is true for a nonparaxial, chaotic resonator.

To investigate this issue, we check whether L-scan spectra are indeed quasiperiodic. To this end, we cross-correlate L-scan transmission spectra obtained for different resonator lengths. If spectra, obtained for two cavity lengths that differ by $p \cdot \lambda/2$ (where p is a small integer), have (near) perfect correlation, we may conclude that the dependence of the eigenfrequency spectrum on L is small enough that the results for λ- and L-scan are the same.

We calculate the maximum value $\overline{\chi}$ of the normalised cross-correlation of pairs of spectra (with the DC value of the spectra removed), obtained for an ensemble of resonator lengths. The two spectra may correspond to the same resonator length, or may be obtained for different resonator lengths. These values $\overline{\chi}$ are plotted against the difference in cavity length ΔL in Fig. 6.2 (where $2\alpha = 90°$). Because of fluctuations in spectra due to external perturbations, even for identical resonator lengths the maximum cross-correlation is smaller than 1; if no external perturbations were present, $\overline{\chi}$ for $\Delta L = 0$ would be identical to 1. These external perturbations have (at least) two sources; the first of these is acoustic noise, mainly coupling into the longitudinal dimension of the cavity and causing a stretching and compressing of the spectra. The second is additive noise from the photomultiplier tube, adding an amplitude ripple to the signal.

---

[1] Exceptions to this are, for example, resonators at the edge of stability (close to concentric), or degenerate resonators with many excited modes.

We see that the maximum cross-correlation decays smoothly from its peak value for $\Delta L = 0$. From this smooth curve we can, for $\Delta L = 2\lambda \approx 1.27\ \mu$m, estimate that $\overline{\chi}_{\Delta L}/\overline{\chi}_0 \approx 0.97$ (or, for $\Delta L = \lambda/2$, $\overline{\chi}_{\Delta L}/\overline{\chi}_0 \approx 0.99$), which shows that these spectra are indeed (almost) identical, at least in statistical sense. Therefore, measuring transmission spectra by varying the *length* of the resonator, which need only be done over $\lambda/2$ (i.e., less than 2λ) to get a complete spectrum, yields spectra that are identical to those obtained through varying the *wavelength* of the injected light.

6.3.2 Averaging over realisations

Averaging over different realisations can be achieved by recording transmission spectra for different resonator lengths L. To determine the minimum length difference ΔL above which spectra become “dissimilar”, we use the same technique as used in the previous subsection to confirm short-range quasiperiodicity. This tells us how large we should choose our length steps δL for our averaging over realisations, to maximise the efficiency of our measurements.

From Fig. 6.2 we immediately see that $\overline{\chi}$ does not decay to 0, but instead levels off at a finite floor, determined by the residual spurious cross-correlations between nominally unrelated spectra. This floor is reached for $\Delta L > 700\ \mu$m. Therefore, choosing a step length $\delta L > 700\ \mu$m will be most efficient at extracting information on the dynamics from the system.

Choosing smaller steps will, because of the finite correlation between spectra, lead to unnecessary duplications: step lengths $\delta L < 700\ \mu$m will lead to averaging over an effectively lower number of *different* realisations, as demonstrated in Fig. 6.3. There we plot $\langle\langle P(t)\rangle\rangle$ for two different step lengths, $\delta L = 20\ \mu$m and $\delta L = 1$ mm. We see that the curve for the shorter step length contains additional structure, especially for lower t/t_{round}. This structure is specific for that particular (average) cavity length; experimentally we found that choosing a different cavity length leads to a different structure. This structure is the result of insufficient averaging, and does not contribute any information on the global nature of the dynamics. In contrast, the curve for $\delta L = 1$ mm, spanning a total resonator length interval of 5 cm, has no other features than the correlation hole for small t/t_{round}.

These results are not critically sensitive to the total number of realisations; this is illustrated by Fig. 6.4, where we plot two $\langle\langle P(t)\rangle\rangle$-curves stemming from the same dataset. One curve was calculated from the full dataset (40 distinct resonator lengths), the other by discarding every second resonator length (20 distinct resonator lengths), yielding an effective step length $\delta L = 2$ mm, while still spanning the same total length interval of 4 cm. We can see that the difference between the two curves is negligible. Therefore, we conclude that measuring over a total resonator length change $\Delta L \geq 4$ cm, containing about 60 different effective realisations, leads to sufficient averaging.

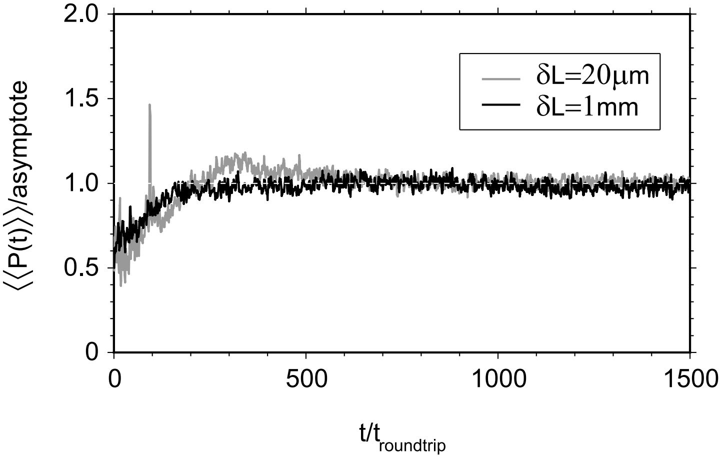

Figure 6.3: $\langle\langle P(t)\rangle\rangle$ *versus* $t/t_{roundtrip}$ *for two different resonator step lengths,* $\delta L =$ 20 μm *and* 1 mm. *The total number of measurements for the two curves is 50 and 40, respectively (*$2\alpha = 90°$*).*

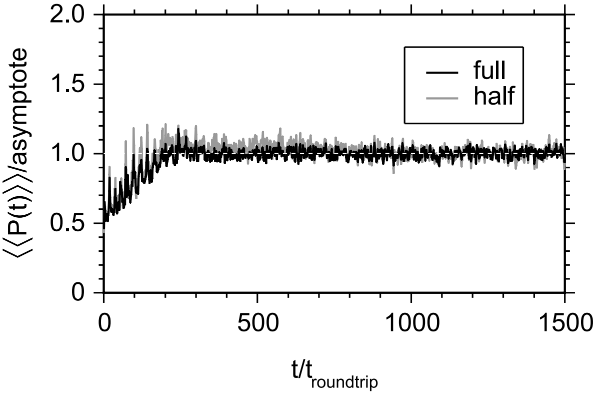

Figure 6.4: $\langle\langle P(t)\rangle\rangle$ *versus* $t/t_{roundtrip}$ *for a full set of 40 resonator lengths (black curve), and when every second resonator length is discarded, leading to 20 resonator lengths (grey curve). Also indicated is the level of the asymptote (*$2\alpha = 90°$*).*

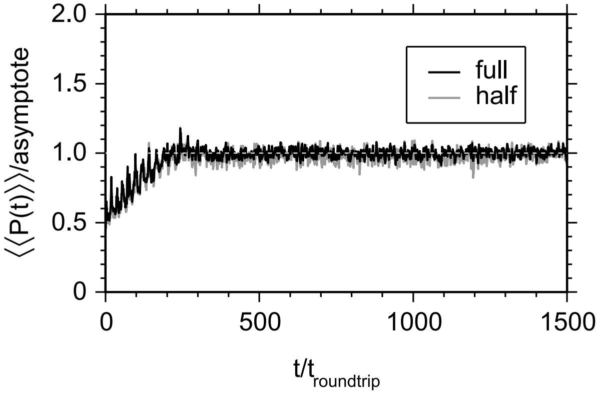

Figure 6.5: $\langle\langle P(t)\rangle\rangle$ *versus* $t/t_{roundtrip}$ *for 10 diffusor positions (black curve), and for 5 diffusor positions (grey curve);* $2\alpha = 90°$ *for both. The difference between these two curves is very slight. Also indicated is the level of the asymptote.*

6.3.3 Averaging over initial conditions

The second type of averaging needed in the analysis procedure is over initial conditions. As mentioned above, this can be achieved by translating the diffusor transversely to the injection beam. Cross-correlating pairs of spectra for different diffusor positions shows that translating the diffusor by 1 mm causes changes in the speckled field impinging on mirror M_1 of the resonator that are large enough to result in completely uncorrelated transmission spectra. In practice, we find that 10 different diffusor positions give sufficient averaging, in that halving the number of diffusor positions, while keeping all other parameters unchanged, does not affect the general shape of the resulting $\langle\langle P(t)\rangle\rangle$-curve, see Fig. 6.5. The only observable difference is in the width of the noise band; this is a direct consequence of changing the total number of measurements.

6.3.4 Line shape

With regard to the basic line shape of the resonances, in the experiment we must satisfy two contradictory requirements. On the one hand, the length of the resonator should ideally be scanned at a rate small enough so that the time to scan through a single resonance is larger than the cavity lifetime. If the scan rate is too high, resonances will lose their Lorentzian shape and generally broaden [71], severely complicating the analysis as discussed below. On the other hand, to minimise the effects of acoustic noise it is beneficial to scan at the highest possible rate. Scanning at a lower rate will degrade the quality of the spectra, again leading to difficulties in the analysis.

To assess the basic line shape we remove the diffusor and couple a thin pencil beam into the resonator, thereby exciting only a few, low order modes. Spectrally, these modes are spaced sufficiently far apart that we can study them individually. In Fig. 6.6a we plot the shape of a typical low order mode, together with the best Lorentzian fit. We see that the deviation from the ideal Lorentzian line shape is considerable, a direct consequence of

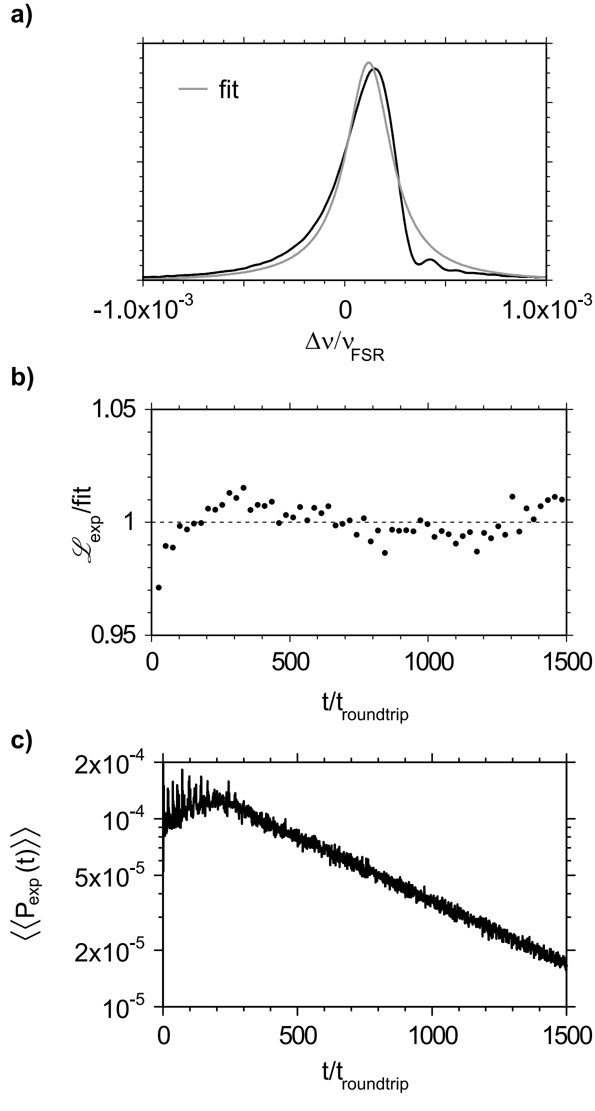

Figure 6.6: *(a) Detailed view of a single, low-order resonance of a chaotic resonator ($2\alpha = 90^\circ$), together with the best Lorentzian fit. (b) Fourier transform of a single low-order resonance, averaged over 20 measurements, divided by a fitted exponential. (c) Typical $\langle\langle P_{exp}(t)\rangle\rangle$-curve, where the asymptote, multiplied by a decaying exponential, is clearly visible.*

the cavity-length scan rate being too high. The length of the cavity was changed at a rate of $\lambda/83.8 \times 10^{-3} = 7.55 \times 10^{-6}$ m/s, so that the FWHM-time it takes to scan through a (deformed) resonance is $\tau \sim 1.25 \times 10^{-5}$ s. The cavity decay time is estimated to be of the order of $\tau_c \sim 3 \times 10^{-6}$ s; exact determination of the cavity decay time is not straightforward, and would involve curve-fitting the exact line shape to expressions from ref. [71]. Lowering the scan rate is not possible, as then the influence of acoustic noise becomes unacceptably large. As such, the chosen scan rate represents, for our current setup, a best-case tradeoff between minimising the effects of non-Lorentzian line shapes and the effect of acoustic noise.

More important than the actual line shape is the square of the modulus of the Fourier transform of that line shape, since that is the curve we want to divide out (see Eq. (6.6)). In the Fourier domain, the deviations between the average of transforms of many individual low-order lines and an exponential function remain below 3% over the entire relevant range, as can be seen in Fig. 6.6b, where we plot the ratio of the averaged Fourier transform and an exponential fit. From this exponential fit we can get an accurate estimate of the effective finesse of the low-order modes in our resonator.

Therefore, it is reasonable to treat the Fourier transform of the basic line shape as an exponential function. This exponential factor shows up prominently in experimentally obtained curves for $\langle\langle P_{\text{exp}}(t)\rangle\rangle$, see Fig. 6.6c, confirming our assumption that each individual transmission spectrum may be viewed as the convolution of an ideal δ-spectrum and a Lorentzian. This prominent exponential factor allows us to accurately estimate the (average) finesse $\mathscr{F}$ of the modes that are excited inside our resonator. In general, it is lower than the finesse for the low-order modes (for example, where the low-order finesse is ~ 5000, the average finesse of all excited modes $\mathscr{F} \sim 3800$), indicating that the higher order modes experience additional loss. For reasons of mode matching it is not possible to measure the finesse of higher order modes independently, so that we can only measure isolated resonances for low order modes, of which there are relatively few.

6.3.5 Postselection of spectra

Part of the procedure to go from experimental transmission spectra to $\langle\langle P(t)\rangle\rangle$ is a postselection of realisations, as mentioned at the end of section 5.2.3. This serves to suppress sharp, isolated spikes on $\langle\langle P(t)\rangle\rangle$ that can detract attention from the global nature of $\langle\langle P(t)\rangle\rangle$. That is not to say those spikes are without meaning or interest, but the information they carry is not needed to determine the type of dynamics in a system. Similar postselection procedures are customary in other experiments on wave chaos [48, 68, 69].

These sharp, isolated spikes occur in first instance on $P(t)$; they stem from strong, highly periodic components in transmission spectra that, for as yet unknown reasons, show up for particular realisations of a folded resonator. These spikes lead, after performing the double averaging, to peaks on $\langle\langle P(t)\rangle\rangle$ that reach a height that exceeds the level of the asymptote by up to a factor of 10.

Fortunately, realisations with such strong Fourier components are, in general, relatively rare and isolated, and it is possible to suppress these realisations without affecting the global shape of our curves. We average $P_{\text{exp}}(t)$-curves over incoupling conditions to obtain $\langle P_{\text{exp}}(t)\rangle$-curves (and hence $\langle P(t)\rangle$), one for every realisation. In these curves, we can determine the strength of the principal Fourier component, and we plot these strengths against the index

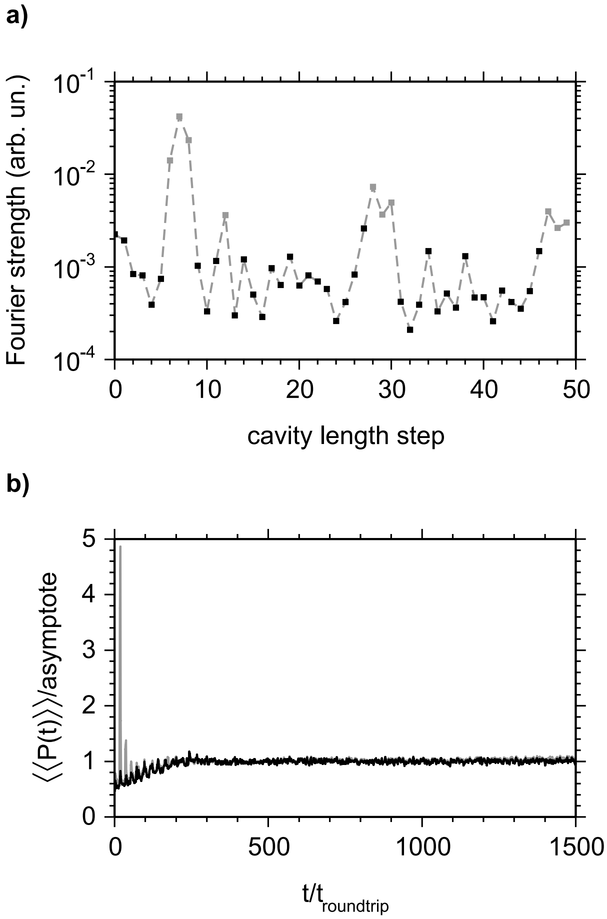

Figure 6.7: *(a) Strength of the principal Fourier component, as determined from* $\langle P(t)\rangle$*, for 50 realisations of a resonator with* $2\alpha = 90°$*. Indicated in grey are the 10 realisations that are not taken into account for the second averaging step. The dashed grey curve is a guide to the eye. (b)* $\langle\langle P(t)\rangle\rangle$ *corresponding to the same data set. Grey curve: Full data set of 50 realisations (500 spectra). Black curve: Partial data set of 40 realisations (400 spectra).*

number for each realisation. By way of example, in Fig. 6.7a we plot the results for a resonator with $2\alpha = 90°$. Based on these data we reject, of a full set of 50, the 10 realisations with the strongest principal Fourier components, and average the remaining 40 to obtain, ultimately, $\langle\langle P(t)\rangle\rangle$. In Fig. 6.7b we plot two curves $\langle\langle P(t)\rangle\rangle$, one for a full set of 50 realisations, the other for the subset of 40 realisations selected in this way. Clearly, the sharp spikes on $\langle\langle P(t)\rangle\rangle$ have disappeared almost completely, *without* affecting the overall shape of $\langle\langle P(t)\rangle\rangle$.

As the global shape of $\langle\langle P(t)\rangle\rangle$, and more importantly that of the correlation hole, is not affected by the postselection, this procedure does not influence our conclusions regarding the nature and general trend of the dynamics in our system.

6.4 Concluding discussion

Here we first summarise our results. Transmission spectra, obtained by scanning the length of the resonator and recording transmitted intensity, give direct information on the (fixed length) eigenfrequency spectrum of such systems, and can be used to analyse these systems. Two types of averaging, over different realisations and over initial conditions, can be achieved by changing the length of the resonator and by changing the transverse position of the incoupling diffusor, respectively. The shape of individual resonances is distinctly non-Lorentzian; this is a direct result of a cavity length scan rate that is higher than allowed by the cavity lifetime. Nevertheless, losses in the system can be accounted for by dividing out an exponential factor in $\langle\langle P_{\mathrm{exp}}(t)\rangle\rangle$, where the coefficient can be estimated accurately from $\langle\langle P_{\mathrm{exp}}(t)\rangle\rangle$. And finally, we are allowed to perform a postselection on our data to reject spurious spikes, without adversely affecting the predictive nature of the method or introducing anomalies.

Both in section 6.3.2 and in section 6.3.4, complications due to acoustic noise are mentioned. Acoustic vibrations cause scan-to-scan fluctuations, so that spectra obtained for identical length and incoupling conditions are never perfectly the same; their signature is necessarily statistical rather than deterministic. Furthermore, these acoustic vibrations impose a lower bound on the rate at which the length of the resonator must be varied; as a result, the cavity scan is faster than allowed by the cavity decay time, leading to non-Lorentzian line shapes. Both these issues would benefit from better acoustic shielding; currently, we are working on a soundproof enclosure for the setup. This should decrease the effect of noise, and allow a lower scan rate so that a higher finesse can be reached; however, effective shielding of acoustic noise is not easily achieved [72]. The current mirrors should, in principle, allow a finesse $\mathscr{F} = 2 \times 10^4$ or better. That we only reach an effective finesse of 5000 is a limitation imposed by the too-high scan rate.

Because it does not affect the overall shape of the curves, the postselection method we employ does not influence predictions regarding the regular or chaotic nature of the dynamics in our system. Nevertheless, the sharp spikes that are rejected in this way represent interesting physics in their own right and warrant further study. Currently, an explanation regarding their origin is lacking, although evidence suggests they are associated with unstable periodic orbits or scars [70]. Future work will specifically target this.

The Wilkie-Brumer method is eminently suited for diagnostics of experiments on wave chaos in folded chaotic resonators. It is robust, and can be used in the presence of many overlapping modes. Direct comparison of this method with other techniques, such as nearest neighbour spacing statistics, will be very interesting, and will shed new light on the interpretation of the location, size and shape of the correlation hole. In the near future, we plan to increase our finesse so that $\mathscr{F} > N$, to enable this comparison.

As a final remark, even though it is not possible to resolve all resonances in our transmission spectra, and direct spectral statistics cannot be used, this overlap is not fatal. The Wilkie-Brumer method can partially compensate for this overlap by *averaging* over initial conditions and realisations of the system, and allows one to determine whether a system is chaotic or not. It cannot, however, give information on individual spacing distributions $P_n(s)$. This then, is the ultimate price one has to pay for system losses.

Bibliography

[1] D. Herriott, H. Kogelnik, and R. Kompfner, ‘Off-axis paths in spherical mirror interferometers’, Appl. Opt. **3**(4), pp. 523–526 (1964). 4, 21, 70, 76

[2] I. A. Ramsay and J. J. Degnan, ‘A ray analysis of optical resonators formed by two spherical mirrors’, Appl. Opt. **9**(2), pp. 385–398 (1970). 4, 12

[3] C. Palma, ‘Complex dynamics of a beam in a gaussian cavity’, Opt. Commun. **129**, pp. 120–133 (1996). 4

[4] M.-D. Wei, W.-F. Hsieh, and C. C. Sung, ‘Dynamics of an optical resonator determined by its iterative map of beam parameters’, Opt. Commun. **146**, pp. 201–207 (1998). 4

[5] L. M. Sánchez and A. A. Hnilo, ‘Optical cavities as iterative maps in the complex plane’, Opt. Commun. **166**, pp. 229–238 (1999). 4

[6] H.-H. Wu, C.-C. Sheu, T.-W. Chen, M.-D. Wei, and W.-F. Hsieh, ‘Observation of power drop and low threshold due to beam waist shrinkage around critical configurations in an end-pumped Nd:YVO$_4$ laser’, Opt. Commun. **165**, pp. 225–229 (1999). 4

[7] A. E. Siegman, *Lasers* (University Science Books, Sausalito, CA, 1986). 4, 6, 12, 15, 16, 18, 30, 31, 35, 43, 51, 65, 66, 68

[8] Y. F. Chen, T. M. Huang, K. H. Lin, C. F. Kao, C. L. Wang, and S. C. Wang, ‘Analysis of the effect of pump position on transverse modes in fiber-coupled laser-diode end pumped lasers’, Opt. Commun. **136**, pp. 399–404 (1997). 5

[9] L. A. Westling, M. G. Raymer, and J. J. Snyder, ‘Single-shot spectral measurements and mode correlations in a multimode pulsed dye laser’, J. Opt. Soc. Amer. B **1**(2), pp. 150–154 (1984). 9

[10] D. H. Auston, ‘Forced and spontaneous phase locking of the transverse modes of a He-Ne laser’, IEEE J. Quantum Electron. **4**, pp. 471–473 (1968). 12

[11] L. G. Gouy, ‘Sur une propriété nouvelle des ondes lumineuses’, Compt. Rend. Acad. Sci. Paris **110**, pp. 1251–1253 (1890). 14

[12] L. G. Gouy, ‘Sur la propagation anomale des ondes’, Ann. de Chim. et Phys. **24**, pp. 145–213 (1891). 14

[13] P. W. Milonni and J. H. Eberly, *Lasers* (Wiley-Interscience, New York, 1988). 15, 16

[14] J. T. Verdeyen, *Laser Electronics* (Prentice-Hall International, London, 1989). 15

[15] H.-J. Stöckmann, *Quantum Chaos: An Introduction* (Cambridge University Press, Cambridge, 1999). 28, 38, 49, 62, 63, 69, 78

[16] D. C. Hanna, ‘Astigmatic gaussian beams produced by axially asymmetric laser cavities’, IEEE J. Quantum Electron. **5**(10), pp. 483–488 (1969). 31

[17] K. An, B. A. Sones, C. Fang-Yen, R. R. Dasari, and M. S. Feld, ‘Optical bistability induced by mirror absorption: measurement of absorption coefficients at the sub-ppm level’, Opt. Lett. **22**(18), pp. 1433–1435 (1997). 35

[18] A. L. Schawlow and C. H. Townes, ‘Infrared and optical masers’, Phys. Rev. **112**(6), pp. 1940–1949 (1958). 38

[19] V. S. Letokhov, ‘Generation of light by a scattering medium with negative resonance absorption’, Sov. Phys.–JETP **26**(4), pp. 835–840 (1968). 38

[20] R. V. Ambartsumyan, N. G. Basov, P. G. Kryukov, and V. S. Letokhov, ‘Non-resonant feedback in lasers’, Prog. Quant. Elec. **1**(3), pp. 107–185 (1970). 38, 39, 57

[21] S. John and G. Pang, ‘Theory of lasing in a multiple-scattering medium’, Phys. Rev. A **54**(4), pp. 3642–3652 (1996). 38

[22] G. A. Berger, M. Kempe, and A. Z. Genack, ‘Dynamics of stimulated emission from random media’, Phys. Rev. E **56**(5), pp. 6118–6122 (1997). 38

[23] T. Sh. Misirpashaev and C. W. J. Beenakker, ‘Lasing threshold and mode competition in chaotic cavities’, Phys. Rev. A **57**(3), pp. 2041–2045 (1998). 38

[24] G. Hackenbroich, C. Viviescas, B. Elattari, and F. Haake, ‘Photocount statistics of chaotic lasers’, Phys. Rev. Lett. **86**(23), pp. 5262–5265 (2001). 38

[25] N. M. Lawandy, R. M. Balachandran, A. S. L. Gomes, and E. Sauvain, ‘Laser action in strongly scattering media’, Nature **368**, pp. 436–438 (1994). 38

[26] W. L. Sha, C.-H. Liu, and R. R. Alfano, ‘Spectral and temporal measurements of laser action of Rhodamine 640 dye in strongly scattering media’, Opt. Lett. **19**(23), pp. 1922–1924 (1994). 38

[27] D. S. Wiersma, M. P. van Albada, and A. Lagendijk, ‘Coherent backscattering of light from amplifying random media’, Phys. Rev. Lett. **75**(9), pp. 1739–1742 (1995). 38

[28] H. Cao, Y. G. Zhao, S. T. Ho, E. W. Seelig, Q. H. Wang, and R. P. H. Chang, ‘Random laser action in semiconductor powder’, Phys. Rev. Lett. **82**(11), pp. 2278–2281 (1999). 38

[29] H. Cao, J. Y. Xu, E. W. Seelig, and R. P. H. Chang, ‘Microlaser made of disordered media’, Appl. Phys. Lett. **76**(21), pp. 2997–2999 (2000). 38

[30] R. K. Thareja and A. Mitra, ‘Random laser action in ZnO’, Appl. Phys. B **71**(2), pp. 181–184 (2000). 38

[31] E. Samuel, ‘Paint the town red’, New Scientist **170**(2297), p. 23 (2001). 38, 39

[32] G. van Soest, M. Tomita, and A. Lagendijk, ‘Amplifying volume in scattering media’, Opt. Lett. **24**(5), pp. 306–308 (1999). 38, 39

[33] C. Gmachl, F. Capasso, E. E. Narimanov, J. U. Nöckel, A. D. Stone, J. Faist, D. L. Sivco, and A. Y. Cho, ‘High-power directional emission from microlasers with chaotic resonators’, Science **280**, pp. 1556–1564 (1998). 38, 62, 63

[34] G. Hackenbroich, C. Viviescas, and F. Haake, ‘Field quantization for chaotic resonators with overlapping modes’, Phys. Rev. Lett. **89**(8), 083902 (2002). 38

[35] M. Patra, ‘Theory for photon statistics of random lasers’, Phys. Rev. A **65**(4), 043809 (2002). 38

[36] K. M. Frahm, H. Schomerus, M. Patra, and C. W. J. Beenakker, ‘Large Petermann factor in chaotic cavities with many scattering channels’, Europhys. Lett. **49**(1), pp. 48–54 (2000). 38

[37] F. Haake, *Quantum Signatures of Chaos* (Springer Verlag, Berlin, 1991). 38, 62

[38] M. P. van Exter, G. Nienhuis, and J. P. Woerdman, ‘Two simple expressions for the spontaneous emission factor β’, Phys. Rev. A **54**(4), pp. 3553–3558 (1996). 51

[39] J. S. Hersch, M. R. Haggerty, and E. J. Heller, ‘Influence of diffraction on the spectrum and wave functions of an open system’, Phys. Rev. E **62**(4), pp. 4873–4888 (2000). 54, 55

[40] J. U. Nöckel and A. D. Stone, ‘Ray and wave chaos in asymmetric resonant optical cavities’, Nature **385**, pp. 45–47 (1997). 62, 63

[41] S. Chang, R. K. Chang, A. D. Stone, and J. U. Nöckel, ‘Observation of emission from chaotic lasing modes in deformed microspheres: displacement by the stable-orbit modes’, J. Opt. Soc. Amer. B **17**(11), pp. 1828–1834 (2000). 62, 63

[42] M. P. van Albada and A. Lagendijk, ‘Observation of weak localization of light in a random medium’, Phys. Rev. Lett. **55**(24), pp. 2692–2695 (1985). 62

[43] D. S. Wiersma, P. Bartolini, A. Lagendijk, and R. Righini, ‘Localization of light in a disordered medium’, Nature **390**, pp. 671–673 (1997). 62

[44] B. A. van Tiggelen, ‘Localization of waves’, in ‘Diffuse Waves in Complex Media’, (J.-P. Fouque, ed.), volume 531 of *NATO Science Series: C: Mathematical and Physical Sciences*, pp. 1–60 (Kluwer Academic Publisher, Dordrecht, 1999). 62

[45] G. van Soest, F. J. Poelwijk, R. Sprik, and A. Lagendijk, ‘Dynamics of a random laser above threshold’, Phys. Rev. Lett. **86**(8), pp. 1522–1524 (2001). 62

[46] H. Cao, Y. Ling, J. Y. Xu, and C. Q. Cao, ‘Photon statistics of random lasers with resonant feedback’, Phys. Rev. Lett. **86**(20), pp. 4524–4527 (2001). 62

[47] G. Zacharakis, N. A. Papadogiannis, G. Filippidis, and T. G. Papazoglou, ‘Photon statistics of laserlike emission from polymeric scattering gain media’, Opt. Lett. **25**(12), pp. 923–925 (2000). 62

[48] H.-D. Gräf, H. L. Harney, H. Lengeler, C. H. Lewenkopf, C. Rangacharyulu, A. Richter, P. Schardt, and H. A. Weidenmüller, ‘Distribution of eigenmodes in a superconducting stadium billiard with chaotic dynamics’, Phys. Rev. Lett. **69**(9), pp. 1296–1299 (1992). 62, 71, 88

[49] P. Pradhan and S. Sridhar, ‘Correlations due to localization in quantum eigenfunctions of disordered microwave cavities’, Phys. Rev. Lett. **85**(11), pp. 2360–2363 (2000). 62

[50] M. Berry, ‘Some quantum-to-classical asymptotics’, in ‘Chaos and quantum physics’, (M.-J. Giannoni, A. Voros, and J. Zinn-Justin, eds.), Les Houches Lecture Series LII, pp. 251–304 (North-Holland, Amsterdam, 1991). 62

[51] T. Prosen, ‘Localization in billiards’, in ‘New Directions in Quantum Chaos’, (G. Casati, I. Guarneri, and U. Smilansky, eds.), Proceedings of the International School of Physics “Enrico Fermi”, Course CXLIII, pp. 473–509 (IOS Press, Amsterdam, 2000). 62

[52] J. Dingjan, E. Altewischer, M. P. van Exter, and J. P. Woerdman, ‘Experimental observation of wave chaos in a conventional optical resonator’, Phys. Rev. Lett. **88**(6), 064101 (2002). 62, 73, 78

[53] E. E. Narimanov, G. Hackenbroich, P. Jacquod, and A. D. Stone, 'Semiclassical theory of the emission properties of wave-chaotic resonant cavities', Phys. Rev. Lett. **83**(24), pp. 4991–4994 (1999). 63

[54] P. B. Wilkinson, T. M. Fromhold, R. P. Taylor, and A. P. Micolich, 'Electromagnetic wave chaos in gradient refractive index optical cavities', Phys. Rev. Lett. **86**(24), pp. 5466–5469 (2001). 63

[55] A. Aiello *et al.*, in preparation. 64

[56] J. Wilkie and P. Brumer, 'Time-dependent manifestations of quantum chaos', Phys. Rev. Lett. **67**(10), pp. 1185–1188 (1991). 64, 69, 71, 78, 80, 81

[57] L. Leviandier, M. Lombardi, R. Jost, and J. P. Pique, 'Fourier transform: A tool to measure statistical level properties in very complex spectra', Phys. Rev. Lett. **56**(23), pp. 2449–2452 (1986). 64, 69, 70, 78, 80, 81

[58] J. P. Pique, Y. Chen, R. W. Field, and J. L. Kinsey, 'Chaos and dynamics on 0.5–300-ps time scales in vibrationally excited acetylene: Fourier transform of stimulated-emission pumping spectrum', Phys. Rev. Lett. **58**(5), pp. 475–478 (1987). 64, 69, 70, 78, 80, 81

[59] Y. Alhassid and N. Whelan, 'Onset of chaos and its signature in the spectral autocorrelation function', Phys. Rev. Lett. **70**(5), pp. 572–575 (1993). 64, 70, 80, 81

[60] J.-Z. Ma, 'Correlation hole of survival probability and level statistics', J. Phys. Soc. Japan **64**(11), pp. 4059–4063 (1995). 64, 70, 81

[61] L. E. Reichl, *The transition to chaos in conservative classical systems; quantum manifestations* (Springer Verlag, Berlin, 1992). 65

[62] M. Bass, E. W. Van Stryland, D. R. Williams, and W. L. Wolfe, eds., *Handbook of Optics*, volume I (McGraw-Hill, New York, 1995), second edition. 65, 66, 68

[63] M. Born and E. Wolf, *Principles of Optics* (Cambridge University Press, Cambridge, 1999). 65

[64] P. Pechukas, '"Quantum chaos" in the irregular spectrum', Chem. Phys. Lett. **86**(5, 6), pp. 553–557 (1982). 69, 78

[65] P. Pechukas, 'Remarks on "quantum chaos"', J. Phys. Chem. **88**, pp. 4823–4829 (1984). 69, 78, 80

[66] A. Kudrolli and S. Sridhar, 'Signatures of chaos in quantum billiards: Microwave experiments', Phys. Rev. E **49**(1), pp. R11–R14 (1994). 70

[67] J. Dingjan, M. P. van Exter, and J. P. Woerdman, 'Geometric modes in a single-frequency Nd:YVO$_4$ laser', Opt. Commun. **188**, pp. 345–351 (2001). 70

[68] W. Li, L. E. Reichl, and B. Wu, 'Quantum chaos in a ripple billiard', Phys. Rev. E **65**, 056220 (2002). 71, 88

[69] C. Dembowski, B. Dietz, H.-D. Gräf, A. Heine, T. Papenbrock, A. Richter, and C. Richter, 'Experimental test of a trace formula for a chaotic three-dimensional microwave cavity', Phys. Rev. Lett. **89**(6), 064101 (2002). 71, 88

[70] E. J. Heller, 'Bound-state eigenfunctions of classically chaotic Hamiltonian systems: Scars of periodic orbits', Phys. Rev. Lett. **53**(16), pp. 1515–1518 (1984). 76, 90

[71] M. J. Lawrence, B. Willke, M. E. Husman, E. K. Gustafson, and R. L. Byer, 'Dynamic response of a Fabry-Perot interferometer', J. Opt. Soc. Amer. B **16**(4), pp. 523–532 (1999). 86, 88

[72] T. Klaassen, private communication. 90

Samenvatting:

Multimode optische trilholtes en golfchaos

Dit proefschrift gaat, zoals u natuurlijk al uit bovenstaande titel heeft afgeleid, over optische trilholtes waarin meerdere eigentrillingen zijn aangeslagen, en over golfchaos. Maar wat betekent dat nu eigenlijk, *optische trilholte*, *eigentrilling* en *golfchaos*?

Net als ieder vakgebied heeft ook de natuurkunde zo haar eigen woordenschat en woordgebruik. Naast woorden die buiten de natuurkunde niet voorkomen, en die een niet-natuurkundige hoogstwaarschijnlijk niet zal kennen, zijn er ook veel woorden die lijken op, of zijn samengesteld uit, woorden die we ook in de wereld van alledag tegenkomen. Echter, binnen de natuurkunde is de betekenis van die woorden nauwer omschreven, soms subtiel anders, en in sommige gevallen haast tegengesteld.

Aangezien ik mijn proefschrift, en dus het werk dat ik de afgelopen jaren heb verricht, toegankelijk wil maken voor een zo breed mogelijk publiek, heb ik ervoor gekozen een *populair-wetenschappelijke* samenvatting te schrijven, waarin ik niet streef naar natuurkundige exactheid, maar naar leesbaarheid en begrijpelijkheid. Daartoe zal ik eerst enige begrippen introduceren en uitleggen.

Enige begrippen

Licht Licht is een elektromagnetisch golfverschijnsel, een trillend elektromagnetisch veld dat zich voortplant. U kunt dit vergelijken met een watergolf die zich voortplant aan een wateroppervlak. Net als zo'n watergolf heeft ook licht golfpieken en golfdalen. Elektromagnetische golven, of straling, wordt ingedeeld aan de hand van de *golflengte*, de afstand tussen twee opeenvolgende golfpieken. Voor licht ligt de golflengte grofweg tussen 1 mm (ver-infrarood) en 10 nm (ver-ultraviolet). Zichtbaar licht heeft een golflengte tussen 730 nm (rood) en 400 nm (violet), waarbij één nanometer overeenkomt met één miljoenste van een millimeter (ter vergelijking, menselijk hoofdhaar heeft een dikte tussen 40 μm en 130 μm, of tussen de 40 en 130 duizendste van een millimeter). Bij golflengtes langer dan 1 mm vinden we eerst microgolven (bekend uit de magnetron), en daarna radiogolven. Straling met een golflengte korter dan 10 nm duiden we aan met röntgenstraling of gammastraling. De golflengte is, via de lichtsnelheid, direct gerelateerd aan de *frequentie* van de straling, waarbij licht met een grotere golflengte een lagere frequentie heeft.

Stralenoptica In de stralenoptica verwaarlozen we, voor het gemak, het golfkarakter van licht, en beschrijven de voortplanting van licht aan de hand van oneindig dunne *lichtstralen*. Deze stralen planten zich in uniforme media langs rechte lijnen voort. Aan spiegelende oppervlakken worden deze stralen gereflecteerd, terwijl ze bij de overgang tussen twee verschillende media, bijvoorbeeld lucht en glas, *breking* vertonen. De stralen vertonen zowel bij reflectie als bij breking een scherpe knik. In veel situaties is de verwaarlozing van het golfkarakter van licht toelaatbaar, met name (maar zeker niet altijd) als de golflengte van het licht heel klein is ten opzichte van alle afmetingen van een systeem (aan bovengenoemde getallen kunt u zien dat, grofweg, de golflengte van zichtbaar licht één of twee honderdste van de dikte van een mensenhaar is).

Golfoptica In de golfoptica wordt wel expliciet rekening gehouden met het golfkarakter van licht. Hierdoor zijn effecten die buiten het bereik van de stralenoptica vallen, wel goed te beschrijven. Een van die effecten is buiging of *diffractie*. Deze diffractie kunnen we zien als de neiging van licht, of welk ander golfverschijnsel, om uit te waaieren. Een voorbeeld hiervan is de lichtbundel afkomstig uit een laserpen: vlak bij de pen is deze bundel grofweg 1 mm in diameter, terwijl ze op 10 m afstand al is gegroeid naar bijna 1 cm.

Een ander belangrijk effect in de golfoptica is *interferentie*, waarbij twee golven door elkaar lopen. Als de golfpieken en -dalen van de eerste golf samenvallen met de golfpieken en -dalen van de tweede golf, zullen deze elkaar versterken (constructieve interferentie). Als daarentegen de pieken van de eerste golf samenvallen met de dalen van de tweede golf, en vice versa, dan zullen de golven elkaar uitdoven (destructieve interferentie). Dit effect is gemakkelijk zichtbaar te maken met watergolven: als men in een vlakke vijver twee stenen gooit, een eindje uit elkaar, ziet men twee cirkelvormige, zich uitbreidende golfpatronen. In het overlapgebied van de twee golfpatronen ziet men dan lijnen waar het water, als gevolg van constructieve interferentie, woest op en neer beweegt, en lijnen waar het water, als gevolg van destructieve interferentie, nauwelijks golft.

Paraxiale benadering Binnen de paraxiale benadering nemen we aan dat de hoek tussen de as van een optisch systeem en de voortplantingsrichting van een lichtstraal of -golf, klein zijn. In dat geval mag men de sinus of tangens van een hoek vervangen door de hoek zelf (gerekend in radialen), $\sin\alpha \approx \tan\alpha \approx \alpha$. Dit zorgt voor een aanzienlijke vereenvoudiging van de wiskundige beschrijving van optische problemen. Veel vraagstukken die binnen de paraxiale benadering simpel op te lossen zijn, leiden tot aanzienlijke problemen *buiten* die benadering.

Laser De laser dankt zijn naam aan het acroniem voor *light amplification by stimulated emission of radiation*, lichtversterking door gestimuleerde emissie van straling. Terwijl een gloeilamp licht uitzendt in alle richtingen en over een breed kleurbereik, is het licht van een laser geconcentreerd in een nauwe bundel, en heel “zuiver” van kleur. Deze kleur kan variëren van (onzichtbaar) ver-infrarood, via het nabij-infrarood van de lasers in cd-spelers, het bekende rood van helium-neonlasers, laserpennen en kassa’s en het groen van lasershows, tot het (onzichtbare) ultraviolet en ver-ultraviolet zoals gebruikt wordt in chipfabricage.

Iedere laser bestaat uit twee basiselementen: een medium dat zorgt voor de versterking van licht, en een manier om een deel van het licht dat uit het lichtversterkend medium komt terug te voeren (terugkoppeling). Dit teruggekoppelde licht stimuleert het medium om identiek licht uit te zenden. In conventionele lasers wordt deze terugkoppeling van licht verzorgd door spiegels die een deel van het licht doorlaten, en een deel terugkaatsten. Deze spiegels sluiten het licht op in een zogenaamde *trilholte*.

Trilholte Een trilholte of resonator bestaat uit spiegels die zo zijn opgesteld dat zij licht kunnen opsluiten in een gesloten pad. Het simpelste voorbeeld is twee spiegels die recht tegenover elkaar staan: het licht dat gereflecteerd wordt door de eerste spiegel valt op de tweede spiegel, die het weer terugkaatst naar de eerste, enzovoort. Een trilholte hoeft dus niet volledig gesloten te zijn, om licht op te kunnen sluiten, maar dit mag natuurlijk wel. De in dit onderzoek gebruikte trilholtes zijn allemaal erg open, en bestaan uit niet meer dan twee of drie spiegels, in grootte variërend tussen minder dan een eurocent en een 2-euromunt.

In een trilholte is het van belang dat de golfpieken en -dalen na één rondgang samenvallen met de pieken en dalen van de oorspronkelijke golf, zodat constructieve interferentie optreedt. Als dit na één rondgang gebeurt, is dit natuurlijk ook zo na twee, drie, tien of honderd rondgangen. In dit geval spreken we van *resonantie*. Vallen de golfpieken na één rondgang niet samen met de pieken van de oorspronkelijke golf, maar met de *dalen*, dan zullen deze pieken en dalen elkaar uitdoven als gevolg van destructieve interferentie. Door dit proces kan alleen licht van heel welbepaalde golflengtes opgesloten worden in een trilholte. We noemen deze golflengtes *resonante golflengtes*, en de bijbehorende frequenties *resonantiefrequenties*. Veranderen we de lengte van de trilholte, door bijvoorbeeld de spiegels verder uit elkaar te zetten, dan zullen deze “passende” golflengtes en frequenties meeveranderen.

Eigentrilling Een eigentrilling van een trilholte of resonator is een elektromagnetisch golfpatroon dat zich na één rondgang door de trilholte exact herhaalt. Dit veronderstelt niet alleen een “passende” golflengte, zoals hierboven beschreven, maar ook een “passend” patroon dwars op de voortplantingsrichting van het licht. In een trilholte gemaakt van holle spiegels, die het licht bundelen, zijn meerdere dwarspatronen mogelijk waarbij de natuurlijke neiging tot uitwaaieren (diffractie) precies wordt gecompenseerd door de netto samenbundelende werking van de spiegels. Voorbeelden van zulke dwarsdoorsnedes van eigentrillingen zijn gegeven in Figuur 1. Het simpelste dwarspatroon, linksboven, is een cirkel die vloeiend afloopt naar de rand. Andere patronen hebben horizontale of verticale lijnen zonder licht, de witte lijnen in de figuur. De afmetingen

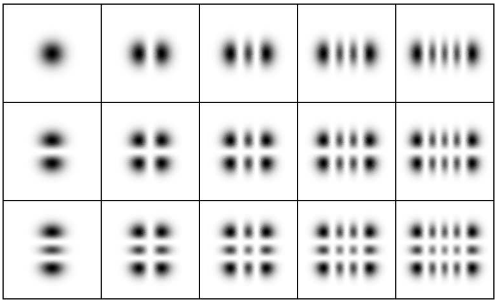

Figuur 1: *Enkele dwarspatronen van eigentrillingen van een trilholte.*

van deze figuren zijn in het algemeen veel groter dan de golflengte van het licht.

Mode Een andere naam voor deze eigentrillingen is *eigenmode* of simpelweg *mode*. Zoals weergegeven in Figuur 1 zijn er meerdere modes mogelijk in een trilholte, elk met hun eigen dwarspatroon. Indien in een trilholte ook daadwerkelijk licht aanwezig is in een van die profielen, noemen we die mode *aangeslagen* (vergelijk dit met het “aanslaan” van noten op een piano). In veel lasers is slechts één mode aangeslagen; de lichtbundel die uit zo’n laser komt heeft dan dezelfde dwarsdoorsnede als deze mode. We noemen zulke systemen *single-mode*. Aangezien de modes in principe onafhankelijk zijn, kunnen ook meerdere modes tegelijkertijd aangeslagen zijn: zo’n systeem noemen we *multimode*.

Gouy-fase Al in 1890 vond Gouy dat licht dat samengebundeld, of gefocusseerd, wordt een verschuiving in de positie van de golfpieken en -dalen laat zien die afhangt van hoe sterk het licht gebundeld wordt. Deze verschuiving kan worden uitgedrukt in een *faseverschil*. De fase van een golf is niets anders dan een manier om aan te geven in welk deel van de golf we ons bevinden. Vergelijk dit met de fasen van de maan: nieuwe maan, eerste kwartier (wassende maan), volle maan en laatste kwartier (krimpende maan). Als de fase van een golf verandert, verschuift dus de positie van de golfpieken en -dalen (ten opzichte van, bijvoorbeeld, een referentiegolf).

Het faseverschil als gevolg van de bundeling van licht wordt Gouy-fase genoemd. Deze Gouy-fase ontwikkelt zich geleidelijk in het gebied rond de nauwste bundeling van het licht, het focus. Hierdoor zal de totale Gouy-fase die licht ondervindt bij één rondgang door een trilholte afhangen van de manier waarop licht in die trilholte samengebundeld wordt, en dus van de afstand tussen, en de kromming van, de spiegels die de trilholte vormen. Daarnaast is ook het dwarspatroon van een eigentrilling van belang: hoe gecompliceerder dat dwarspatroon, hoe groter de Gouy-fase na één rondgang. Aangezien de Gouy-fase zorgt voor een verschuiving van de golfpieken en -dalen, en deze pieken en dalen voor resonantie moeten samenvallen met de pieken en dalen van één rondgang eerder, bepaalt de Gouy-fase heel direct de resonantiefrequenties van elke mode. Omdat de Gouy-fase wordt bepaald door de afstand tussen, en de kromming van, de spiegels van de trilholte, kunnen we deze makkelijk beïnvloeden.

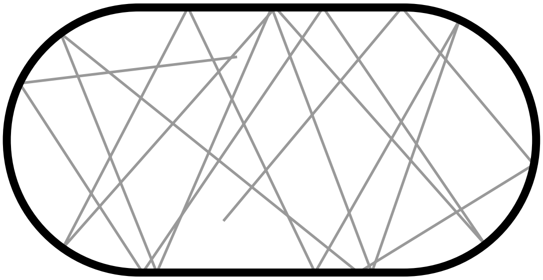

Figuur 2: *Stadion-vormig biljart met daarin het traject van een biljartbal.*

Chaos In tegenstelling tot in het dagelijks taalgebruik duidt chaos in de natuurkunde niet op volledige willekeur. Integendeel, de term (klassieke) chaos is voorbehouden aan systemen die zich ontwikkelen volgens welomschreven regels (deterministisch), zonder enige willekeur, maar waarvoor het desondanks niet mogelijk is “de toekomst” te voorspellen. Dit komt doordat zelfs oneindig kleine veranderingen in de begintoestand razendsnel groeien, en aanleiding geven tot radicaal ander gedrag. Een veelgebruikt voorbeeld van een klassiek chaotisch systeem is het weer op aarde. In 1972 illustreerde Edward Lorenz de extreme gevoeligheid van chaotische systemen met zijn welbekende vlinder: een vleugelslag van deze vlinder in het regenwoud in Brazilië kan een tornado boven Texas veroorzaken. De *Quantum Weather Butterfly* die de kaft van mijn proefschrift siert is een verdere evolutie van de vlinder van Lorenz.

Een heel simpel voorbeeld van een klassiek chaotisch systeem is een biljart dat niet rechthoekig is, maar is voorzien van ronde uiteinden, een zogenoemd *stadion-biljart*, zoals geschetst in Figuur 2. In zo’n biljart hangt het traject van een biljartbal extreem gevoelig af van de exacte positie van de bal, of de richting waarin ze gespeeld wordt; een kleine verandering in plaats of richting leidt tot een volledig andere weg.

Golfchaos Als we in een klassiek chaotisch systeem de (licht-)stralen of deeltjes (de biljartballen) vervangen door *golven*, krijgen we een *golfchaotisch* systeem. Doordat we nu werken met golven, gaat de bovenstaande beschrijving van de razendsnelle groei van oneindig kleine veranderingen niet meer op. De gevolgen van golfchaos zijn vooral te merken in de statistische verdeling van de resonantiefrequenties van het systeem. Voor een golfchaotisch systeem is de kans dat twee resonantiefrequenties heel dicht bij elkaar liggen, verwaarloosbaar klein. Voor een niet-golfchaotisch systeem is deze kans juist relatief groot.

Samenvatting van het proefschrift

Zoals al genoemd in de inleiding van dit hoofdstuk, gaat dit proefschrift over optische trilholtes waarin meerdere eigentrillingen zijn aangeslagen, en over golfchaos. De motivatie van dit onderzoek komt van de kant van de *random laser*: een laser die niet is gebaseerd op een simpele trilholte, met eenvoudig te berekenen eigentrillingen, maar juist op een *chaotisch systeem*. Dit systeem kan een suspensie van heel kleine deeltjes zijn, waaraan licht verstrooid wordt (vergelijk dit met de verstrooiing van licht aan stof in de lucht), of een trilholte die door zijn vorm golfchaotisch is, zoals het stadionbiljart van Figuur 2.

Random lasers hebben eigenschappen die aanzienlijk afwijken van die van conventionele lasers. De fundamentele fysica interesseert zich met name in de veranderde ruiseigenschappen en dynamica van zulke lasers, en de combinatie van meervoudige verstrooiing van licht en kwantummechanica. Voor de toegepaste fysica ligt het belang van random lasers in de relatieve ongevoeligheid van deze lasers voor imperfecties, en de daaruit voortvloeiende potentieel lage prijs. Het onderzoek aan random lasers heeft bijvoorbeeld al geleid tot “laserverf” die, volgens de uitvinders, gebruikt kan worden voor zulke diverse toepassingen als anti-vervalsingssystemen, extreem zichtbare markeringen, noodverlichting en beeldschermen.

Alle tot nu toe daadwerkelijk gerealiseerde random lasers zijn gebaseerd op lichtverstrooiende deeltjes, in de vorm van een fijn poeder of een suspensie. Dit bemoeilijkt de beïnvloeding van de verdeling van de deeltjes, en maakt exacte herhaling van experimenten veelal onmogelijk. Ook leidt dit ertoe dat deze lasers niet constant “aan” kunnen zijn, maar slechts korte tijd achter elkaar kunnen werken. Omdat een groot deel van de theorie voor random lasers is ontwikkeld voor continu werkende systemen, is een nauwkeurige vergelijking van theorie en experimentele resultaten nog niet goed mogelijk. Om deze redenen wilden wij een werkende random laser bouwen gebaseerd op een *trilholte*, in plaats van lichtverstrooiende deeltjes. Dit heeft als grote voordelen dat de vorm van zo’n trilholte veel beter te sturen valt dan de verdeling van een poeder, en dat zo’n random laser continu kan werken.

Helaas is het in onze experimenten niet gelukt ook daadwerkelijk een random laser te bouwen. In eerste instantie hebben we gewerkt aan een kleine, zelfgebouwde laser. Van dit systeem kunnen we de geometrie nauwkeurig aanpassen. Omdat deze laser van energie wordt voorzien door een andere laser (de pomplaser), kunnen we ook de plaats en grootte van het gebied waar licht versterkt wordt beïnvloeden, door de bundel van de pomplaser op een andere plek te laten vallen. Dit onderzoek staat beschreven in hoofdstukken 2, 3 en 4. In een later stadium heeft ons onderzoek zich geconcentreerd op “lege” trilholtes, zonder lichtversterkend medium. In deze systemen, die vooral beschreven worden in hoofdstukken 5 en 6, hebben we de aanwezigheid van golfchaos aangetoond.

Hoofdstuk 2: Geometrische modes in een “single frequency” Nd:YVO_4-laser

In dit hoofdstuk beschrijven we het gedrag van een zelfgebouwde laser, waarin een Nd:YVO_4-kristal (spreek uit: neodymium-yttriumvanadaat) zorgt voor de versterking van licht. Het systeem is zo opgebouwd dat licht alleen *naast* de optische as van het systeem wordt versterkt, zoals geschetst in Figuur 2.1 op pagina 5. In het algemeen zal dit ervoor zorgen dat de laser licht uitzendt met een dwarsprofiel als in Figuur 2.2, waarbij de meest linkse donkere vlek samenvalt met het gebied waar licht versterkt wordt. U kunt dit figuur vergelijken met de bovenste rij in Figuur 1 op pagina 98.

Als we de afstand tussen de holle en de vlakke spiegel veranderen, zien we voor een welbepaalde afstand dat de laser in een compleet ander patroon licht uitzendt, namelijk zoals weergegeven in Figuur 2.3a–d. Subfiguur a toont het dwarsprofiel van de eigentrilling op de vlakke spiegel, subfiguur b het dwarsprofiel op de holle spiegel. In subfiguur d is de vorm van deze eigentrilling geschetst. We zien dat deze W-vormige mode veel beter overlapt met het lichtversterkende gebied, aangegeven met de pijl in Figuur 2.3d. We hebben deze mode een *geometrische mode* genoemd.

Deze W-vormige mode is het resultaat van samenwerking tussen een groot aantal eigentrillingen, elk met dwarsdoorsnedes vergelijkbaar met Figuur 2.2 of de bovenste rij in Figuur 1. Dit samenwerkingsverband is mogelijk omdat, bij deze speciale lengte van de trilholte, al deze eigentrillingen dezelfde golflengte hebben. Gezien vanuit de stralenoptica vormt precies bij deze lengte het W-vormige traject een gesloten pad. Na vier keer heen-en-weerkaatsen tussen de spiegels zijn we weer terug bij het beginpunt.

Ook bij andere afstanden tussen de holle en vlakke spiegel kan het vòòrkomen dat veel eigentrillingen dezelfde golflengte hebben. Ook dan zal de laser licht uitzenden in een geometrische mode, maar dan van een andere vorm.

Hoofdstuk 3: Optische resonatoren en de Gouy-fase

In dit hoofdstuk geven we een uitgebreidere uitleg bij de waarnemingen van hoofdstuk 2. We geven de theorie voor de eigenfrequenties van paraxiale trilholtes, en we speculeren over de gevolgen van niet-paraxialiteit.

Essentieel in de bepaling van de eigenfrequenties is de *Gouy-fase*. Deze Gouy-fase wordt bepaald door de afstand tussen en de vorm van de spiegels die de trilholte vormen, zeg maar de geometrie van de trilholte. Voor paraxiale trilholtes bestaande uit twee spiegels bepaalt deze Gouy-fase het frequentieverschil tussen de eigentrillingen met dwarsdoorsnedes als weergegeven in Figuur 1. Ook is de Gouy-fase van belang in de stralenoptica: ze bepaalt het gedrag van lichtstralen in een trilholte.

Als in de paraxiale benadering de Gouy-fase, als gevolg van de geometrie van de trilholte, gelijk is aan 2π maal een breuk K/N, zullen veel eigentrillingen dezelfde resonantiefrequentie hebben. We noemen zo'n resonator *ontaard*. Op het zelfde moment zal, in het stralenoptische beeld, *elke* lichtstraal een gesloten pad volgen, waarbij ze N keer de trilholte rond gaat voordat ze terugkomt bij het begin. In die N rondgangen gaat zo'n straal K keer omhoog en omlaag. In Figuur 3.7 geven we een aantal voorbeelden van zulke gesloten paden. Als de Gouy-fase niet gelijk is aan 2π maal een breuk K/N, zullen de lichtstralen heen-en-weer blijven kaatsen zonder ooit zichzelf te herhalen.

Buiten de paraxiale benadering zijn zulke gesloten paden nog steeds mogelijk, maar bij resonatorlengtes die iets korter zijn dan binnen de paraxiale benadering. Nu zal niet elke lichtstraal meer een gesloten pad volgen, maar alleen heel specifieke; deze specifieke lichtstralen hangen sterk af van de exacte lengte van de trilholte.

Tenslotte geven we een uitbreiding van de theorie voor paraxiale resonatoren van twee naar drie spiegels, en beschouwen we de mogelijkheid om een ontaarde trilholte te gebruiken om nauwkeurig lengteveranderingen mee te kunnen meten.

Hoofdstuk 4: Pogingen tot een random laser

Zoals al gezegd in de inleiding van deze samenvatting is het daadwerkelijk bouwen van een werkende random laser niet gelukt. Wel zijn we een groot aantal opmerkelijke dingen op het spoor gekomen, zoals de geometrische modes van hoofdstuk 2. In dit hoofdstuk laten we resultaten zien waaruit we afleiden waarom we geen random laser hebben gezien.

Uit metingen aan de frequenties van het licht dat door de laser uitgezonden wordt leiden we af dat de laser vrijwel nooit in een groot aantal modes tegelijk actief is. Wanneer de laser *wel* licht uitzendt in een groot aantal modes, gedragen deze modes zich onafhankelijk, net als we verwachten in een normale laser.

Als we de laser zo lang maken dat de trilholte het licht nog maar net, of juist net niet, op kan sluiten, zien we een aantal opmerkelijke effecten, die waarschijnlijk niet kunnen worden toegeschreven aan een mogelijke random laser. We zien bijvoorbeeld dat de overgang tussen een trilholte die het licht nog net wel, of net niet meer kan opsluiten, veel minder scherp is dan verwacht uit simpele berekeningen. Ook zien we dat de laser niet langer licht uitzendt met een dwarspatroon als in Figuur 1, maar met een ander dwarspatroon (zie bijvoorbeeld Figuur 4.11 op pagina 56), en zelfs een andere kleur en trillingsrichting. Dit grensgebied is nog niet uitgebreid onderzocht, en hier liggen dan ook mogelijkheden voor toekomstig onderzoek.

Hoofdstuk 5: Observatie en manipulatie van golfchaos in een gevouwen optische trilholte

Aangezien het niet mogelijk bleek om direct een random laser te bouwen, hebben we onze aandacht gericht op een *golfchaotische trilholte*. Met zo'n trilholte is het namelijk in principe eenvoudig om een random laser te bouwen, door een lichtversterkend medium toe te voegen. Er zijn al eerder golfchaotische optische trilholtes gemaakt, maar die zijn alle klein, niet eenvoudig te manipuleren, en staan niet alle metingen toe die men aan zo'n systeem zou willen doen. Ons doel was een systeem dat simpel en snel aan te passen is, dat gemaakt kan worden van standaard optische elementen, en waaraan een groot aantal verschillende metingen kan worden gedaan.

De door ons gerealiseerde trilholte is geschetst in Figuur 5.1 op pagina 63. Het is een gevouwen trilholte bestaande uit drie spiegels, waarbij het essentieel is dat de vouwspiegel gekromd is (in ons geval hol). Doordat de gekromde vouwspiegel onder een hoek gebruikt wordt, veroorzaakt deze veel lensfouten (vergelijk dit met een bril waar onder een grote hoek door gekeken wordt); deze lensfouten zorgen ervoor dat het systeem, ondanks de kleine hoeken met de optische as, effectief niet-paraxiaal is. Deze niet-paraxialiteit geeft aanleiding tot *golfchaos*, en kan direct worden beïnvloed door de vouwhoek te variëren: een grotere vouwhoek leidt tot een sterkere niet-paraxialiteit.

Om de aanwezigheid van golfchaos aan te tonen, meten we de resonantiefrequenties van de gevouwen trilholte door licht door de trilholte heen te schijnen. Door dit voor een groot aantal resonatorgeometrieën te doen, verkrijgen we verschillende spectra. Deze spectra worden, na enige wiskundige bewerkingen, gemiddeld, om een uitspraak te kunnen doen over de aanwezigheid van golfchaos. De op deze manier verkregen kromme zal naar een constante waarde neigen. Voor niet-golfchaotische systemen zal de kromme *nooit* onder die constante waarde komen, terwijl ze voor golfchaotische systemen juist onder die waarde *moet* komen, alvorens naar die constante waarde te gaan.

In Figuur 5.5 plotten we vijf van deze krommen, voor vijf verschillende vouwhoeken van de resonator. De bovenste kromme, voor $2\alpha = 0^\circ$, laat geen chaos zien. Dit komt overeen met het verwachte gedrag: een trilholte met $2\alpha = 0^\circ$ komt immers overeen met een resonator opgebouwd uit twee spiegels. Voor $2\alpha = 90^\circ$, dus als de trilholte een rechte hoek maakt, zien we dat de kromme inderdaad onder de constante waarde valt. Dit systeem is dus *golf-chaotisch*. Voor tussenliggende vouwhoeken zien we een vloeiende overgang tussen chaotisch en niet-chaotisch. We zien dat inderdaad de mate van niet-paraxialiteit van het systeem, als bepaald door, onder andere, de vouwhoek van de trilholte, bepalend is voor de sterkte van de golfchaos.

Hoofdstuk 6: Diagnostiek van golfchaos in een gevouwen optische trilholte

De methode die we in hoofdstuk 5 gebruiken om de aanwezigheid van golfchaos in een gevouwen optische trilholte aan te tonen, is van origine ontwikkeld voor de analyse van complexe moleculaire spectra. In deze spectra is het vaak niet goed mogelijk om de afzonderlijke resonantiefrequenties te bepalen; hierdoor is het ook niet mogelijk om de waarschijnlijkheid te bepalen dat twee resonantiefrequenties dicht bij elkaar liggen. Om die reden is deze, alternatieve, methode ontwikkeld, die zonder direct deze waarschijnlijkheden te bepalen toch uitspraken kan doen over het al dan niet chaotisch zijn van zulke spectra.

Voor de succesvolle toepassing van deze methode op ons systeem is een aantal aannames nodig. In dit hoofdstuk laten we zien dat deze aannames gerechtvaardigd zijn. Ook tonen we hoe de experimenten zo efficiënt mogelijk gedaan kunnen worden, waarbij een maximale hoeveelheid informatie wordt afgeleid uit een minimaal aantal metingen. Tenslotte demonstreren we dat het mogelijk is om een selectie te maken uit de metingen om geïsoleerde artefacten uit de uiteindelijke curve weg te filteren, zonder de waarde van deze analysemethode, het beantwoorden van de vraag of een systeem golfchaotisch is of niet, aan te tasten.

Summary:

Multi-mode optical resonators and wave chaos

This thesis is, as you have of course already noticed from the above title, about resonators in which multiple eigenmodes are excited, and about wave chaos. But what do *optical resonator*, *eigenmode* and *wave chaos* actually mean?

Like every specialist field, physics has its own vocabulary and word usage. Besides words that do not exist outside of physics, which a non-physicist most probably won't know, there are a lot of words that resemble, or are derived from, words that we encounter in everyday life. However, in physics the meaning of those words is more narrowly defined, sometimes it is subtly different, and in some cases, almost the opposite.

Since I want to make my thesis, and thus the work that I have done in the past few years, accessible to as broad a public as possible, I have chosen to write a popular science summary. With this I do not aim for precise and exact physics, but for readability and comprehensibility. Therefore, I will first introduce and explain some terms.

Some terms

Light Light is an electromagnetic wave phenomenon, a vibrating electromagnetic field that propagates. You can compare this with a wave that propagates along a water surface. Just like a water wave, light also has wave peaks and valleys. Electromagnetic waves, or radiation, are categorised according to *wavelength*, the distance between two successive wave peaks. The wavelength for light lies approximately between 1 mm (far infrared) and 10 nm (far ultraviolet). Visible light has a wavelength between 730 nm (red) and 400 nm (violet), where one nanometre is equivalent to one millionth of a millimetre (for comparison, human hair has a thickness of between 40 μm and 130 μm, or between 40 and 130 thousandths of a millimetre). At wavelengths longer than 1 mm, we find first microwaves and then radio waves. Radiation with a wavelength of less than 10 nm is called x-rays or gamma rays. The wavelength is, via the speed of light, directly related to the *frequency* of the radiation, where light with a larger wavelength has a lower frequency.

Ray optics In ray optics we neglect, to make matters easier, the wave nature of light, and describe the propagation of light using infinitely thin *light rays*. In uniform media, these rays propagate along straight lines. They are reflected by mirrored surfaces, while at the interface between two different media, for example air and glass, they *refract*. When reflected or refracted, the rays make a sharp bend. Neglecting the wave nature of light is permissible in many situations, mainly (but certainly not always) when the wavelength of the light is very small compared to all dimensions of a system (from the above-mentioned numbers you can see that, roughly, the wavelength of visible light equals one or two hundredths of the thickness of a human hair).

Wave optics In wave optics, we do explicitly take the wave nature of light into account. Because of this, effects that fall beyond the reach of ray optics, can be described properly. One of those effects is bending or *diffraction*. We can see this diffraction as the tendency of light, or any wave phenomenon, to spread out. An example of this is the beam of light from a laser pointer: the beam is approximately 1 mm in diameter close to the pointer, while at a distance of 10 m it has already grown to almost 1 cm.

Another important effect in wave optics is *interference*, where two waves pass through each other. When the peaks and valleys of the first wave coincide with the peaks and valleys of the second wave, the two waves will amplify each other (constructive interference). If instead, the peaks of the first wave coincide with the valleys of the second wave, and vice versa, then the waves will extinguish each other (destructive interference). This effect is easily seen with water waves: if one throws two stones, some distance apart, into a pond, one sees two circular wave patterns spreading out. In the area where the two wave patterns overlap, one can then see lines where the water, as a result of constructive interference, moves wildly up and down. One can also see lines where the water barely moves, as a result of destructive interference.

Paraxial approximation Within the paraxial approximation, we assume that the angle between the axis of an optical system and the direction of propagation of a light ray or wave is small. In that case, one may substitute the sine or tangent of an angle with the angle itself (in radians), $\sin\alpha \approx \tan\alpha \approx \alpha$. This results in a great simplification of the mathematical description of optical problems. Many questions that are simple to solve within the paraxial approximation, lead to considerable problems *outside* that approximation.

Laser The laser thanks its name to the acronym for *light amplification by stimulated emission of radiation*. While a light bulb emits light in all directions and over a broad colour range, light from a laser is concentrated in a narrow beam, and has a very “pure” colour. This colour can vary from (invisible) far infrared, via the near infrared of lasers in CD players, the familiar red of helium-neon lasers, laser pointers and cash registers and the green of laser shows, to the (invisible) ultraviolet and far ultraviolet as is used in chip manufacturing.

Every laser consists of two basic elements: a medium that amplifies the light, and a way to bring back part of the light that comes out of the amplifying medium (feedback). The light that is fed back stimulates the medium to emit identical light. In conventional lasers, this feedback is taken care of by mirrors that let part of the light through and reflect a part. These mirrors enclose the light in a so-called *resonator*.

Resonator A resonator or cavity consists of mirrors that are placed in such a way that they can confine light in a closed path. The simplest example is two mirrors that are directly opposite each other: the light that is reflected by the first mirror falls on the second mirror, which reflects it back to the first, and so forth. Thus, a cavity need not be completely closed in order to confine light, but it is, of course, allowed. The resonators used in this research are all very open and consist of no more than two or three mirrors, varying in size from less than a eurocent to a two euro coin.

In a resonator, it is important that the wave peaks and valleys after the first round trip coincide with the peaks and valleys of the original wave, so that constructive interference occurs. If this happens after *one* round trip, then it will naturally happen after two, three, ten or a hundred round trips. In that case, we speak of *resonance*. If, after one round trip, the wave peaks do not coincide with the peaks of the original wave but with the *valleys*, these peaks and valleys will extinguish each other as a result of destructive interference. Through this process, only light of very well-defined wavelengths can be confined in a cavity. We call these wavelengths *resonant wavelengths*, and the accompanying frequencies *resonance frequencies*. If we change the length of the cavity, for example, by placing the mirrors further apart, then these “matching” wave lengths and frequencies will change with it.

Eigenmode An eigenmode of a resonator or cavity is an electromagnetic wave pattern that exactly repeats itself after one round trip through the resonator. This presumes not only a “matching” wave length, as described above, but also a “matching” pattern perpendicular to the light’s direction of propagation. In a cavity made of concave (hollow) mirrors that bundle the light, there are a number of transverse patterns possible where the natural tendency to spread out (diffraction) is precisely compensated by the net focusing effect of the mirrors. Examples of such transverse profiles of eigenmodes are shown in Figure 1. The simplest transverse pattern, on the top left, is a circle that tapers off smoothly at the edge. Other patterns have horizontal or vertical lines without light, the white lines in the figure. The dimensions of these figures are generally much larger than the wavelength of the light.

These eigenmodes are often simply called *modes*. As shown in Figure 1, there are multiple modes possible in a cavity, each with its own transverse pattern. If light is actually present in one of the profiles in a cavity, we call that mode *excited*. In many lasers, only one mode is excited; the beam that comes out of such a laser then has the same transverse profile as this mode. We call such systems *single mode*. Because the modes are, in principle, independent, multiple modes can be excited at the same time: we call such a system *multi-mode*.

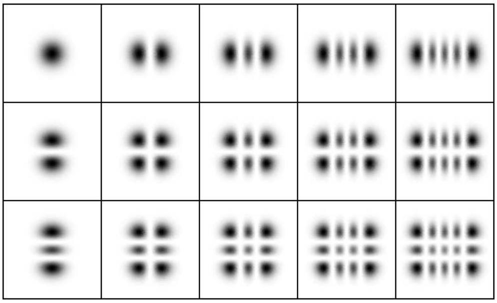

Figure 1: *Some transverse patterns of eigenmodes in a resonator.*

Gouy phase Already in 1890, Gouy found that light that is bundled together, or focused, demonstrates a shift in the position of the wave peaks and valleys that is dependent on how strongly the light is focused. This shift can be expressed in a *phase difference*. The phase of a wave is nothing other than a way to indicate in which part of the wave we are. Compare this to the phases of the moon: new moon, first quarter (waxing), full moon, and last quarter (waning). If the phase of a wave changes, the position of the wave peaks and valleys shifts (relative to, for example, a reference wave).

The phase difference as a result of the focusing of light is called the Gouy phase. This Gouy phase develops gradually in the area around the narrowest part of the beam, the focus. Therefore, the total Gouy phase that light experiences after one round trip through a cavity depends on the way in which the light is focused in the cavity, and thus, on the distance between and the curvature of the mirrors that form the cavity. Furthermore, the transverse pattern of an eigenmode is also of importance: the more complicated the transverse pattern, the larger the Gouy phase after one round trip. Since the Gouy phase causes a shift in the wave peaks and valleys, and since these peaks and valleys must, for resonance, coincide with the peaks and valleys of the previous round trip, the Gouy phase determines very directly the resonance frequencies of each mode. Because the Gouy phase is determined by the distance between and the curvature of the cavity's mirrors, we can easily influence it.

Chaos In contrast with common language use, in physics, chaos does not imply complete randomness. On the contrary, the term (classical) chaos is reserved for systems that develop according to well defined rules (or deterministically), without any randomness, but for which it is nevertheless impossible to predict “the future”. This is because even infinitely small changes in the initial state grow very fast and lead to radically different behaviour. A much used example of a classically chaotic system is the weather on Earth. In 1972, Edward Lorenz illustrated the extreme sensitivity of chaotic systems with his well-known butterfly: a flap of this butterfly's wings in the Brazilian rainforests can cause a tornado in Texas. The *Quantum Weather Butterfly* which graces the cover of my thesis is a further evolution of Lorenz's butterfly.

A very simple example of a classically chaotic system is a billiard table that isn't rectangular, but has rounded ends, a so-called *stadium billiard*, as sketched in Figure 2. In

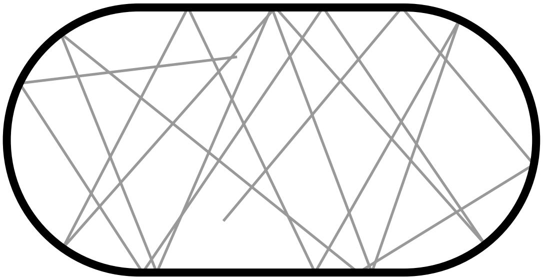

Figure 2: *Stadium billiard with therein the trajectory of a billiard ball.*

such a billiard, the trajectory of a billiard ball is extremely sensitive to the exact position of the ball, or the direction it is shot in; a small change in the place or direction leads to a completely different trajectory.

Wave chaos If, in a classically chaotic system, we substitute *waves* for the (light) rays or particles (the billiard balls), we get a *wave chaotic* system. Because we are now working with waves, the above description of the very fast growth of infinitely small changes no longer applies. The consequences of wave chaos are mostly noticeable in the statistical distribution of the system's resonance frequencies. For a wave chaotic system, the probability that two resonance frequencies lie very close together, is negligibly small. For a non-wave-chaotic system, this probability is relatively large.

Thesis summary

As already mentioned in the introduction to this chapter, this thesis is about optical resonators in which multiple eigenmodes are excited, and about wave chaos. The motivation for this research comes from the direction of the *random laser*: a laser that isn't based on a simple resonator, with easily calculated eigenmodes, but on a *chaotic system*. This system can be a suspension of very small particles, in which light is scattered (compare this with the way light scatters off dust in the air), or a resonator that is wave chaotic because of its shape, like the stadium billiard in Figure 2.

Random lasers have properties that differ significantly from those of conventional lasers. Fundamental physics is mainly interested in the changed noise properties and dynamics of such lasers, and the combination of multiple scattering of light and quantum mechanics. For applied physics, the importance of random lasers lies in the relative insensitivity of these lasers to imperfections, and the resulting potentially lower price. Research into random lasers has already led to, for example, "laser paint" which, according to its inventors, can be used for such diverse applications as anti-counterfeit systems, extremely visible markers, emergency lighting and display technology.

All of the lasers actually realised up until now are based on light scattering particles, in the form of a fine powder or suspension. This makes influencing the distribution of the particles more difficult and often makes exact repeats of experiments impossible. It also leads to lasers that cannot constantly be "on", but only work for short periods at a time. Because a large part of random laser theory has been developed for continuously working systems, a precise comparison of theoretical and experimental results is not very feasible yet.

For these reasons we wanted to build a working random laser based on a *cavity*, instead of light scattering particles. This has as big advantages that the shape of such a cavity is easier to control than the distribution of a powder, and that such a random laser can work continuously.

Unfortunately, in our experiments, we did not succeed in actually building a random laser. At first, we worked on a small, self-built laser, of which we could adjust the geometry with precision. Because this laser's energy is provided by another laser (the pump laser), we can also easily influence the position and size of the area where the light is amplified by letting the pump laser's beam fall on a different spot. This research is described in chapters 2, 3 and 4. In a later stage, our research concentrated on "empty" cavities, without a light amplifying medium. In these systems, which are mainly described in chapters 5 and 6, we have demonstrated the presence of wave chaos.

Chapter 2: Geometric modes in a single-frequency Nd:YVO$_4$ laser

In this chapter, we describe the behaviour of a self-built laser, in which a Nd:YVO$_4$-crystal (pronounced: neodymium yttrium vanadate) takes care of the amplification of light. The system is built in such a way that only light *next to* the optical axis of the system is amplified, as shown in Figure 2.1 on page 5. In general, this means that the laser emits light with a transverse profile as in Figure 2.2, where the leftmost dark spot coincides with the area where light is amplified. You can compare this figure with the topmost row in Figure 1 on page 108.

If we change the distance between the concave and the flat mirror, we see, for a well-defined distance, that the laser emits light in a completely different pattern, namely as shown in Figure 2.3a–d. Subfigure a shows the transverse profile of the eigenmode on the flat mirror, subfigure b shows the transverse profile on the concave mirror. The shape of this eigenmode is shown in subfigure d. We see that this W-shaped mode overlaps much better with the light amplifying area, indicated by the arrow in Figure 2.3d. We've called this mode a *geometric mode*.

This W-shaped mode is the result of cooperation between a large number of eigenmodes, each with transverse profiles comparable with Figure 2.2 or the topmost row in Figure 1. This cooperation is possible because, at this special cavity length, all these eigenmodes have the same frequency. From a ray optics point of view, it is precisely at this length that the W-shaped trajectory forms a closed path. After bouncing back and forth between the mirrors four times, we are back at the starting point.

Also at different distances between the concave and flat mirror, many eigenmodes have the same wavelength. Then, too, the laser will emit light in a geometric mode, but of a different shape.

Chapter 3: Optical resonators and the Gouy phase

In this chapter, we give a more extensive explanation of the observations in chapter 2. We lay out the theory for eigenfrequencies of paraxial resonators, and we speculate on the consequences of non-paraxiality.

Essential to the determination of the eigenfrequencies is the *Gouy phase*. This Gouy phase is determined by the distance between and the shape of the mirrors that form the cavity, or in other words, the geometry of the cavity. For paraxial resonators consisting of two mirrors, this Gouy phase determines the frequency difference between the eigenmodes with transverse profiles as shown in Figure 1. The Gouy phase is also of importance in ray optics: it determines the behaviour of light rays in a cavity.

If the Gouy phase in the paraxial approximation is equal to 2π times a rational fraction K/N (as a result of the geometry of the cavity), many eigenmodes will have the same resonance frequency. We call such a resonator *degenerate*. At the same moment, from a ray-optical perspective, *every* light ray will follow a closed path, where it will go round the cavity N times before it returns to the start. In these N round trips, such a ray goes up and down K times. We give a number of examples of such closed paths in Figure 3.7. If the Gouy phase is not equal to 2π times a rational fraction K/N, the light rays will keep bouncing back and forth without ever repeating themselves.

Such closed paths are still possible outside the paraxial approximation, but at resonator lengths that are a little shorter than within the paraxial approximation. Now not every light ray will follow a closed path, but only very specific ones; these specific light rays are strongly dependent on the exact length of the cavity.

Finally, we expand the theory for paraxial resonators from two to three mirrors, and we examine the possibility of using a degenerate resonator to accurately measure changes in length.

Chapter 4: Attempts towards a cavity random laser

As already mentioned in the introduction to this summary, the actual building of a random laser was unfortunately unsuccessful. We did, however, encounter a great number of striking effects, such as the geometric modes of chapter 2. In this chapter we show results from which we deduce why we have not seen a random laser.

From measurements on the frequencies of the light emitted by the laser, we deduce that the laser is almost never active in a great number of modes at the same time. When the laser *does* emit light in a large number of modes, these modes behave independently, just like we expect from a normal laser.

If we make the laser so long that the cavity can barely, or barely not, confine the light, we see a number of striking effects that, in all probability, cannot be attributed to a possible random laser. We see, for example, that the transition between a cavity that can barely, or barely not, confine the light, is much less sharp than expected from simple calculations. We also see that the laser no longer emits light with a transverse pattern as shown in Figure 1, but with a different transverse pattern (see, for example, Figure 4.11 on page 56), and even a different colour and oscillation direction. This transition area has not been researched in detail. Here, then, lie possibilities for future research.

Chapter 5: Observation and manipulation of wave chaos in a folded optical resonator

Since it was not possible to build a random laser directly, we turned our attention to a *wave chaotic resonator*. With such a resonator it is, in principle, simple to build a random laser, by adding a light amplifying medium. Wave chaotic resonators have been made before, but they are all small, not easy to manipulate, and don't allow all the measurements that one would want to do on such a system. Our goal was a system that is simple and easy to adjust, that can be made from standard optical elements, and on which a large number of different measurements can be done.

The resonator that we realised is sketched in Figure 5.1 on page 63. It is a folded resonator consisting of three mirrors, where it is essential that the folding mirror be curved (in our case, concave). Because this curved folding mirror is used under an angle, it introduces many lens aberrations (compare this to glasses you look through under a large angle). These lens aberrations mean that the system, despite the small angles to the optical axis, is effectively nonparaxial. This nonparaxiality leads to *wave chaos*, and can be directly influenced by varying the folding angle. A larger folding angle leads to increased nonparaxiality.

To demonstrate the presence of wave chaos, we measure the resonance frequencies of the folded resonator by shining light through the resonator. We get a large number of spectra by doing this for different resonator geometries. After some calculations, these spectra are averaged in order to be able to make a statement about the presence of wave chaos. The curve obtained in this manner will tend to a constant value. For non-wave-chaotic systems, the curve will *never* fall below that constant value, while for wave chaotic systems, it *must* fall below that value before tending towards that constant value.

In Figure 5.5, we plot five of these curves, for five different folding angles of the resonator. The top curve, for $2\alpha = 0^\circ$, shows no chaos. This confirms the expected behaviour. After all, a resonator with $2\alpha = 0^\circ$ is equivalent to a resonator built up out of two mirrors. For $2\alpha = 90^\circ$, so if the resonator makes a right angle, we see that the curve does fall below the constant value. This system is thus *wave chaotic*. For folding angles that lie in between, we see a smooth transition between chaotic and not chaotic. We see that the degree of nonparaxiality of the system, as determined by, among others, the resonator's folding angle, does indeed determine the amount of wave chaos.

Chapter 6: Diagnostics of wave chaos in a folded optical resonator

The method that we used in chapter 5 to demonstrate the presence of wave chaos in a folded resonator, was originally developed for the analysis of complex molecular spectra. In these spectra, it is often not possible to determine the individual resonance frequencies. Because of this, it is also not possible to determine the probability of two frequencies lying close together. For that reason, this alternative method was developed, from which statements can be made about such spectra being chaotic or not, without directly having to determine these probabilities.

For the successful application of this method on our system, a number of assumptions are necessary. In this chapter, we show that these assumptions are justified. We also show how the experiments can be done as efficiently as possible, whereby the maximum amount of information can be gained from a minimal number of measurements. Finally, we demonstrate that it is possible to make selections from the measurements to filter out isolated artefacts from the final curve. This can be done without undermining the value of this method of analysis, to answer the question whether a system is wave chaotic or not.

Curriculum Vitae van de auteur

Jos Dingjan werd op 8 september 1974 geboren te Amsterdam. In 1992 behaalde hij het atheneumdiploma aan de Minkema SG (thans Minkema College) te Woerden. In september van dat jaar begon hij de studie Technische Natuurkunde aan de Technische Universiteit Delft. Zijn afstudeerproject vond plaats in de vakgroep Halfgeleiderfysica, onder begeleiding van dr. J. E. Dijkstra en prof. dr. W. Th. Wenckebach. Het onderwerp was de productie van ohmse metallische contacten op silicium met hoge soortelijke weerstand voor gebruik bij lage temperaturen. Hij behaalde zijn ingenieurstitel in 1998.

In november van dat jaar trad hij als Onderzoeker in Opleiding (OiO) in dienst van de Stichting voor Fundamenteel Onderzoek der Materie (FOM), om onderzoek te verrichten in de werkgroep Quantumoptica aan de Universiteit Leiden. Het daar verrichte onderzoek, onder begeleiding van dr. M. P. van Exter en prof. dr. J. P. Woerdman, heeft geresulteerd in dit proefschrift.

In het kader van het promotieonderzoek heeft hij deelgenomen aan de zomerscholen *“Waves and Imaging through Complex Media”* in Cargèse, Frankrijk (1999), *“Mesoscopic physics between photonic and electronic systems”* in Lutherstadt Wittenberg, Duitsland (2000) en *“Let’s Face Chaos through Nonlinear Dynamics”* in Maribor, Slovenië (2002). In 2001 nam hij deel aan de conferenties *“International Conference on Quantum Information (ICQI)”* en *“8th Rochester Conference on Coherence and Quantum Optics (CQO8)”* in Rochester, NY in de Verenigde Staten. Op deze laatste conferentie heeft hij, net als op de zomerschool in Maribor en op de najaarsvergadering van de Nederlandse Natuurkundige Vereniging (Sectie Atoom-, Molecuul- en Optische Fysica) te Lunteren (2001), een wetenschappelijke voordracht gegeven.

Naast deze werkzaamheden gaf hij, als deel van zijn onderwijstaak aan de Universiteit Leiden, aan eerstejaarsstudenten werkcollege in het vak “Elementaire Kinetische Theorie”, en fungeerde hij van 2000–2002 als helpdesk voor eerstejaarsstudenten voor het vak “Programmeermethoden”. Tevens was hij lid van de Bedrijfshulpverlening (BHV) van het Huygenslaboratorium, en organiseerde hij de jaarlijkse kerstontbijten voor de vakgroep.

Curriculum Vitae of the author

Jos Dingjan was born in Amsterdam, on 8 September 1974. In 1992 he got his “atheneum” diploma at the Minkema SG (now Minkema College) in Woerden. In September of the same year he started his study of Applied Physics at the Technische Universiteit Delft. His graduation project took place in the Semiconductor Physics Group, under supervision of Dr. J. E. Dijkstra and Prof. Dr. W. Th. Wenckebach. The subject was the production of ohmic metallic contacts on high-resistivity silicon for use at low temperatures. He got his Master’s degree in 1998.

In November of that year he was employed by the “Stichting voor Fundamenteel Onderzoek der Materie” (FOM) as a Ph.D. student, to work in the Quantum Optics group at the Universiteit Leiden. The research he performed there, under supervision of Dr. M. P. van Exter and Prof. Dr. J. P. Woerdman, has resulted in this thesis.

As part of his Ph.D. research he participated in the summer schools *“Waves and Imaging through Complex Media”* in Cargèse, France (1999), *“Mesoscopic physics between photonic and electronic systems”* in Lutherstadt Wittenberg, Germany (2000), and *“Let’s Face Chaos through Nonlinear Dynamics”* in Maribor, Slovenia (2002). In 2001 he participated in the conferences *“International Conference on Quantum Information (ICQI)”* and *“8th Rochester Conference on Coherence and Quantum Optics (CQO8)”* in Rochester, NY, USA. He gave a scientific presentation at this last conference, as well as at the summer school in Maribor and at the autumn meeting of the Atomic, Molecular and Optical Physics section of the “Nederlandse Natuurkundige Vereniging” (NNV) in Lunteren (2001).

Besides this work, as part of his teaching obligations, he gave tutorials in the course “Elementary Kinetic Theory” to first year students, and served as help desk for first year students for the course “Programming methods”. In addition he was a fire warden at the Huygens Laboratory, and he organised the annual group Christmas breakfasts.

Nawoord

Om maar eens een bekend Nederlands gezegde te parafraseren: “Een onderzoek doe je zelden alleen”, en een promotieonderzoek al helemaal niet. Dit proefschrift is tot stand gekomen onder de begeleiding, en met waardevolle inbreng, van mijn promotor, Han Woerdman, en mijn copromotor, Martin van Exter.

Natuurlijk zijn zij niet de enigen die een belangrijke rol gespeeld hebben. Zonder Jan Post, Koos Benning en Ewie de Kuyper van de fijnmechanische dienst zou een groot deel van mijn opstelling niet bestaan hebben, terwijl Richard van Leeuwen, René Overgauw, Arno van Amersfoort en Leendert Prevo van de elektronische dienst zorg droegen voor de elektronische aansturing, de servers en het computernetwerk, tegenwoordig bijna onmisbaar in een natuurkundig experiment. Ook aan de onontbeerlijke spin in het web van alle regels en formulieren die tegenwoordig aan een promotieonderzoek kleven, groepssecretaresse Anneke Aschoff, ben ik zeer veel dank verschuldigd.

Door de jaren heen heb ik, voor kortere of langere tijd, of zelfs meerdere keren, een aantal studenten mogen begeleiden: Erwin Altewischer, William Irvine, Randy Kalkman en Riccardo Sapienza hebben elk hun eigen aandeel gehad in mijn onderzoek. Ook mijn medepromovendi en de postdocs mag ik niet vergeten: Frans, Gerwin, Krista, Alexander, Marnix, Steven, Yngve, Sumant, Hayk, Jorrit, Javier, Erwin, Thijs, Peter, Nikolay, Graciana, Carles, Silvania, Klaasjan, Sergio, Andrea, Cyriaque en Dirk, bedankt voor de discussies, zowel op wetenschappelijk als niet-wetenschappelijk gebied, en voor de gezelligheid.

Ik heb de mensen van `#drum` schaamteloos gebruikt als klankbord voor verschillende vragen aangaande de Engelse taal, waarvoor ik ze bedank. Mijn ouders, familie en vrienden hebben mij al deze jaren welwillend aangehoord, en ik beloof ze dat ik niet zal ophouden ze te bedelven onder half-begrijpelijk natuurkundegepraat. En natuurlijk Kimberley, who has helped me perfect the art of Dunglish, om middenin een zin om te schakelen naar een andere language, and seamlessly back again, tot grote verwarring van omstanders.

Afterword

To paraphrase a well-known English saying: “A thesis wasn’t built in a day”, and, like Rome, it wasn’t done all alone, either. It was completed under the supervision, and with valuable contribution, of my thesis supervisor, Han Woerdman, and co-supervisor, Martin van Exter.

Of course, they are not the only ones who played an important role. Without Jan Post, Koos Benning and Ewie de Kuyper of the mechanical workshop a large part of my setup would not have existed. Richard van Leeuwen, René Overgauw, Arno van Amersfoort and Leendert Prevo of the electronics services department took care of the control electronics, the servers and the computer network, which nowadays are almost indispensable in a physics experiment. I also owe a large debt of gratitude to the vital spider in the web of all regulations and forms that nowadays surround a Ph.D. research project, group secretary Anneke Aschoff.

Through the years I have, for shorter or longer periods of time, or even multiple times, supervised a number of students: Erwin Altewischer, William Irvine, Randy Kalkman and Riccardo Sapienza all had their own part in my research. I should also not forget my fellow Ph.D. students and postdocs: Frans, Gerwin, Krista, Alexander, Marnix, Steven, Yngve, Sumant, Hayk, Jorrit, Javier, Erwin, Thijs, Peter, Nikolay, Graciana, Carles, Silvania, Klaasjan, Sergio, Andrea, Cyriaque and Dirk, thanks for the discussions, both scientific and non-scientific, and for the “gezelligheid”.

I have shamelessly used the people of `#drum` as a sounding board for various questions regarding the English language, for which I thank them. My parents, family and friends have lent me a willing ear all these years, and I promise I will not stop bothering them with half-comprehensible physics-gobbledygook. And of course Kimberley, die me geholpen heeft de kunst van Engerlands te perfectioneren, to switch, in the middle of a sentence, to a different taal, en naadloos weer terug, much to the confusion of surrounding people.